

Superstrong Dynamics and Chiral Emission of a Giant Atom in a Structured Bath

V. Jouanny,^{1,2} L. Peyruchat,^{1,2} M. Scigliuzzo,^{3,2} A. Mercurio,^{4,2} E. Di Benedetto,⁵ D. De Bernardis,⁶ D. Sbroggiò,^{1,2} S. Frasca,^{1,2} V. Savona,^{4,2} F. Ciccarello,^{5,7} and P. Scarlino^{1,2}

¹*Hybrid Quantum Circuits Laboratory (HQC), Institute of Physics,
École Polytechnique Fédérale de Lausanne (EPFL), 1015, Lausanne, Switzerland*

²*Center for Quantum Science and Engineering,
Institute of Physics, École Polytechnique Fédérale de Lausanne (EPFL), 1015, Lausanne, Switzerland*

³*Laboratory of Photonics and Quantum Measurements (LPQM), Institute of Physics,
École Polytechnique Fédérale de Lausanne (EPFL), 1015, Lausanne, Switzerland*

⁴*Laboratory of Theoretical Physics of Nanosystems, Institute of Physics,
École Polytechnique Fédérale de Lausanne (EPFL), 1015, Lausanne, Switzerland*

⁵*Università degli Studi di Palermo, Dipartimento di Fisica e Chimica-Emilio Segrè, Via Archirafi 36, 90123 Palermo, Italy*

⁶*National Institute of Optics (CNR-INO), c/o LENS via Nello Carrara 1, Sesto F.no 500019, Italy*

⁷*NEST, Istituto Nanoscienze-CNR, Piazza S. Silvestro 12, 56127 Pisa, Italy*

(Dated: September 3, 2025)

Quantum emitters coupled to waveguides with nonlinear dispersion show rich quantum dynamics with the promise of implementing non-trivial non-Markovian quantum models. Recent advances in engineered photonic environments now allow the realization of discrete-site waveguides with tailored dispersion, yet most implementations of waveguide QED remain limited to a local qubit-waveguide coupling. Here, we study a transmon qubit non-locally coupled to a high-impedance coupled cavity array (CCA), thus implementing a *giant atom* in a structured photonic environment. The non-local coupling produces interference with the CCA eigenmodes, selectively enhancing interaction with long-wavelength (low-effective k), symmetric modes about the array center, while suppressing coupling to antisymmetric and short-wavelength modes. For a subset of symmetric, low-effective k modes, we reach the superstrong coupling regime. In this regime, measurements of the atomic participation ratio reveal strongly hybridized eigenmodes on a par with a strongly reduced qubit participation at the frequency of maximum hybridization with the qubit, in agreement with theory. Time-domain measurements of the qubit dynamics show clear deviations from the single-mode Jaynes–Cummings model, marked by the emergence of mode–mode interactions. By breaking inversion symmetry, the qubit seeds dressed eigenmodes confined to either the right or left of the qubit, which we exploit to implement and characterize a chiral photon-emission protocol. These results demonstrate precise control over multimode light–matter interaction in a structured photonic environment.

I. INTRODUCTION

Controlling the interaction between emitters and confined photonic modes lies at the heart of cavity quantum electrodynamics (QED), achieving milestones ranging from the demonstration of strong coupling to the development of quantum information processing [1–3]. At the other extreme, continuous waveguide QED describes qubits coupled to a 1D continuum of propagating modes, where interference can give rise to collective radiative phenomena and chiral interactions [4–10]. Between these limits lies *multimode QED*, where a qubit couples to a discrete set of modes [11]. When the qubit–mode coupling strength exceeds the characteristic mode frequency spacing, the system enters the *superstrong coupling regime* [12, 13]: the qubit hybridizes with multiple modes simultaneously, leading not only to a reshaping of their spectrum but also to significant mode–mode hybridization. This hybridization drives dynamics beyond the single-mode Jaynes–Cummings paradigm, manifesting in the breakdown of single-mode Rabi oscillations and in strong spatial confinement effects of the eigenmodes [12–14]. Experiments in the linear-dispersion regime [11, 15–19] have revealed rich non-Markovian effects [20]. However,

in such systems the qubit typically remains hybridized across the entire accessible spectrum, hindering single-photon state preparation and limiting time-resolved access to quantum dynamics.

Structured photonic environments with engineered bandgaps overcome these limitations, enabling quantum state preparation inside the gap and subsequent transfer into the band [21]. Such environments can be realized with stepped-impedance waveguides [22, 23], periodically loaded waveguides [24] or coupled cavity arrays (CCAs) [21, 25–32]. At their band edges, such environments support atom–photon bound states [33, 34], providing new routes for analog quantum simulation [35], offering alternative paths for quantum computing architectures [36–38], and enabling directional interactions [26, 39, 40]. In all of these experiments, artificial atoms have been coupled to a *single site* of the array, fulfilling the electric dipole approximation. In this limit, due to parity symmetry, the n th CCA mode couples equally to the qubit as the $(N - n)$ th mode, where N is the total number of modes. As a result, strong coupling to band-edge modes opens large avoided crossings, which hinder non-adiabatic transfer between bandgap and in-band states, effectively “trapping” the qubit outside the

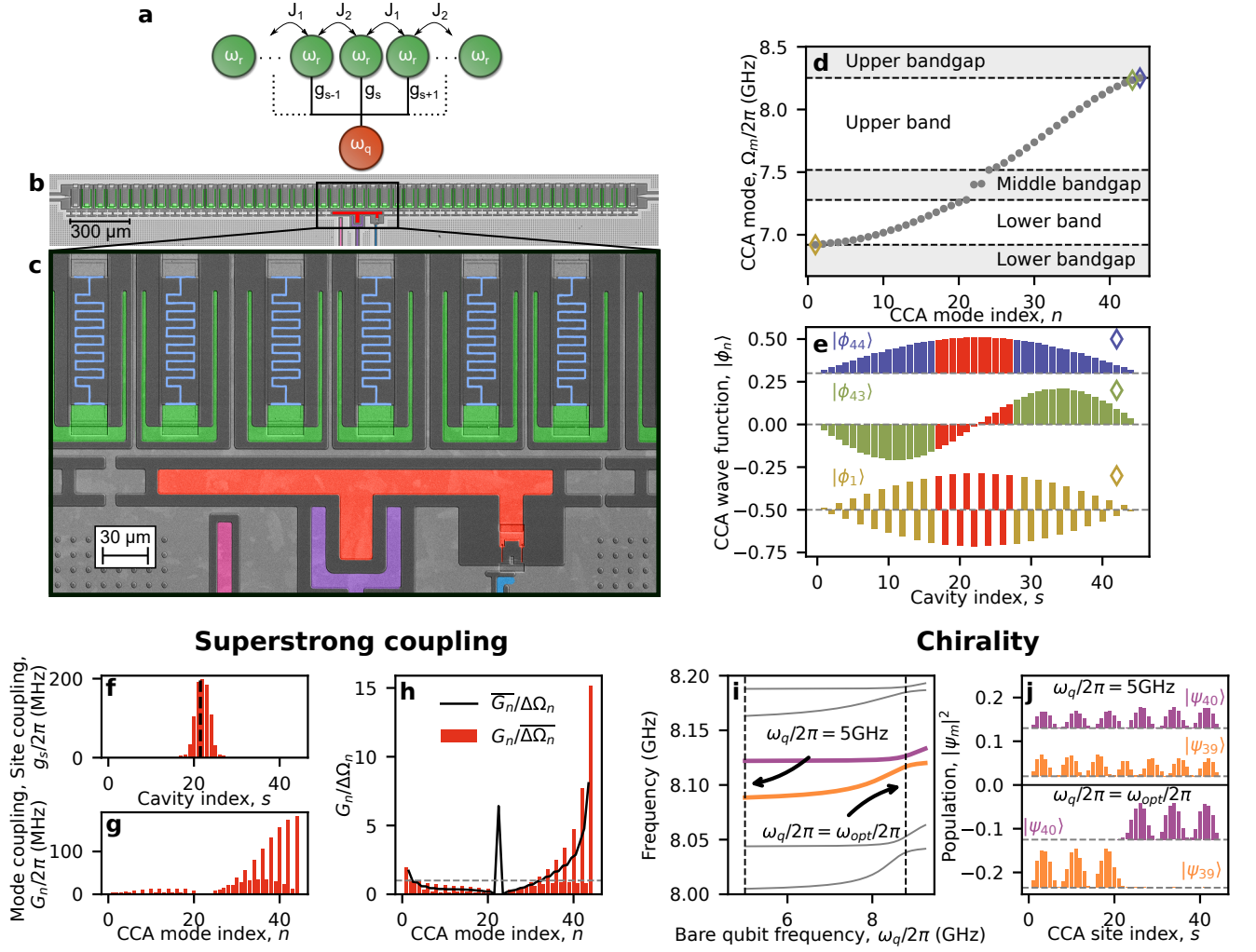


Figure 1. **Giant atom interacting with a structured photonic bath.** (a) Pictorial representation of the system. Cavities of bare frequency $\omega_r/2\pi$ (green) are coupled in a dimerized fashion with staggered couplings $J_1/2\pi$ and $J_2/2\pi$. The qubit, with transition frequency $\omega_q/2\pi$, is shown in red and coupled to cavity s with strength $g_s/2\pi$. (b) False-colored optical micrograph of a representative device. Aluminium appears light grey, silicon dark grey, cavities green, and the qubit red. Drive, readout, and flux lines are pink, violet, and blue, respectively. (c) False-colored scanning electron micrograph. NbN inductors of the metamaterial resonators are highlighted in light blue. (d) Spectrum of the CCA modes, $\Omega_n/2\pi$, versus mode index n (grey dots). Bandgaps are shaded grey. (e) Spatial profiles of modes $|\phi_{44}\rangle$ (blue), $|\phi_{43}\rangle$ (green), and $|\phi_1\rangle$ (gold) versus site index s . Qubit-CCA coupling sites are shown in red. (f) Spatial profile of the qubit-cavity coupling $g_s/2\pi$. The vertical black dashed line indicates the center of the CCA. (g) Qubit-mode coupling $G_n/2\pi$ versus mode index n . (h) Superstrong coupling quantifier $G_n/\Delta\Omega_n$ versus mode index n , with $\Delta\Omega_n = \Omega_n - \Omega_{n-1}$. The black line uses the average coupling to the two modes of each splitting, $\bar{G}_n/\Delta\Omega_n$, while the red bars use the average mode spacing, $G_n/\Delta\Omega_n$. The horizontal grey dashed line represent $G_n/\Delta\Omega_n = 1$. (i) Dressed CCA modes $\tilde{\omega}_n/2\pi$ versus bare qubit frequency $\omega_q/2\pi$. Orange and purple lines indicate the modes studied in panel j. (j) Spatial profile of the population $|\psi_m|^2$ of modes $|\psi_{39}\rangle$ and $|\psi_{40}\rangle$ versus site index s . Data are shown for $\omega_q/2\pi = 5$ GHz, where the modes are weakly affected by the qubit, and for $\omega_q/2\pi = \omega_{\text{opt}}/2\pi$, where $|\psi_{40}\rangle$ is maximally chiral.

band and preventing access to the rich dynamics of the superstrong regime.

This problem can be overcome by engineering a suitable qubit-mode coupling profile [41]. Notably, this can be achieved by coupling the qubit non-locally to multiple lattice sites, realizing a *giant atom* [42–44]. Destructive interference suppresses coupling to low-frequency band-edge modes, facilitating non-adiabatic transfer from the lower bandgap into the band, while constructive in-

terference selectively enhances interactions with a subset of high-frequency band-edge modes [see Methods], thereby enabling access to superstrong coupling dynamics. Although such non-local coupling has been studied in waveguide-QED systems [43, 45–47], it has not yet been realized in structured photonic environments [48–52].

In this work, we realize a transmon qubit non-locally coupled to a high kinetic inductance gapped CCA [Fig. 1b–c] [28]. Specifically, the qubit couples to seven

Parameter Group	Parameter	Description
Indices	s	Cavity index
	n	CCA mode index
	m	Dressed mode index
CCA sites basis	$\omega_r/2\pi$	Resonant frequency
	$g_s/2\pi$	Qubit-cavity coupling rate
CCA modes $ \phi_n\rangle$	$\Omega_n/2\pi$	CCA mode frequency
	$G_n/2\pi$	Qubit-mode coupling rate
Dressed CCA modes $ \psi_m\rangle$	$\tilde{\omega}_m/2\pi$	Dressed CCA mode frequency
Effective CCA modes	$\Omega_n^{\text{eff}}/2\pi$	Effective CCA mode frequency
	$G_{n,n'}/2\pi$	Mode-mode coupling rate
Effective dressed CCA modes	$\tilde{\omega}_m^{\text{eff}}/2\pi$	Effective dressed CCA mode frequency

Table I. Notation for the paper.

lattice sites, thereby implementing a *giant atom* interaction [Fig. 1a]. Constructive interference enhances coupling to high-frequency modes, granting access to the superstrong regime [Fig. 1g–h], where we investigate both steady-state and dynamical properties [section III, section IV]. Moreover, the chosen coupling configuration breaks spatial inversion symmetry [Fig. 1f], such that the dressed CCA modes acquire *chirality*: their photonic components are deterministically confined to one side of the array relative to the qubit position [Fig. 1i–j]. We exploit this chirality to demonstrate directional emission of a single-photon quantum state [section V, section VI].

II. EXPERIMENT

The device comprises a Coupled Cavity Array (CCA) with $N = 44$ cavities, implemented as a superconducting metamaterial composed of compact ($50 \times 125 \mu\text{m}^2$) high-kinetic inductance lumped LC resonators with a resonant frequency of $\omega_r/2\pi = 7.749 \text{ GHz}$ [Fig. 1a–c]. The CCA implements the Su-Schrieffer-Heeger (SSH) model in its symmetry-protected topological phase [53, 54], with dimerized hopping rates of $J_1/2\pi = 258 \text{ MHz}$ and $J_2/2\pi = 370 \text{ MHz}$ [Fig. 1a–d]. Nonetheless, the topology of the SSH will not be involved in what follows. A flux-tunable transmon qubit [55] is coupled to multiple cavities of the CCA [Fig. 1]. The total setup is described by the Hamiltonian ($\hbar = 1$ in the remainder of

the manuscript)

$$\begin{aligned}
 H &= H_{\text{CCA}} + H_{\text{QB}} + H_{\text{INT}} \\
 &= \omega_r \sum_{s=1}^N a_s^\dagger a_s + J_1 \sum_{s=1}^{N/2} \left(a_{2s-1}^\dagger a_{2s} + \text{H. c.} \right) \\
 &\quad + J_2 \sum_{s=1}^{N/2-1} \left(a_{2s}^\dagger a_{2s+1} + \text{H. c.} \right) \\
 &\quad + \omega_q b^\dagger b - \frac{E_C}{2} b^\dagger b^\dagger b b + \sum_{s=1}^N g_s \left(a_s^\dagger b + \text{H. c.} \right),
 \end{aligned} \tag{1}$$

where H_{CCA} , H_{QB} and H_{INT} , are the CCA, qubit and interaction Hamiltonian. a_s (b) annihilates an excitation on cavity s (the transmon qubit), $\omega_q/2\pi$ is the tunable transition frequency between $|g\rangle$ and $|e\rangle$ (respectively ground and first-excited states of the qubit), while the qubit anharmonicity is given by $E_C/2\pi = 318 \text{ MHz}$. To better model the system, higher order CCA coupling terms are taken into account but not reported in this Hamiltonian [see [Supplementary Note A](#)]. Ultimately, these higher-order couplings are responsible for the observed asymmetry of the energy bands [see Fig. 1d]. Finally, $g_s/2\pi$ is the coupling strength between the transmon qubit and cavity s , which breaks spatial inversion symmetry around the CCA inversion center [Fig. 1f].

Single-photon eigenstates of the bare CCA Hamiltonian H_{CCA} are expressed as $|\phi_n\rangle = \sum_s d_{s,n} |s\rangle$, where $|s\rangle = a_s^\dagger |\text{vac}\rangle$ is the single photon state on cavity s and $d_{s,n}$ is the corresponding probability amplitude. Analogously, single-excitation eigenstates of the full Hamiltonian H will be written as $|\psi_m\rangle = u_m |e, \text{vac}\rangle + \sum_s c_{s,m} |g, s\rangle$. Unlike $|\phi_n\rangle$, these states are dressed with the qubit. The ground state of the system is $|g, \text{vac}\rangle$. For clarity, [Tab. I](#) introduces the notation of the different bases used in this work.

III. SUPERSTRONG COUPLING

We first measure the CCA using single-tone spectroscopy in transmission as a function of the qubit frequency at low power to remain in the single-excitation manifold [Fig. 2a]. Due to the dimerization of the CCA, we observe two bands separated by $\sim |J_2 - J_1|$. The dressed qubit frequency, $\tilde{\omega}_q/2\pi$, is measured using standard two-tone spectroscopy [see [Supplementary Note C](#)] and reported in Fig. 2a as purple circles above the upper band and pink circles in the middle bandgap. This highlights the presence of an atom-photon bound state (APBS) in the upper bandgap [22, 27]. The combined single- and two-tone spectroscopy data are globally fitted to the Hamiltonian eigenvalues (dressed CCA modes) in Eq. (1), $\tilde{\omega}_m$, showing excellent agreement [see inset Fig. 2a]. A fit with resonant frequency disorder allows to extract precisely the eigenmode frequencies [see [Ext Data Fig. 1](#)].

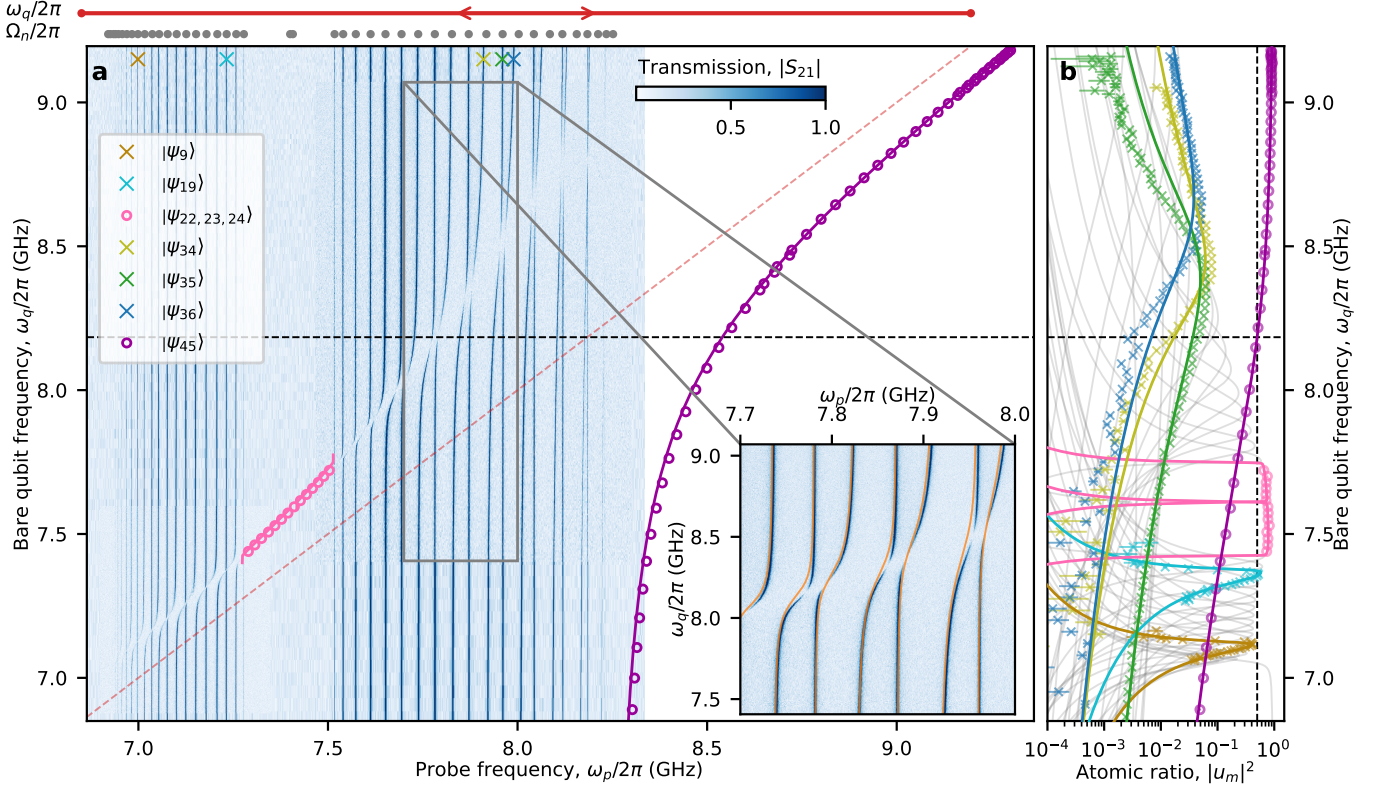


Figure 2. **Steady-state interaction of a giant atom with a structured photonic bath.** (a) Single-tone transmission of the CCA as a function of bare qubit frequency $\omega_q/2\pi$. The dressed qubit frequency extracted from two-tone spectroscopy is shown above the upper band (purple circles) and inside the middle bandgap (pink circles). Model predictions according to Eq. (1) for the dressed qubit are shown as purple and pink lines, and the bare qubit frequency as a red dashed line. Crosses indicate the dressed CCA modes analyzed in panel b. Inset: zoom-in from $\omega_p/2\pi = 7.7$ GHz to 8 GHz; orange lines show eigenvalues, $\tilde{\omega}_m/2\pi$, of the fitted disorder-free model according to Eq. (1). (b) Atomic participation ratio of each eigenmode, $|u_m|^2$. Grey lines: expected atomic participation ratio, $|u_m|^2$, of each mode according to Eq. (1); circles and crosses: values extracted from two-tone and single-tone spectroscopy, respectively (error bars from the standard deviation of fitted dressed-mode frequencies), using $|u_m|^2 = d\tilde{\omega}_m/d\omega_q$. Vertical black dashed line: reference atomic ratio of 0.5. Horizontal black dashed line: qubit frequency where the atomic ratio of the APBS, $|u_{45}|^2$, is 0.5 (also marked in panel a). Mode labels are indicated in the legend in panel a.

We observe that the qubit interacts strongly with the upper passband and weakly with the lower one, as seen from the small and large frequency shifts, respectively [Fig. 2a]. This is a direct consequence of the non-local coupling (giant atom regime) of the transmon qubit to the CCA, which inhomogeneously redistributes the coupling strength over the CCA normal modes. At the upper band edge, the qubit strongly hybridizes with photonic modes, producing a visible frequency shift even when the bare qubit is significantly detuned from the upper band edge [Fig. 2a].

When the qubit-mode coupling strength to the n th CCA mode, G_n , becomes comparable to the mode spacing $\Delta\Omega_n = \Omega_n - \Omega_{n-1}$, the avoided crossing shifts exceed $\Delta\Omega_n$, effectively hybridizing multiple modes simultaneously. To characterize this regime quantitatively, we introduce two complementary metrics. Since there are N coupling strengths but only $N - 1$ mode spacings, we define (i) the *average coupling per splitting*, $\bar{G}_n/\Delta\Omega_n$, where

each mode spacing is normalized by the average of the two adjacent couplings [see black line in Fig. 1h], and (ii) the *average splitting per coupling*, $G_n/\bar{\Delta\Omega}_n$, where each coupling is normalized by the average of the neighboring mode spacings [see red bars in Fig. 1h].

In systems with linear dispersion and uniform coupling, superstrong coupling produces a smooth frequency shift of all modes as a function of the qubit frequency [16]. In our case, however, the staggered coupling of the qubit to the CCA modes [see Fig. 1g] leads to an alternating pattern: modes that are even with respect to the giant experience large frequency shifts, while odd modes, weakly coupled at the qubit position, remain nearly unperturbed [see inset Fig. 1a and Supplementary Note D]. Consequently, strongly shifted modes overlap with weakly shifted ones.

Due to the high $G_n/\Delta\Omega_n$ ratio, the qubit is expected to participate simultaneously in multiple eigenmodes. We quantify this with the *atomic participation ratio* [56, 57],

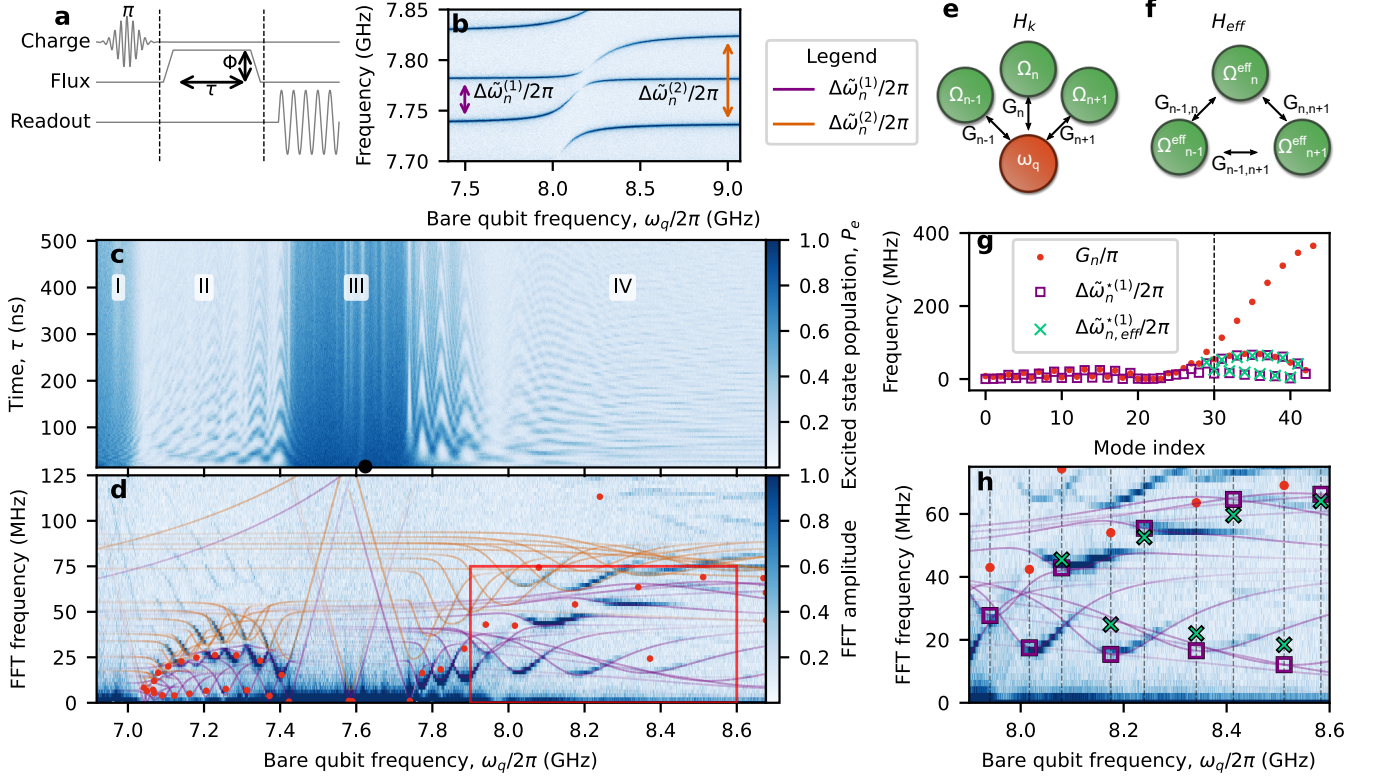


Figure 3. **Superstrong dynamics.** (a) Pulse sequence: the qubit is excited, non-adiabatically displaced in frequency for a time τ , then returned at its initial frequency for readout. (b) Zoom-in on the spectroscopy of Fig. 2a. Energy spacings between consecutive and next-nearest dressed CCA modes are denoted $\Delta\tilde{\omega}_n^{(1)}/2\pi$ (purple arrows) and $\Delta\tilde{\omega}_n^{(2)}/2\pi$ (orange arrows), respectively. (c) Measured qubit excited-state population versus τ and $\omega_q/2\pi$. The black dot marks the bare qubit frequency at $\tau = 0$, corresponding to a dressed frequency $\tilde{\omega}_q/2\pi = 7.43$ GHz. (d) Fast Fourier transform of the data in panel c. Purple (orange) lines indicate $\Delta\tilde{\omega}_n^{(1)}/2\pi$ ($\Delta\tilde{\omega}_n^{(2)}/2\pi$). The intensity of the lines is proportional to $|u_i|^2|u_j|^2$. Red dots mark G_n/π , the expected Rabi rate between the qubit and CCA mode n . (e) Hamiltonian H_k in the CCA mode basis [see Methods], with bare eigenmodes of frequency $\Omega_n/2\pi$, coupling rates $G_n/2\pi$, and the bare qubit at $\omega_q/2\pi$. Just three modes are shown. (f) Corresponding effective Hamiltonian H_{eff} from perturbation theory [see Methods], featuring effective eigenmodes of frequency $\Omega_n^{\text{eff}}/2\pi$ and induced mode–mode couplings $G_{n,n'}/2\pi$, between modes n and n' . (g) Comparison between expected and measured Rabi rates versus mode index. Red dots: G_n/π . Purple squares: $\Delta\tilde{\omega}_n^{*(1)}/2\pi$, the nearest-neighbor spacing $\Delta\tilde{\omega}_n^{(1)}$, where $|u_n|^2|u_{n+1}|^2$ is maximum. Green crosses: $\Delta\tilde{\omega}_{n,\text{eff}}^{*(1)}/2\pi$, the effective nearest-neighbor spacing $\Delta\tilde{\omega}_{n,\text{eff}}^{(1)}/2\pi$, where $|u_n|^2|u_{n+1}|^2$ is maximum H_{eff} . (h) Zoom-in of the red frame in panel d, the markers and lines as previously defined in panel d and g. Vertical dashed lines, bare qubit frequencies at which $|u_n|^2|u_{n+1}|^2$ is maximum.

defined as $|u_m|^2$ for the m th dressed eigenstate $|\psi_m\rangle$. In Fig. 2b, we show the atomic ratios in grey, extracted from each of the eigenstates of Hamiltonian Eq. (1), plotted on a logarithmic scale. Experimentally, we determine $|u_m|^2$ using the Hellmann–Feynman theorem [56, 58], which yields $|u_m|^2 = d\tilde{\omega}_m/d\omega_q$, and report values for several dressed modes in Fig. 2b [additional data in Supplementary Note D]. As required by normalization, $\sum_m |u_m|^2 = 1$. The small discrepancies between theory and experiment are attributable to disorder.

When $G_n/\Delta\Omega_n \lesssim 1$, the qubit participation ratio for a given dressed mode exhibits a narrow resonance, peaking near unity when the qubit is tuned into resonance with a bare CCA mode. This behavior is characteristic of a *single-mode coupling* regime, where the qubit

primarily interacts with one mode at a time. In contrast, when $G_n/\Delta\Omega_n > 1$, the participation ratio broadens and its maximum is lowered, marking the onset of the *superstrong coupling* regime, where the qubit interacts simultaneously with multiple modes. As $G_n/\Delta\Omega_n$ increases, the participation maxima decrease smoothly across the upper band. In this regime, the dressed modes remain mostly photonic, and the strong qubit hybridization induces mode–mode interactions, renormalizing the dynamics of the system [13, 20].

IV. DYNAMICS OF THE EMITTER

In section III, we demonstrated that the qubit interacts simultaneously with several CCA modes by measur-

ing the atomic participation ratio. Here, we investigate how the superstrong coupling regime affects the qubit dynamics using the pulse sequence shown in **Fig. 3a**. The qubit is first initialized in the middle bandgap [black dot in **Fig. 3c**]. A constant flux offset, Φ , with a 2.4 ns ramp is then applied, shifting the bare qubit frequency for a duration τ . Finally, the qubit is returned to its initial frequency and its state measured.

In **Fig. 3c**, we show the qubit excited-state population as a function of the interaction time τ and the bare qubit frequency $\omega_q/2\pi$. This measurement reveals four distinct interaction regions. Within the bandgaps (I, III), minimal interaction with the eigenmodes is observed, as indicated by the absence of Rabi oscillations. Nonetheless, enhanced decay rates are noted, attributed to the presence of Two-Level-System fluctuators [59] on the chip and, in the middle bandgap, to weak coupling with the SSH edge modes of the CCA. By contrast, when the qubit is tuned within the passbands (II, IV), Rabi oscillations appear. As the qubit is tuned further into the bands, these oscillations strongly interfere. Since the qubit is initialized and measured in the middle bandgap (III), the upper bandgap does not contribute to this measurement. The strong coupling to the highest-frequency CCA modes prevents non-adiabatic transfer between band states and bandgap, effectively trapping the qubit within the band [see **Supplementary Note E**].

To gain deeper insight, we present in **Fig. 3d** the Fast Fourier Transform (FFT) of the data shown in **Fig. 3c**. For a qubit coupled to a single mode at frequency $\Omega_n/2\pi$, we expect to observe Rabi oscillations at frequency $\left(\sqrt{4G_n^2 + \Delta_n^2}\right)/2\pi$, where $\Delta_n = \Omega_n - \omega_q$ is the detuning. This picture works in the lower band [see **Fig. 3d**], where we observe a good match between the expected resonant ($\Delta_n = 0$) Rabi frequency and the observed ones. This reinforces our claim that the interaction in the lower band remains in the single-mode regime. Systematic deviations emerge once the qubit is tuned deep into the upper band, corresponding to a region where the system enters the superstrong coupling regime ($G_n/\Delta\Omega_n > 1$). Here, the simultaneous participation of the qubit in several CCA modes allows the observation of transitions between (dressed) modes at different (dressed) frequencies $\tilde{\omega}_n$. This behavior is confirmed by the transition frequencies (energy differences) $\Delta\tilde{\omega}_n^{(i)} = \tilde{\omega}_{n+i} - \tilde{\omega}_n$ for $i = 1$ (purple lines) and $i = 2$ (orange lines) [**Fig. 3b**], which overlay the FFT spectrum in **Fig. 3d** and **Ext Data Fig. 2**.

In **Fig. 3g**, we compare the coupling expected from the single-mode Jaynes-Cummings model (red dots) with the energy difference between neighboring eigenmodes at the qubit frequency of maximum interaction, $\Delta\tilde{\omega}_n^{*(1)}$, i.e. $\Delta\tilde{\omega}_n^{(1)}$ at the qubit frequency at which $|u_n|^2|u_{n+1}|^2$ reaches its maximum (purple squares). As seen in **Fig. 3d–h**, these values no longer match once $\overline{G_n}/\Delta\Omega_n \gtrsim 1$ [dashed line in **Fig. 3g**], marking a clear deviation from the single-mode Jaynes-Cummings model. To gain in-

sight into the underlying physics, we derive an effective theory that reveals a qubit mediated mode-mode interaction [see **Fig. 3f** and **Methods**]. Although this effective model is strictly valid only when the qubit is detuned from the CCA bands, it exhibits excellent agreement with the energy difference $\Delta\tilde{\omega}_n^{*(1)}$ in the upper band [see green crosses vs purple squares in **Fig. 3g–h**]. Together, these results demonstrate that our platform enables single-photon dynamics to be tracked across the crossover from the single-mode to the superstrong coupling regime.

V. CHIRALITY

We focus on the effect of breaking the inversion symmetry of the CCA [**Fig. 1f**], which renders a subset of dressed CCA modes chiral, conditional to the bare qubit frequency [10, 60]. This effect is evident looking at reflection measurements from both the left and right sides of the CCA, resulting in a different signal contrast near maximum qubit-mode hybridization (i.e. maximum atomic ratio) [**Fig. 4a–d**]. More specifically in **Fig. 4a–b** the reflectivity probes the chirality of the modes ($|\psi_{13}\rangle, |\psi_{14}\rangle$) at the weak coupling ratio $\overline{G_n}/\Delta\Omega_n \approx 0.35$, while in **Fig. 4c–d** of modes ($|\psi_{31}\rangle, |\psi_{32}\rangle$), corresponding to the superstrong coupling ratio $\overline{G_n}/\Delta\Omega_n \approx 0.95$. For modes $|\psi_{13}\rangle$ ($|\psi_{31}\rangle$), reflection is suppressed on the right and enhanced on the left, whereas the opposite occurs for modes $|\psi_{14}\rangle$ ($|\psi_{32}\rangle$).

As argued in the **Methods**, this chirality originates from the broken spatial inversion symmetry of the CCA, which enables interference between eigenmodes and confines the dressed wavefunction to one side or the other of the array. Two main distinctions arise between the two mode pairs: (i) the frequency range over which chirality occurs, which is broader for the superstrong case [compare red lines on the x-axis in **Fig. 4b,c**], and (ii) the smaller and more widely distributed atomic fraction in the more strongly-coupled modes.

We extract the external dissipation rates to the left and right ports, $\gamma_{\text{ext,L}}/2\pi$ and $\gamma_{\text{ext,R}}/2\pi$, for the two sets of modes, and report their ratio $\chi = 10 \log_{10}(\gamma_{\text{ext,R}}/\gamma_{\text{ext,L}})$ in dB [see **Fig. 4f,h**]. The measurements clearly reveal the expected chirality. Numerical simulations based on the imaginary parts of the eigenvalues of a disorder-free non-Hermitian Hamiltonian [see **Methods**] reproduce the main features, but differ in both the background dissipation levels and in the exact qubit frequency at which maximal chirality occurs, which we attribute to disorder [see **Supplementary Note B**]. At the qubit frequency of maximum chirality, the model predicts ideal localization, with either $\gamma_{\text{ext,R}} = 0$ and $\gamma_{\text{ext,L}} \neq 0$ or vice versa. Experimentally, however, we do not reach such ideal values: for modes 13 and 14 we extract $\chi = (-11 \pm 3, 22 \pm 9)$ dB, respectively, and for modes 31 and 32, $\chi = (-15 \pm 3, 20 \pm 5)$ dB, comparable to other recent experimental demonstrations [40]. We attribute

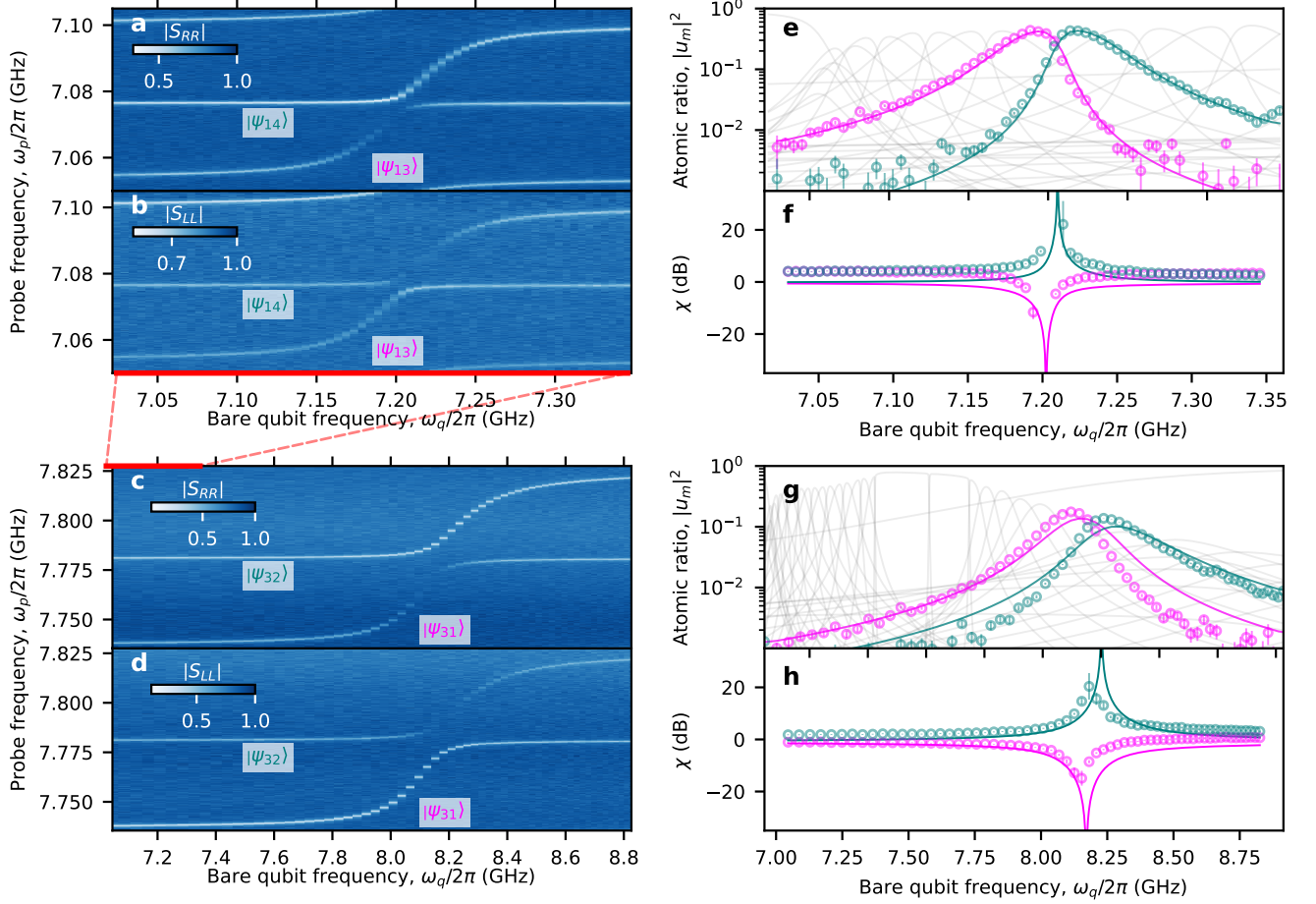


Figure 4. **Experimental signature of chirality.** (a) [b] Magnitude of the reflection spectra from the right [left] port, $|S_{RR}|$ [$|S_{LL}|$], for dressed CCA modes $|\psi_{13}\rangle$ and $|\psi_{14}\rangle$ as a function of the bare qubit frequency. (c) [d] Magnitude of the reflection spectra from the right [left] port, $|S_{RR}|$ [$|S_{LL}|$], for dressed CCA modes $|\psi_{31}\rangle$ and $|\psi_{32}\rangle$ as a function of the bare qubit frequency. The red lines in panels b and c on the x axes, compares the qubit frequency range spanned in the two cases. (e) [g] Extracted atomic ratio $|u_m|^2$, (circles) of dressed CCA modes $|\psi_{13}\rangle$ and $|\psi_{14}\rangle$ [$|\psi_{31}\rangle$ and $|\psi_{32}\rangle$]. Error bars represent the propagated standard deviation of the dressed mode frequencies obtained from fits of the reflection spectra to the input–output response function [see [Supplementary Note B](#)]. The grey lines are the expected atomic participation ratio of each modes according to [Eq. \(1\)](#) (disorder-free). (f) [h] Extracted ratio of external dissipation, $\chi = 10 \log_{10}(\gamma_{\text{ext,R}}/\gamma_{\text{ext,L}})$, reported in dB scale (circles), of dressed CCA modes $|\psi_{13}\rangle$ and $|\psi_{14}\rangle$ [$|\psi_{31}\rangle$ and $|\psi_{32}\rangle$]. Error bars represent the propagated standard deviation from fits of the reflection spectra to the input–output response function [see [Supplementary Note B](#)]. The continuous lines are the expected ratio χ , from a disorder-less non-Hermitian Hamiltonian [see [Methods](#)].

the absence of complete suppression not to a fundamental limitation, but to finite signal-to-noise ratio: small external dissipation rates are masked by intrinsic losses and the noise floor, preventing us from resolving the full chirality predicted by theory.

VI. DIRECTIONAL EMISSION

Directional photon emission has been demonstrated in nanophotonic systems [5, 61], in superconducting waveguides using interference to generate on-demand directional microwave photons [8, 47, 62], and more recently in one-dimensional superconducting CCAs with Rice–

Mele topology [40]. Here, building on the chirality of the dressed CCA modes established in the previous section, we exploit this property to selectively suppress qubit emission toward either the left or the right side of the CCA, focusing on dressed modes $|\psi_{31}\rangle$ and $|\psi_{32}\rangle$. The pulse sequence and corresponding energy diagram of the system are shown in [Fig. 5a–b](#) [see [Methods](#)]. The qubit is first prepared in the middle bandgap in a superposition state $(|g, \text{vac}\rangle + |\psi_{21}\rangle)/\sqrt{2}$ [21]. This state is then transferred into $|\psi_{31}\rangle$ or $|\psi_{32}\rangle$ through a SWAP using a parametric coupling scheme [calibration in [Supplementary Note F](#)] [31]. Finally, the qubit is adiabatically tuned to the point of maximal directional emission via a 120 ns flux ramp [see step 3 of [Fig. 5a–b](#)].

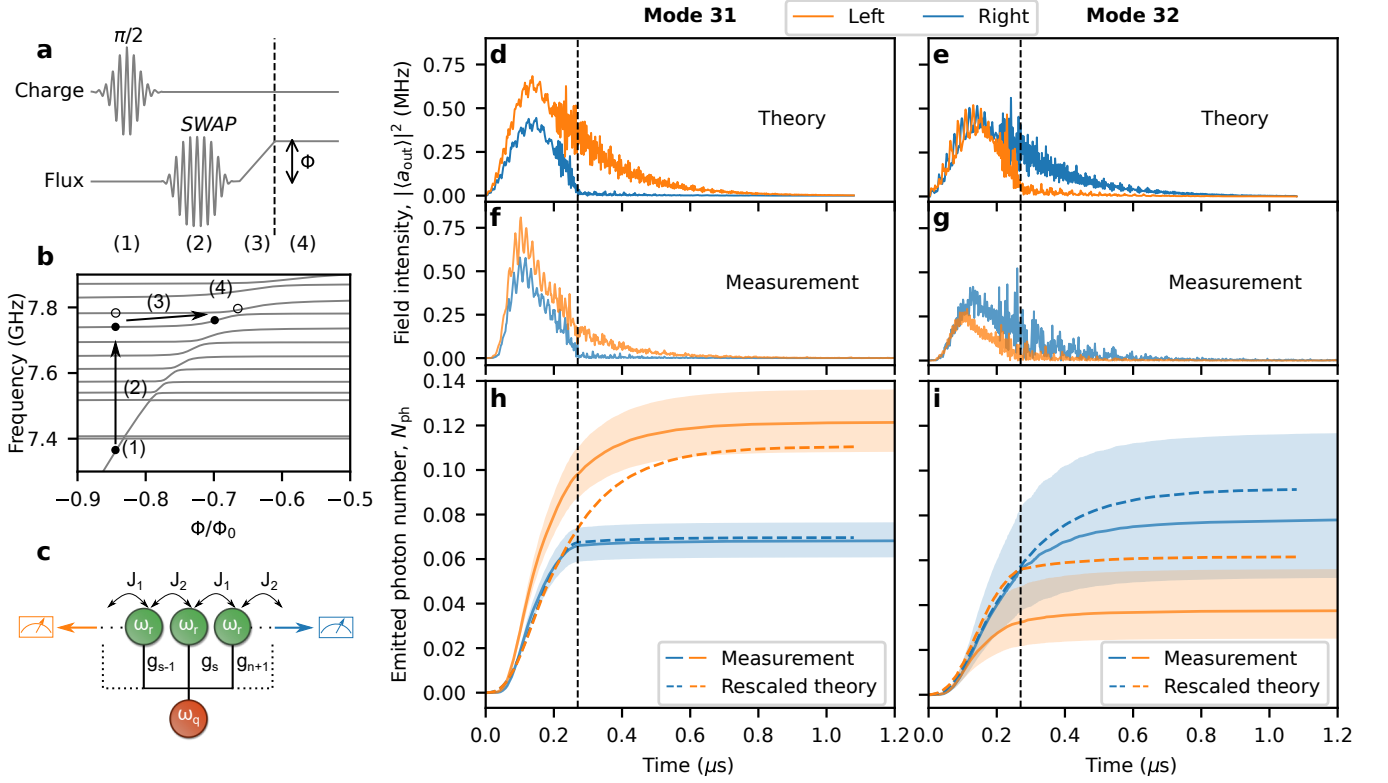


Figure 5. **Directional emission.** (a) Pulse sequence. The qubit is first excited to the state, $(|g, \text{vac}\rangle + |\psi_{21}\rangle)/\sqrt{2}$ (1), it is then transferred to a target dressed CCA mode using a parametric coupling scheme (2). The qubit is adiabatically displaced in frequency (3) to reach the optimal emission point (4). (b) Energy diagram of the system with the pulse sequence. The grey lines represent the dressed CCA modes as a function of the reduced flux, Φ/Φ_0 , threading the SQUID of the transmon. The black dots [circle] show the position of the “excitation” for the steps (1), (2), (3) and (4) as indicated in panel a for mode 31 [32]. (c) Pictorial diagram of the expected emission. The orange (blue) arrows highlight emissions coming from the left (right). This color code is used in the rest of the figure. (d) [e] Simulation of the field intensity $|\langle a_{\text{out}} \rangle|^2$ as a function of time [see Methods], following the protocol in panel a for dressed CCA mode 31 [32]. a_{out} is the outgoing emitted photon field from the left or right side of the CCA. (f) [g] Measured field intensity $|\langle a_{\text{out}} \rangle|^2$, as a function of time, following the protocol in panel a for dressed CCA mode 31 [32]. (h) [i] Emitted photon number N_{ph} , as a function of time for dressed CCA mode 31 [32]. The continuous lines represent the experimental data, where the shaded area is the uncertainty region due to gain calibration error [see Supplementary Note G]. The dashed line is the rescaled theory [see Methods].

In Fig. 5d–e, we show the field intensity, $|\langle a_{\text{out}} \rangle|^2$, to the left and right of the CCA for modes $|\psi_{31}\rangle$ and $|\psi_{32}\rangle$, as obtained from a disorder-free Hamiltonian [see Methods]. Initially, emission is bidirectional, but after the flux ramp [dashed vertical line in Fig. 5d–e], it becomes predominantly leftward for mode $|\psi_{31}\rangle$ and rightward for mode $|\psi_{32}\rangle$. The initial rise of the field intensity reflects the competition between SWAP loading and emission from the mode at rate γ_m , producing a wavepacket with finite rise and exponential tail; without the ramp it decays at γ_m , while the ramp cancels emission on one side and redirects it to the other side. Pronounced oscillations appear at the onset of the ramp, signaling nonadiabatic dynamics, particularly strong for mode $|\psi_{32}\rangle$ whose optimal emission point lies immediately beyond an avoided crossing [hollow circle in Fig. 5b].

In Fig. 5f–g, we present the measured field intensity for modes $|\psi_{31}\rangle$ and $|\psi_{32}\rangle$ to the left and right of the

CCA, averaged over 75×10^6 iterations. The output gain is directly calibrated at the mode frequencies [see Supplementary Note G]. The measurements are in good agreement with the theoretical trends, though they reveal even stronger nonadiabatic behavior for mode $|\psi_{32}\rangle$ than predicted, which we attribute to disorder or distortions in the flux pulses.

We quantify the directional emission by reporting the emitted photon number N_{ph} , obtained by integrating the measured field intensity as a function of time [solid lines in Fig. 5h–j, for details see Supplementary Note H]. For comparison, we overlay rescaled theoretical predictions (dashed lines), where the rescaling accounts for disorder-induced changes in mode localization and hence the external dissipation rates [see Methods].

The directionality of mode m is quantified by

$$\eta_m = \frac{L - R}{L + R}, \quad (2)$$

where L and R denote the emitted photon numbers to the left and right ports, respectively. By definition, $\eta_m = 1$ (-1) corresponds to perfectly left- (right-) directional emission. Experimentally, we obtain $\eta_{31}^{\text{meas}} = 0.279$ and $\eta_{32}^{\text{meas}} = -0.346$, compared to the rescaled theoretical predictions of $\eta_{31}^{\text{theory}} = 0.226$ and $\eta_{32}^{\text{theory}} = -0.196$. The discrepancy between theory and measurement is primarily attributed to gain miscalibration of the measurement chain [see [Supplementary Note G](#)].

Three non-idealities limit the emission protocol: 1) the qubit begins emitting immediately after the SWAP gate and becomes directional only after reaching the optimal emission point; 2) residual nonadiabatic dynamics persist even at the optimal point due to the finite ramp speed; 3) internal losses in both the qubit and the CCA further reduce the overall emission efficiency.

Despite these limitations, the experiment demonstrates controlled, mode-selective directional emission of single photons in a superconducting metamaterial environment.

VII. DISCUSSION

We observe that directionality could be enhanced by preparing the system in the upper APBS [purple line in [Fig. 2a](#)], which allows for direct access of the avoided crossing responsible for chiral emission [see [Ext Data Fig. 6](#)]. In this case, our model predicts nearly ideal performance ($\eta_{31}^{\text{Theo}} = 0.989$, $\eta_{32}^{\text{Theo}} = -0.980$). Even better performances are expected from devices optimized for directional emission, with lower internal loss and ports positioned at CCA antinodes. In this experiment, this was not implemented due to control-electronics limitations.

Beyond directionality, several further opportunities emerge. Extending this experiment to two braided qubits would enable decoherence-free interactions in the continuum [48]. Generalizing to two-dimensional baths [30, 32, 49, 63–65] would provide access to exotic bound states and unconventional transport phenomena. Moreover, this platform offers a testbed for nonlinear multimode quantum optics, where the dynamics could be explored beyond the single-photon regime, both inside the bands and in the bandgaps [66].

Remarkably, our results highlight the role of *coupling engineering* [41]. By tailoring the qubit–CCA connection points, we reshaped the distribution of coupling strengths across the mode spectrum, enhancing interactions with high-frequency symmetric modes while reducing coupling to low-frequency and antisymmetric ones. This design enabled selective access to the superstrong regime and already pushes the system toward multimode *ultrastrong* coupling, with $G_n/\Omega_n \approx 0.05$ at the upper band edge. Extending this strategy to qubits with higher anharmonicity—such as fluxoniums [67], Cooper-pair boxes, or semiconductor quantum dots [68]—would open a path to genuinely non-perturbative physics in multimode QED [69, 70].

VIII. ACKNOWLEDGEMENTS

The authors thank Carlos Vega, Alejandro Gonzalez-Tudela and Shingo Kono for stimulating discussions. This research was funded by the Swiss National Science Foundation (SNSF), Grant number 200021.200418 / 1. This work was supported by the Swiss State Secretariat for Education, Research and Innovation (SERI) under contract number MB22.00081 /REF-1131 -52105. This work was supported as a part of NCCR SPIN, a National Centre of Competence in Research, funded by the Swiss National Science Foundation (grant number 225153). P.S. and V.S. acknowledge support by the Swiss State Secretariat for Education, Research and Innovation (SERI) under contract number UeM019-16. V.S. acknowledges support by the Swiss National Science Foundation through Projects No. 200020.215172, 200021-227992, and 20QU-1.215928. S.F. acknowledges the support of SNF Spark project 221051. D.D.B. acknowledges funding from the European Union - NextGeneration EU, "Integrated infrastructure initiative in Photonic and Quantum Sciences" - I-PHOQS [IR0000016, ID D2B8D520, CUP B53C22001750006]. M.S. acknowledges support from the EPFL Center for Quantum Science and Engineering postdoctoral fellowship. E.D.B. and F.C. acknowledge financial support from European Union-Next Generation EU through projects: Eurostart 2022 'Topological atom-photon interactions for quantum technologies'; PRIN 2022-PNRR No. P202253RLY 'Harnessing topological phases for quantum technologies'; THENCE-Partenariato Estesio NQSTI-PE00000023-Spoke 2 'Taming and harnessing decoherence in complex networks'. The device has been fabricated in the Center of Micro-NanoTechnology (CMi) at EPFL.

Data availability: The data used to produce the plots will be available on Zenodo. All other data are available from the corresponding authors upon request.

Code availability: The codes used to analyze the data and produce the plots will be available on Zenodo.

IX. AUTHOR CONTRIBUTIONS

V.J., D.S., M.S., L.P., and P.S. designed the experiment. D.S., V.J., and S.F. fabricated the devices. V.J. performed the measurements with guidance from M.S. V.J. analyzed the data with guidance from L.P. A.M., E.D.B., V.J., L.P., and M.S. developed the theoretical model; A.M. performed the numerical simulations and derived the effective Hamiltonian, while E.D.B. developed the theory of chirality. V.J., L.P., A.M., D.D.B., and E.D.B. wrote the manuscript with input from all authors. V.S., F.C., and P.S. supervised the work.

X. METHODS

A. Mode-space coupling strength distribution: interference and symmetries

Given the interaction Hamiltonian in Eq. (1), describing the qubit's interaction with a subset of CCA sites, we would like to compute the qubit's coupling strength to each of the CCA normal modes $|\phi_n\rangle$, i.e. the eigenstates of the bare Hamiltonian H_{CCA} with respective eigenstate Ω_n . We then use the form obtained to make some general comments about reaching the *superstrong* coupling regime and the emergence of chiral CCA dressed modes.

The interaction Hamiltonian in the site basis reads

$$H_{\text{INT}} = \sum_{s=1}^N g_s (a_s^\dagger b + \text{H.c.}). \quad (3)$$

Recalling that $|\phi_n\rangle = \sum_{s=1}^N d_{s,n} |s\rangle$, we can express each of the ladder operators a_s as $a_s = \sum_n d_{s,n} \phi_n$, where $|\phi_n\rangle = \phi_n^\dagger |\text{vac}\rangle$. This allows to recast the interaction Hamiltonian in the form

$$H_{\text{INT}} = \sum_n G_n (\phi_n^\dagger b + \text{H.c.}), \quad (4)$$

where

$$G_n = \sum_{s=1}^N d_{s,n}^* g_s. \quad (5)$$

In the case of a standard *small atom*, we have $g_s = g \delta_{s,s_0}$, where s_0 is the index of the coupling point. Then from Eq. (5) we have $G_n = g d_{s_0,n}^*$, and the mode-space coupling distribution is only determined by the amplitude of each CCA mode on cavity s_0 . However, in the multi-site coupling introduced by the *giant atom*, the coupling distribution is affected by interference between the different eigenmode wavefunctions, that can redistribute the qubit-CCA coupling strength among the CCA eigenmodes in an arbitrary and non-trivial way. In this sense, G_n can be understood as a result of a weighted interference of mode $|\phi_n\rangle$ at different cavities.

For instance, a giant atom configuration allows to couple the qubit strongly only to a subset of CCA bare modes around a certain value of quasi-momentum k , corresponding to G_n being peaked around a specific n value. This possibility is intuitively understood given the relation $\Delta k \Delta x > 1$ imposed by Fourier analysis, being Δx the size of the atom (e.g. the number of coupling points). The latter entails that the more the number of coupling points, the smaller number of CCA bare modes will the coupling strength be concentrated to. This is the simple mechanism allowing for selectively reaching the *superstrong* coupling regime for a subset of modes using a giant atom.

In an inversion-symmetric CCA, the CCA bare modes are eigenstates of the inversion symmetry operator \mathcal{P} ,

i.e. they have well defined parity around the inversion center. This entails that, if \mathcal{P} -symmetry is not broken by the (giant) atom, there cannot exist dressed CCA modes localized only to the left or right of the inversion center (chiral CCA modes) and the qubit will couple *only* to even-parity CCA bare modes. On the contrary, if the coupling g_s breaks the \mathcal{P} -symmetry, such chiral CCA modes can emerge at specific qubit frequencies as a result of the mixing of CCA bare modes with even and odd parity.

B. Derivation of the qubit-mediated photon-photon interaction

As shown in section X A the Hamiltonian in Eq. (1) can be written in the basis of the eigenmodes of the CCA as

$$H = \omega_q b^\dagger b - \frac{E_C}{2} b^{\dagger 2} b^2 + \sum_{n=1}^N \Omega_n \phi_n^\dagger \phi_n + G_n (\phi_n^\dagger b + \text{H.c.}), \quad (6)$$

where ϕ_n is the bosonic annihilation operator of the n -th eigenmode of the CCA and $\Omega_n/2\pi$ its frequency.

We are interested in deriving the effective qubit-mediated photon-photon interaction. To do so, we perform a Schrieffer-Wolff transformation [71, 72]

$$H_{\text{eff}} = e^S H e^{-S} = H + [S, H] + \frac{1}{2} [S, [S, H]] + \dots, \quad (7)$$

where S is the generator of the transformation. The Hamiltonian in Eq. (6) can be separated into a free part $H_0 = \sum_{n=1}^N \Omega_n \phi_n^\dagger \phi_n + \omega_q b^\dagger b$, a nonlinearity $H_{\text{nl}} = -\frac{E_C}{2} b^{\dagger 2} b^2$, and the interaction $H_{\text{int}} = \sum_{n=1}^N G_n (\phi_n^\dagger b + \text{H.c.})$. We choose the generator S such that the first-order term in the Schrieffer-Wolff transformation cancels the interaction term, i.e. $[S, H_0] = -H_{\text{int}}$. This imposes

$$S = \sum_{n=1}^N \frac{G_n}{\Delta_n} (\phi_n^\dagger b - \phi_n b^\dagger), \quad (8)$$

for the generator S , where $\Delta_n = \Omega_n - \omega_q$ is the detuning between the n -th mode and the qubit. This choice is well-posed provided that $\Delta_n \neq 0$ for each n , i.e. the qubit is not resonant with any of the CCA bare modes. Keeping terms in Eq. (7) up to second order in G_n , we obtain the effective Hamiltonian

$$H_{\text{eff}} \simeq H_0 + H_{\text{nl}} + \frac{1}{2} [S, H_{\text{int}}] + [S, H_{\text{nl}}] + \frac{1}{2} [S, [S, H_{\text{nl}}]]. \quad (9)$$

Since Eq. (6) conserves the total number of excitations, we can restrict ourselves to a fixed number-of-excitations subspace. In particular, in the single-excitation subspace, where H_{nl} does not appear, the effective Hamiltonian can

be written as

$$H_{\text{eff}} \simeq \sum_{n=1}^N \Omega_n^{\text{eff}} \phi_n^\dagger \phi_n + \omega_q^{\text{eff}} b^\dagger b + \sum_{\substack{n=1 \\ n' \neq n}}^N G_{n,n'} (\phi_n^\dagger \phi_{n'} + \text{H. c.}), \quad (10)$$

where

$$\Omega_n^{\text{eff}} = \Omega_n - \frac{G_n^2}{\Delta_n}, \quad (11)$$

$$\omega_q^{\text{eff}} = \omega_q + \sum_{n=1}^N \frac{G_n^2}{\Delta_n}, \quad (12)$$

$$G_{n,n'} = -\frac{G_n G_{n'} (\Delta_n + \Delta_{n'})}{2\Delta_n \Delta_{n'}}. \quad (13)$$

Thus, an effective photon-photon interaction emerges with a strength $G_{n,n'}$. It is worth noticing that such perturbative approach is valid as long as the G_n/Δ_n ratio is small.

Ext. Data Fig. 3(a-b) compare the eigenfrequencies of the full Hamiltonian in Eq. (6) with the one of effective Hamiltonian in Eq. (10). Despite a small deviation that grows as $\Delta_n \rightarrow 0$, this perturbative approach captures the relevant physics, both in band [**Ext. Data Fig. 3a**] and out of band [**Ext. Data Fig. 3c**]. An example at $\omega_q/2\pi = 8.5$ GHz of the photon-photon coupling matrix $G_{n,n'}$ is shown in **Ext. Data Fig. 3c**, showing how these mediated interactions are stronger for lower-wavelength modes and, interestingly, mix significantly multiple modes at different frequencies [see **Ext. Data Fig. 3d-f**].

C. Theory: qubit-induced chirality

We consider in the following a CCA made by N cavities, at a frequency $\omega_r/2\pi$, coupled with nearest-neighbor hopping rate $J/2\pi$ [see **Ext. Data Fig. 4a**]. In the single-excitation sector, the CCA normal modes are $\Omega_n = \omega_r + 2J \cos \frac{n\pi}{N+1}$, $n = 1, \dots, N$, and form a passband in the energy interval $[\omega_r - 2J, \omega_r + 2J]$. A qubit *locally* coupled to a cavity at position s_0 [see **Ext. Data Fig. 4a**] seeds a set of dressed bound state localized between one of the edges and cavity s_0 when the qubit is fine-tuned to a specific frequency [73], provided that s_0 do not coincide with the CCA inversion center [see **section X A**]. Using the Green's function formalism [49, 74, 75], in general a dressed bound state having energy $\tilde{\omega}_{\text{BS}}$ can be found in correspondence of a real solution of the equation

$$\tilde{\omega}_{\text{BS}} = \omega_q + g^2 \langle s_0 | \mathcal{G}_B(\tilde{\omega}_{\text{BS}}) | s_0 \rangle, \quad (14)$$

where $\omega_q/2\pi$ is the bare qubit frequency, $g/2\pi$ is the qubit's coupling strength to cavity s_0 and $\mathcal{G}_B(z)$ is the CCA's Green's function, defined as $\mathcal{G}_B(z) = \sum_k |\phi_k\rangle\langle\phi_k| / (z - \Omega_k)$. The wavefunction of the bound state corresponds to the residue of $\mathcal{G}_B(z)$ at $z = \tilde{\omega}_{\text{BS}}$. In particular, such state will be localized between one of

the edges and cavity s_0 if $\langle s_0 | \mathcal{G}_B(\tilde{\omega}_{\text{BS}}) | s_0 \rangle = 0$, i.e. if its wavefunction has a *node* at position s_0 . From this follows that the energy of this bound state will correspond to the qubit frequency $\omega_q/2\pi$. In particular, a left-localized state will appear when the bare qubit frequency is resonant with

$$\tilde{\omega}_m^L = \omega_0 + 2J \cos \frac{m\pi}{s_0 + 1}, \quad m = 1, \dots, s_0, \quad (15)$$

while for the right-localized dressed states

$$\tilde{\omega}_p^R = \omega_0 + 2J \cos \frac{p\pi}{N - s_0}, \quad p = 1, \dots, N - s_0 - 1, \quad (16)$$

regardless of the coupling strength $g/2\pi$ [see **Ext. Data Fig. 4b**]. Their localization can be verified using a *chirality quantifier* $Q_m(\omega_q)$ for each dressed mode $|\psi_m\rangle$ defined as

$$Q_m(\omega_q) = \frac{\sum_{s=0}^{s_0} |\langle s | \psi_m \rangle|^2 - \sum_{s=s_0+1}^N |\langle s | \psi_m \rangle|^2}{\sum_{s=0}^N |\langle s | \psi_m \rangle|^2}, \quad (17)$$

which take values in $[-1, 1]$, reaching its maximum (minimum) for a mode completely localized to the left (right) of cavity s_0 . In **Ext. Data Fig. 4i-j**, we plot Q_m for the same pair of modes at different values of g/J , confirming that perfect localization happens at the predicted qubit frequencies regardless of g/J . Notably, when the qubit coupling is stronger, the chirality quantifier exhibits a broader peak around the predicted frequency [see **Ext. Data Fig. 4m**] and the APR goes down [see **Ext. Data Fig. 4n**], signaling that the localized modes become mostly photonic. Thus, we predict a better efficiency in the directional emission protocol, introduced in **section VI**, for strongly coupled qubits.

As shown in the experiment, a *superstrong* coupling can be reached with the aid of a giant atom. We now investigate whether chiral localization of the eigenmodes is possible also in this case. To show this, if $g_s/2\pi$ is the coupling strength of the giant atom to cavity at position s , we introduce an effective cavity $|\chi\rangle$ defined as $|\chi\rangle = \bar{g}^{-1} \sum_s g_s |s\rangle$, where $\bar{g}^2 = \sum_s g_s^2$, which allows us to express Eq. (14) for a giant atom as [49],

$$\tilde{\omega}_{\text{BS}} = \omega_q + \bar{g}^2 \langle \chi | \mathcal{G}_B(\tilde{\omega}_{\text{BS}}) | \chi \rangle \quad (18)$$

and the node condition as $\langle s_0 | \mathcal{G}_B(\tilde{\omega}_{\text{BS}}) | \chi \rangle \approx 0$. For instance, the latter is satisfied at frequencies in Eq. (15) provided that $G_{m_0}/\delta\omega \ll 1$, being $\delta\omega = |\tilde{\omega}_m^L - \Omega_{m_0}|$, where $\Omega_{m_0}/2\pi$ is the frequency of the CCA bare mode quasi-resonant to a given $\tilde{\omega}_m^L$ and, accordingly, $G_{m_0}/2\pi$ is the coupling to such mode. If this is true, maximum localization is obtained for

$$\omega_q = \tilde{\omega}_{\text{BS}} - \bar{g}^2 \langle \chi | \mathcal{G}_B(\tilde{\omega}_{\text{BS}}) | \chi \rangle, \quad (19)$$

now bearing a dependency on the average coupling strength \bar{g} , which introduces a shift between the chiral mode and the qubit frequency. This can be estimated as

$|\langle \chi | \mathcal{G}_B(\tilde{\omega}_{BS}) | \chi \rangle| \sim (\delta\omega)^{-1}$, entailing that the stronger the coupling \bar{g} , the bigger the shift.

Condition $G_{m_0}/\delta\omega \ll 1$ can be achieved easily noticing that the mode $|\phi_{m_0}\rangle$ will be anti-symmetric with respect to cavity s_0 , meaning that if the coupling g_s is symmetric around cavity s_0 , G_{m_0} will be highly-suppressed [see discussion in [section X A](#)]. Thus, in [Ext. Data Fig. 4](#) we study a giant atom coupled to 5 cavities, with $g_s/2\pi$ having a truncated Gaussian shape centered at s_0 . The average coupling matches the *small atom* case, i.e. $\bar{g} = \sqrt{\sum_s g_s^2} = g_{s_0}$. Although localization is still observed regardless of \bar{g} [[Ext. Data Fig. 4d](#)], different coupling strength affects significantly both the spectrum [[Ext. Data Fig. 4g-h](#)] and the chirality quantifier [[Ext. Data Fig. 4k-l](#)]. In particular, if $\bar{g}/J > 1$ changing the qubit frequency induces a slow displacement of the eigenfrequencies and the qubit frequency is strongly shifted from the chiral modes frequencies. This is better visible comparing Q_m for a fixed pair of modes at different \bar{g}/J values [[Ext. Data Fig. 4o](#)]. Notice that this coupling configuration highly enhances the coupling to low-wavelength modes, resulting in the peaks in the chirality quantifier for different dressed modes to start overlapping with each other at the same bare qubit frequency. This means that, while localization in the *small atom* system results from fine tuning of the parameter, in a *giant atom* system the qubit can induce localization of a big subset of modes at the same time, removing the need for fine tuning.

Our argument is independent on the detail of the bath provided that the localization problem for a small qubit admits a set of localized solutions. Thus, it explains also the results in the present experiment.

D. Simulation of the losses

[Fig. 4](#) presents simulations of mode dissipation as a function of the bare qubit frequency, $\omega_q/2\pi$. These simulations employ the non-Hermitian Hamiltonian formalism, which is derived similarly to that in Refs. [[27](#), [28](#)]. Here, j and l are indices of the Hamiltonian matrix. The non-Hermitian Hamiltonian is given by:

$$H_{j,l}^{\text{Non-Herm}} = \begin{cases} \kappa_{\text{int}}, & \text{if } j = l = \{1, 44\}, \\ \kappa_q, & \text{if } j = l = 45, \\ \kappa_{\text{ext,L}}, & \text{if } j = l = 1, \\ \kappa_{\text{ext,R}}, & \text{if } j = l = 44, \\ \kappa'_{\text{ext,L}}, & \text{if } j = l = 2, \\ \kappa'_{\text{ext,R}}, & \text{if } j = l = 43, \\ 2\sqrt{\kappa_{\text{ext,L}}\kappa'_{\text{ext,L}}}, & \text{if } (j, l) = (1, 2) \text{ or } (2, 1), \\ 2\sqrt{\kappa_{\text{ext,R}}\kappa'_{\text{ext,R}}}, & \text{if } (j, l) = (44, 43) \text{ or } (43, 44). \end{cases} \quad (20)$$

where $\kappa_{\text{int}}/2\pi$ is the internal dissipation rate of the cavity sites, $\kappa_q/2\pi$ is the bare qubit total dissipation rate, $\kappa_{\text{ext,L(R)}}/2\pi$ are the external coupling rates of the left (right) cavity to the left (right) measurement port, and $\kappa'_{\text{ext,L(R)}}/2\pi$ are the external coupling rates of the second to left (right) cavity to the left (right) measurement port.

The imaginary part of the eigenvalues of the non-Hermitian Hamiltonian provides the dissipation profile of the eigenmodes:

$$\text{Im}(\text{Eig}(H^{\text{Non-Herm}})) = 2\vec{\gamma}_{\text{Tot}}, \quad (21)$$

where $\vec{\gamma}_{\text{Tot}} = \vec{\gamma}_{\text{int}} + \vec{\gamma}_{\text{ext,L}} + \vec{\gamma}_{\text{ext,R}}$ is the total dressed dissipation rate vector for all eigenmodes.

By setting certain dissipation rates to zero, we can selectively extract the external dissipation rates. Specifically, setting $\kappa_{\text{int}} = \kappa_q = 0$ and either $\kappa_{\text{ext,L}} = \kappa'_{\text{ext,L}} = 0$ or $\kappa_{\text{ext,R}} = \kappa'_{\text{ext,R}} = 0$ allows the extraction of the right or left external dissipation rates, respectively, as formalized in:

$$\text{Im}(\text{Eig}(H^{\text{Non-Herm}})) = 2 \begin{cases} \vec{\gamma}_{\text{ext,R}} & \text{if } \kappa_{\text{ext,L}} = \kappa'_{\text{ext,L}} = \kappa_{\text{int}} = \kappa_q = 0, \\ \vec{\gamma}_{\text{ext,L}} & \text{if } \kappa_{\text{ext,R}} = \kappa'_{\text{ext,R}} = \kappa_{\text{int}} = \kappa_q = 0. \end{cases} \quad (22)$$

The extraction of the bare CCA dissipations is described in [Supplementary Note B](#). The external dissipation rates, $\vec{\gamma}_{\text{ext,R}}$ and $\vec{\gamma}_{\text{ext,L}}$, are sensitive to disorder in the resonant frequencies of the CCA sites. This sensitivity arises because disorder affects mode localization, thereby altering the field amplitude at the coupling ports. Further details are provided in [Supplementary Note B](#).

E. Simulation of the open dynamics

The simulation of the open dynamics is performed by solving the Lindblad master equation

$$\frac{d}{dt}\rho = -i[H, \rho] + \kappa_q \mathcal{D}[b]\rho + \sum_{s=1}^N \kappa_s \mathcal{D}[a_s]\rho, \quad (23)$$

where $\mathcal{D}[O]\rho = O\rho O^\dagger - (O^\dagger O\rho + \rho O^\dagger O)/2$ is the dissipator and κ_s is the total dissipation rate of site s [see [Eq. \(20\)](#)]. The system preserves a weak $U(1)$ symmetry and we can thus work in the subspace containing only zero and one excitations in total. The time evolution is then numerically integrated using the `QuantumToolbox.jl` package in Julia [[76](#)].

F. Device parameters

Device parameters are summarized in [Ext. Data Tab. 1](#). The extraction of CCA and qubit parameters is described in [Supplementary Note B](#) and [Supplementary Note C](#), respectively.

G. Pulse sequence in Figure 3

The pulse sequence employed in Fig. 3 begins with a 40 ns DRAG π -pulse with the qubit initialized at $\omega_q/2\pi = 7.62$ GHz, corresponding to a dressed state frequency of $\tilde{\omega}_q/2\pi = 7.43$ GHz. Subsequently, a constant flux offset is applied, with a holding time τ ranging from 16 to 500 ns in 4 ns steps. The ramp time for this flux offset is 2.4 ns. Finally, the qubit is returned to its initial frequency, and its state is read out for 2 μ s via conventional dispersive readout.

H. Pulse sequence in Figure 5

The pulse sequence employed in Fig. 5 begins with a 40 ns DRAG $\pi/2$ -pulse, with the qubit initialized at $\omega_q/2\pi = 7.56$ GHz, corresponding to a dressed state frequency of $\tilde{\omega}_q/2\pi = 7.384$ GHz. The qubit state is transferred to mode 31 (32) using a supergaussian parametric SWAP pulse at 356.5 MHz (399.5 MHz) for 160 ns. The qubit frequency is then ramped to $\omega_q/2\pi = 8.15$ GHz for mode 31 and to $\omega_q/2\pi = 8.22$ GHz for mode 32, with a ramp time of 120 ns. This fast ramp rate causes non-adiabatic transitions between dressed CCA modes 31 and 32, and with other dressed CCA modes [see [Supplementary Note H](#)]. However, these non-adiabatic transitions can be avoided by omitting the ramp from the pulse sequence, initializing the qubit from the upper APBS as shown in [Ext Data Fig. 6](#).

I. Emission measurements

a. Rescaling. In Fig. 5, we compare the experimental data with rescaled theoretical predictions. The rescaling compensates for the absence of disorder in the simulations, since implementing the exact disorder realization of our device is not feasible. To account for this, the theory is rescaled by the ratio

$$\Gamma_{L(R)}^{(i)} = \frac{\gamma_{\text{ext},L(R)}^{i,\text{Simu}}}{\gamma_{\text{ext},L(R)}^{i,\text{Meas}}},$$

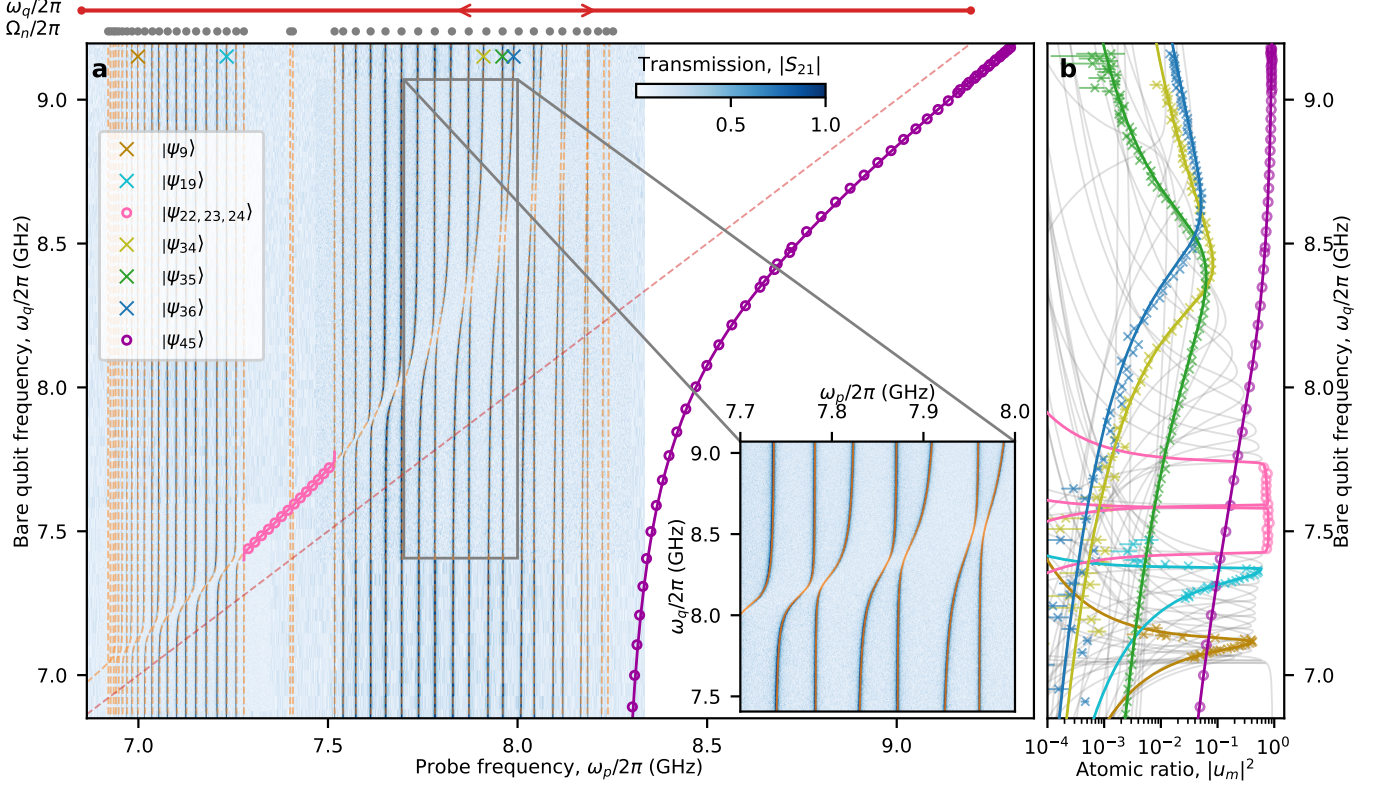
which corrects for disorder-induced modifications of eigenmode localization not captured in the disorder-free Hamiltonian. Here, $\gamma_{\text{ext},L(R)}^{i,\text{Simu}}$ and $\gamma_{\text{ext},L(R)}^{i,\text{Meas}}$ denote the simulated and measured external dissipation rates, respectively, for mode i from the left (right) port. Since the emitted photon number scales linearly with the external dissipation ($n \propto \gamma_{\text{ext},L(R)}$), this procedure provides a consistent comparison. We find good agreement for mode 31, whereas for mode 32 noticeable discrepancies remain, which we mainly attribute to uncertainties in the gain calibration [see [Supplementary Note G](#)].

b. Calibration of the gain: The gain for mode 31 and 32 is calibrated using AC-Stark shift measurements. A

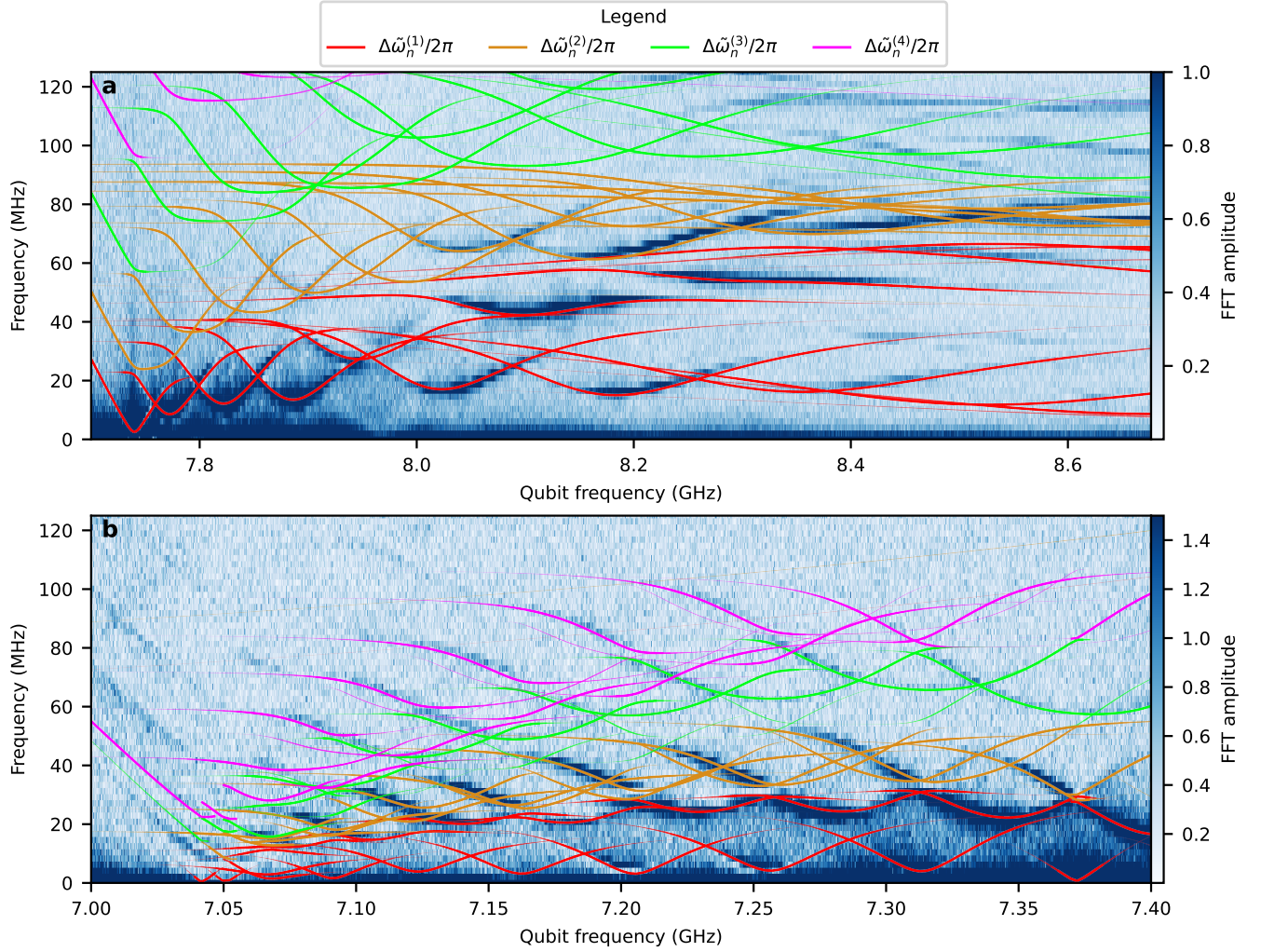
detailed description of the calibration is in [Supplementary Note G](#). The calibration is performed with the bare qubit set to the initial frequency for the directional emission protocol at $\omega_q/2\pi = 7.55$ GHz, corresponding to a dressed qubit frequency of $\tilde{\omega}_q/2\pi = 7.38$ GHz. Below we briefly describe the calibration sequence:

1. **Measurement of the modes' dispersive shift:** The frequency response of modes 31 and 32 are measured using single-tone spectroscopy in reflection with the qubit in its ground state, then the qubit in its excited state. This allows for the extraction of the dispersive shift.
2. **AC-Stark shift measurement:** The qubit AC-Stark shift is measured as a function of the input power in modes 31 and 32 from both the left and right port of the CCA. This allows for a precise extraction of the attenuation for both modes from both sides of the CCA.
3. **Extraction of the gain:** The gain is extracted by measuring modes 31 and 32 using single-tone spectroscopy in reflection from both the left and the right side. Knowing that the baseline of the reflected signal should be equal to 1 for a calibrated system, i.e. $\langle a_{\text{out}} \rangle = \langle a_{\text{in}} \rangle$, we can find the gain for both modes from both sides of the CCA.

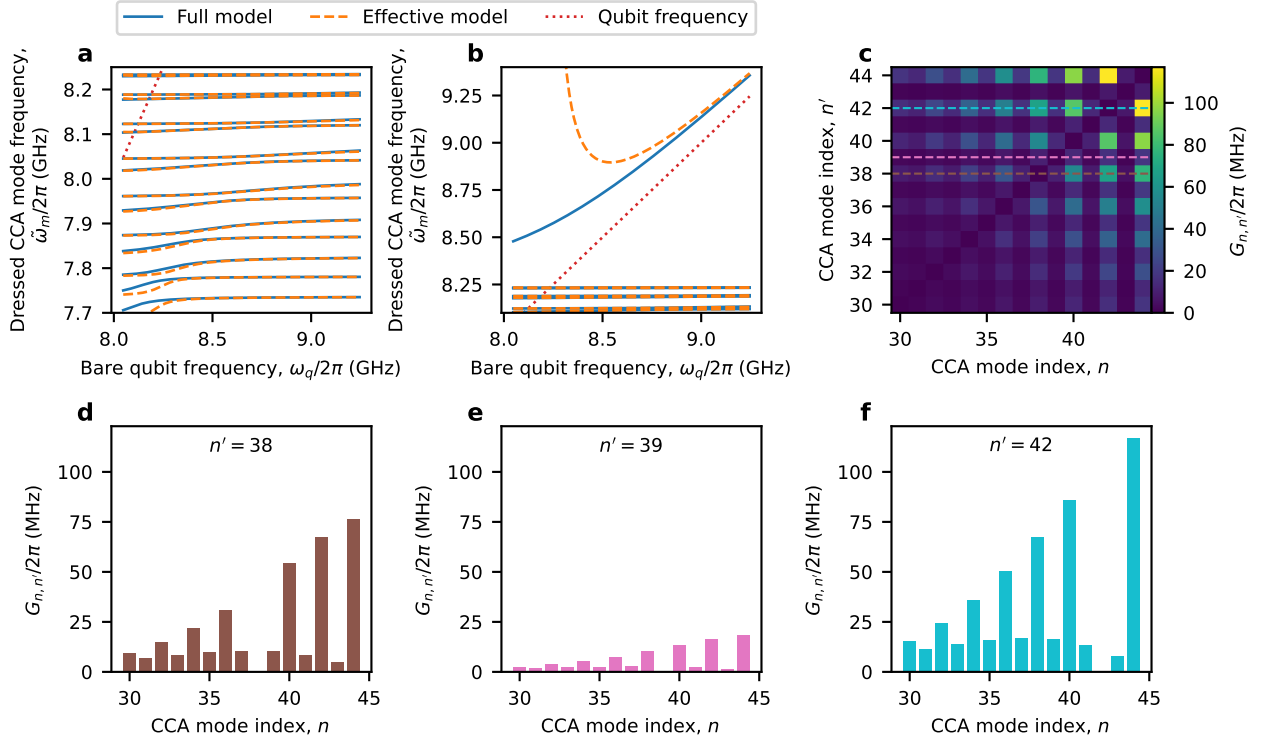
XI. EXTENDED DATA FIGURE



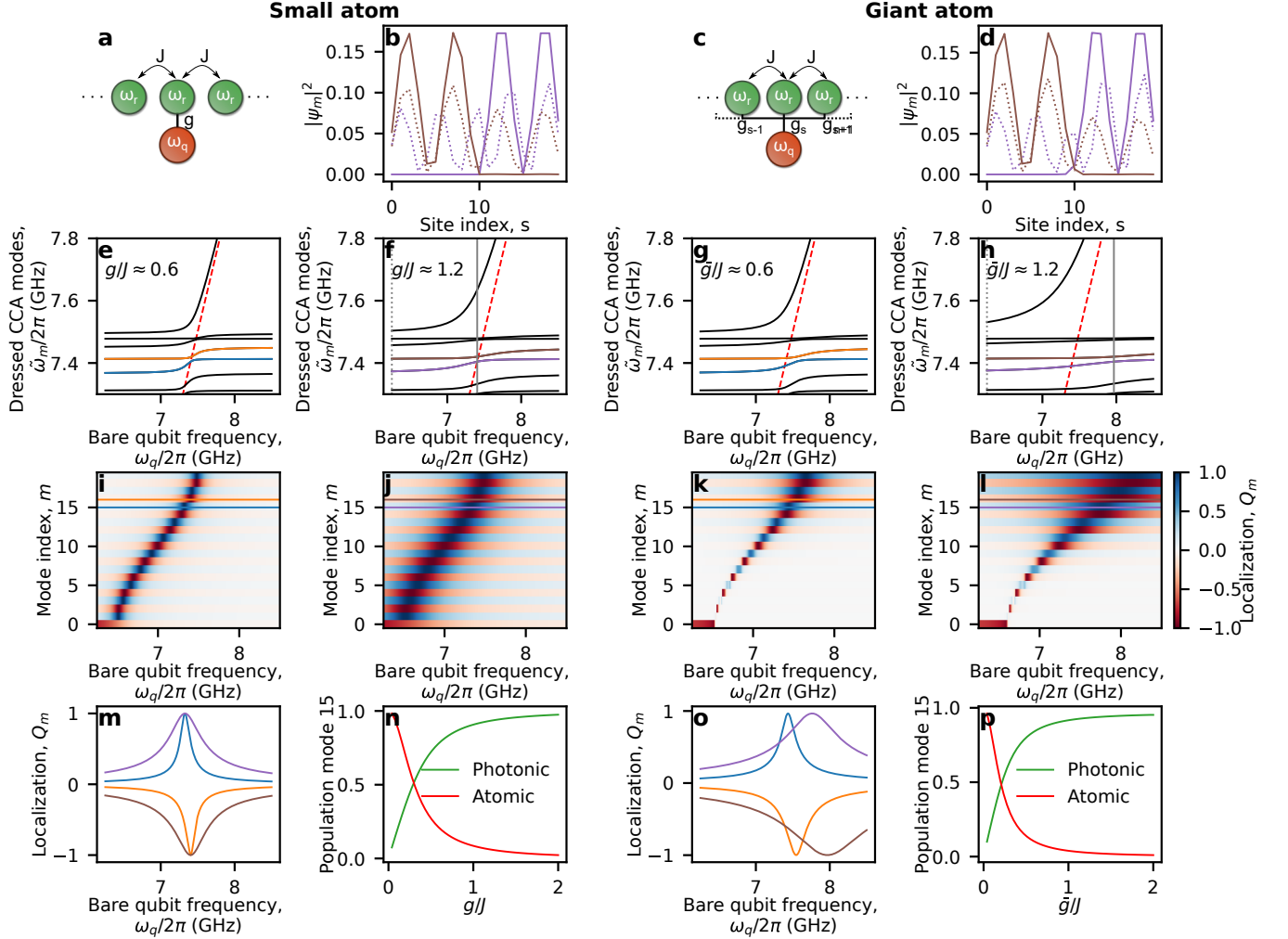
Extended Data Figure 1. **Steady-state interaction of a giant atom interacting with a structured photonic bath (comparison to a model including disorder)** (a) Single-tone transmission of the CCA as a function of bare qubit frequency $\omega_q/2\pi$. The dressed qubit frequency extracted from two-tone spectroscopy is shown above the upper band (purple circles) and inside the middle bandgap (pink circles). Model predictions according to Eq. (1) for the dressed qubit are shown as purple and pink lines, and the bare qubit frequency as a red dashed line. Crosses indicate the dressed CCA modes analyzed in panel b. Inset: zoom-in from $\omega_p/2\pi = 7.7$ GHz to 8 GHz; orange lines show eigenvalues, $\tilde{\omega}_m/2\pi$, of the fitted disorder-free model according to Eq. (1). The orange (dashed) lines are the eigenvalues of the fitted model including resonant frequency disorder with standard deviation $\sigma = 21.8$ MHz. (b) Atomic participation ratio of each eigenmode, $|u_m|^2$. Grey lines: expected atomic participation ratio, $|u_m|^2$, of each modes according to Eq. (1); circles and crosses: values extracted from two-tone and single-tone spectroscopy, respectively (error bars from the standard deviation of fitted dressed-mode frequencies), using $|u_m|^2 = d\tilde{\omega}_m/d\omega_q$. Mode labels are indicated in the legend in panel a.



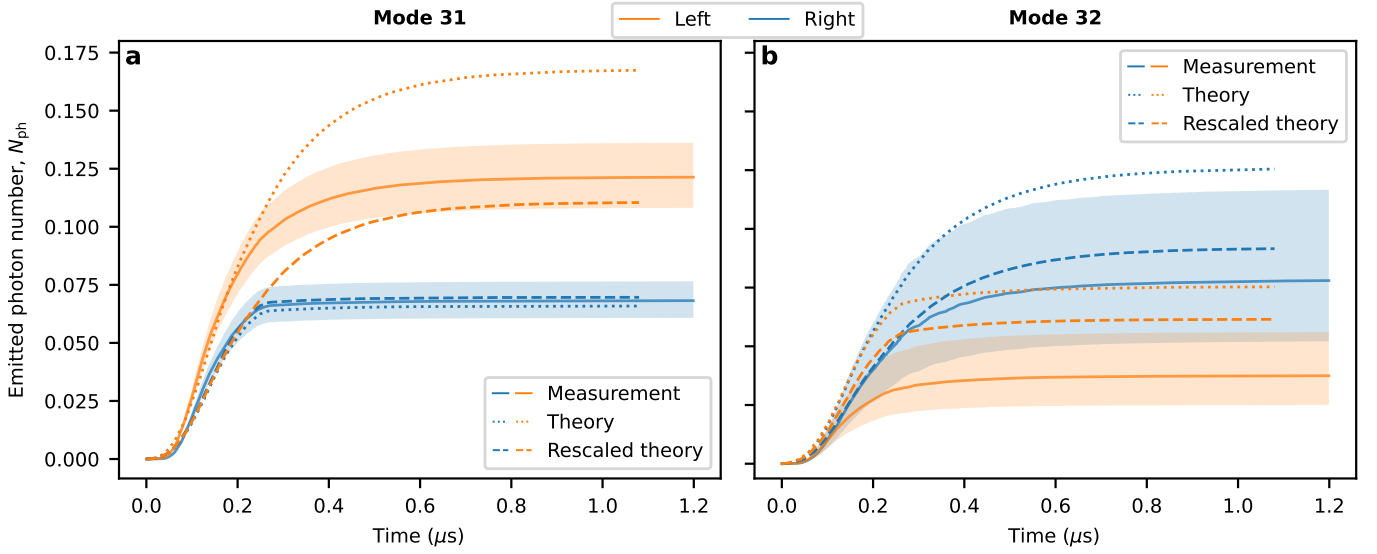
Extended Data Figure 2. **Zooms-in on the FFT of the time domain trace of Fig. 3.** The colormap is saturated to highlight the features. **(a)** Zoom in the upper band. **(b)** Zoom in the lower band. The red lines corresponds to $\Delta\tilde{\omega}_n^{(1)}/2\pi$, the orange lines to $\Delta\tilde{\omega}_n^{(2)}/2\pi$, the green line to $\Delta\tilde{\omega}_n^{(3)}/2\pi$ and the purple line to $\Delta\tilde{\omega}_n^{(4)}/2\pi$.



Extended Data Figure 3. **Photon-Photon Mode Hybridization.** (a) [(b)] Dressed CCA mode frequency comparison between the full Hamiltonian, $\tilde{\omega}_n/2\pi$, (solid blue line) and the effective Hamiltonian, $\tilde{\omega}_{n,\text{eff}}/2\pi$, (dashed orange line), in the upper band [upper bandgap]. The dotted red line corresponds to the bare qubit frequency, $\omega_q/2\pi$. (c) Photon-photon coupling matrix, which increases for higher mode indices. (d), (e) and (f), line cuts of the photon-photon coupling matrix, for $n' = 37$, 38 and 41, respectively.



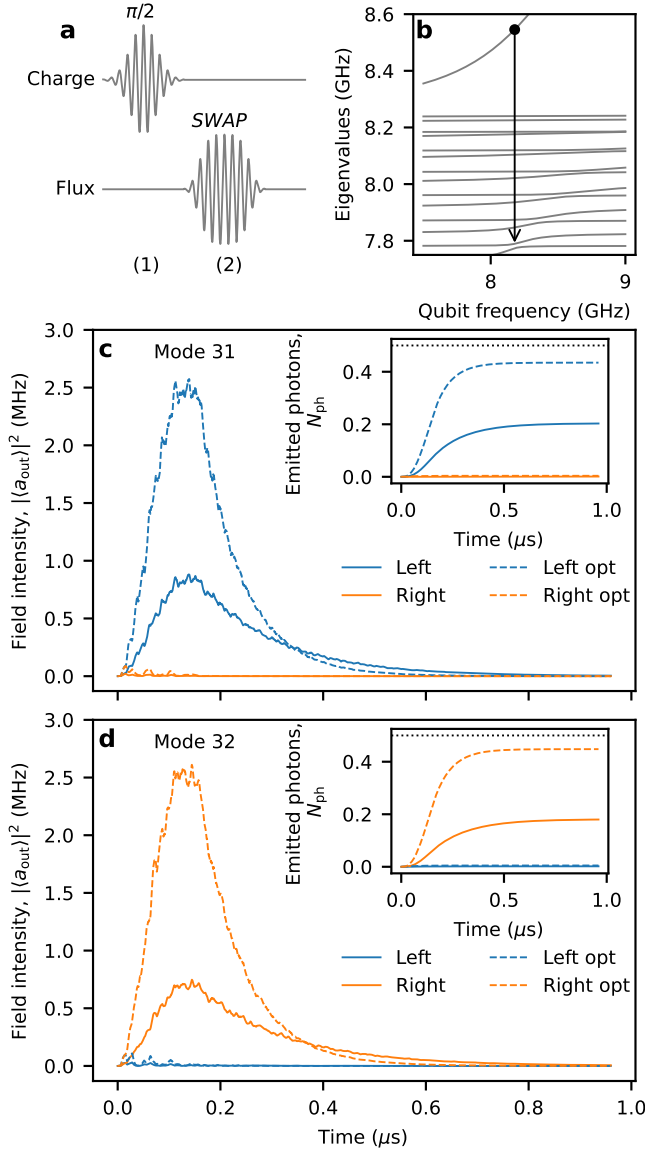
Extended Data Figure 4. **Understanding chirality.** (a,c) Schematic of a qubit coupled *locally* [a] or *non-locally* [c] to a homogeneous 1D CCA. (b,d) Localization of the pair of modes highlighted in purple and brown in panels f,h, shown for qubit frequencies where the modes are delocalized (dotted) and localized (solid). (e,f) Spectrum as a function of the bare qubit frequency $\omega_q/2\pi$ for a small atom with $g/J = 0.6$ [e] and $g/J = 1.2$ [f]. (g,h) Spectrum for a giant atom with $\bar{g}/J = 0.6$ [g] and $\bar{g}/J = 1.2$ [h], where the qubit couples to five cavities with a truncated Gaussian profile. In all cases, $N = 20$, $g = \bar{g} = \sqrt{\sum_s g_s^2}$, $\omega_r = 28J$, $J/2\pi = 0.25$ GHz, and the qubit couples to cavity 10 (red circle). The red dashed line follows the bare qubit frequency. Blue/orange and purple/brown lines highlight modes 15 and 16 for $g/J = 0.6$ and $g/J = 1.2$, respectively. (i-l) Localization of the dressed CCA modes Q_m as a function of $\omega_q/2\pi$, corresponding to panels e-h. (m,o) Linecuts of Q_m for modes 15 and 16 at $g/J = 0.6$ and $g/J = 1.2$ for the small atom [m] and giant atom [o]. (n,p) Photonic (green) and atomic (red) fractions of dressed mode 15 as a function of g/J , evaluated at the qubit frequency where the mode is maximally localized, for the small atom [n] and giant atom [p].



Extended Data Figure 5. **Emitted photon number** N_{ph} . Same measurement/data as shown in Fig. 5h–i, including non rescaled theory. Emitted photon number, N_{ph} , during the directional emission protocol for mode $|\psi_{31}\rangle$ panel **a** and mode $|\psi_{32}\rangle$ panel **b**. The continuous lines represent the experimental data, where the shaded area is the uncertainty region due to gain calibration error [see Supplementary Note G]. The dotted line is the theory. The dashed line is theory rescaled with $\gamma_{\text{ext,Simulation}}/\gamma_{\text{ext,Measured}}$.

Metamaterial			
Parameter	Value	Method	
L_g	16.80 nH	Fit of the metamaterial spectrum + microwave simulation.	
C_g	23.04 fF		
C_1	1.84 fF	Fit of the metamaterial spectrum	
C_2	2.72 fF		
C'	0.38 fF		
C''	0.13 fF		
Z_r	789 Ω		
$\omega_r/2\pi$	7.749 GHz		
$J_1/2\pi$	258.8 MHz		
$J_2/2\pi$	370.5 MHz		
$J'/2\pi$	47.5 MHz		
$J''/2\pi$	12.7 MHz		
$J'''/2\pi$	5.19 MHz		
$J''''/2\pi$	2.1 MHz		
$\kappa_{\text{ext,R}}/2\pi$	13.67 ± 0.32 MHz		Fit of the metamaterial dissipations.
$\kappa_{\text{ext,L}}/2\pi$	11.12 ± 0.14 MHz		
$\kappa'_{\text{ext,R}}/2\pi$	52.64 ± 7.78 kHz		
$\kappa'_{\text{ext,L}}/2\pi$	28.70 ± 2.69 kHz		
$\kappa_{\text{int}}/2\pi$	590 ± 26 kHz		
Qubit			
Parameter	Value	Method	
$\omega_{q,0}/2\pi$	9.29 GHz	Fit of the metamaterial spectrum vs flux.	
$E_C/2\pi$	318 MHz	High-power two-tone spectroscopy measurement.	
$E_J(0)/2\pi$	36.39 GHz	-	
$E_J(0)/E_C$	114	-	
T_1	871 ± 65 ns	Qubit T_1 measurements at the sweet spot.	
T_2	1059 ± 213 ns	Qubit T_2 measurements at the sweet spot.	
Readout resonator			
Parameter	Value	Method	
$\omega_{RO}/2\pi$	4.60 GHz	Fit of the readout resonator frequency vs flux.	
$g/2\pi$	89 MHz	Fit of the readout resonator frequency vs flux.	
$\gamma_{\text{RO,ext}}/2\pi$	1.64 ± 0.03 MHz	Fit of the resonator with the qubit detuned.	
$\gamma_{\text{RO,int}}/2\pi$	330 ± 43 kHz	Fit of the resonator with the qubit detuned.	

Extended Data Table 1. List of the system parameters.



Extended Data Figure 6. **Optimized emission simulation.**

(a) Pulse sequence. Step (1): The APBS is first excited in the state $(|\text{vac}, g\rangle + |\psi_{45}\rangle)/\sqrt{2}$. Step (2): The state is transferred to the mode of interest with a SWAP gate. (b) Energy diagram. The APBS is initialized at the qubit frequency corresponding to the black dot, and then transferred to the mode displaying directionality (arrow). (c) and (d) Simulation of the field intensity, $|\langle a_{\text{out}} \rangle|^2$, for modes $|\psi_{31}\rangle$ and $|\psi_{32}\rangle$, respectively, as a function of time. The continuous lines show the optimal emission for the device parameters [see Ext. Data Tab. 1], while the dashed lines show the emission for a similar device with better loss parameters ($\kappa_{\text{int}}/2\pi = 75$ kHz, $\kappa_{\text{ext,L}}/2\pi = \kappa_{\text{ext,R}}/2\pi = 50$ MHz and $\kappa_q/2\pi = 16$ kHz). The insets show the emitted photon number, N_{ph} , as a function of time. The dotted black line indicates the theoretical maximum number of emitted photons.

Supplementary Information A: Model

1. Metamaterial

In this section we derive the Hamiltonian of the bare metamaterial. The derivation in this section is largely inspired from our previous work [28]. The metamaterial circuit consists of a chain of $N = 44$ capacitively coupled LC resonators. Each resonator has an inductance L_g and capacitance C_g to ground. The coupling between resonators is dimerized such that the capacitance inside a unit-cell is C_1 and the capacitance between unit-cells is C_2 . The potential energy in the inductors is expressed as

$$E_L = \frac{1}{2L_g} \sum_{s=1}^N \varphi_s^2, \quad (\text{A1})$$

where φ_s is the flux at node s . The total kinetic energy stored in the chain's capacitors is given by

$$\begin{aligned} E_K = & \frac{C_g}{2} \sum_{n=1}^N \dot{\varphi}_s^2 \\ & + \frac{C_1}{2} \sum_{s=1}^{N/2} (\dot{\varphi}_{2s-1} - \dot{\varphi}_{2s})^2 \\ & + \frac{C_2}{2} \sum_{s=1}^{N/2-1} (\dot{\varphi}_{2s} - \dot{\varphi}_{2s+1})^2 \\ & + \frac{1}{2} \sum_{\substack{i,j \\ 2 \leq |i-j| \leq 4}} C_{i,j} (\dot{\varphi}_i - \dot{\varphi}_j)^2, \end{aligned} \quad (\text{A2})$$

where $\dot{\varphi}_s$ is the electric potential at node s . The $C_{i,j}$ terms are taken into account up to order 4 and represent the stray capacitances between higher order neighbors. The higher order stray capacitances are expressed as C' , C'' and C''' , for order 2,3 and 4, respectively. Due to the high-impedance of the resonators, the mutual inductance can be neglected. The Lagrangian of the circuit is,

$$\mathcal{L} = E_K - E_L. \quad (\text{A3})$$

We will use its matrix form,

$$\mathcal{L} = \frac{1}{2} (\dot{\boldsymbol{\varphi}}^T [C] \dot{\boldsymbol{\varphi}} - \boldsymbol{\varphi}^T [L^{-1}] \boldsymbol{\varphi}), \quad (\text{A4})$$

with the vectors $\dot{\boldsymbol{\varphi}}^T = (\dot{\varphi}_1, \dot{\varphi}_2, \dots, \dot{\varphi}_N)$ and $\boldsymbol{\varphi}^T = (\varphi_1, \varphi_2, \dots, \varphi_N)$. The capacitance matrix is defined as,

$$[C] = \begin{pmatrix} C_\Sigma & -C_1 & -C' & -C'' & \dots & 0 \\ -C_1 & C_\Sigma & -C_2 & -C' & \ddots & \vdots \\ -C' & -C_2 & C_\Sigma & -C_1 & \ddots & \vdots \\ \vdots & \ddots & \ddots & \ddots & \ddots & -C' \\ \vdots & \ddots & \ddots & \ddots & \ddots & -C_1 \\ 0 & \dots & \ddots & -C' & -C_1 & C_\Sigma \end{pmatrix}, \quad (\text{A5})$$

with C_Σ being the total capacitance of a resonator. The inductance matrix is defined as,

$$[L^{-1}] = \frac{1}{L_g} \mathbf{I} \quad (\text{A6})$$

where \mathbf{I} is the identity matrix. The exact Hamiltonian takes the form,

$$H_{CCA} = \sqrt{[C^{-1}][L^{-1}]}. \quad (\text{A7})$$

The eigenvalues of the Hamiltonian above are used to fit the bare CCA modes' frequencies to extract the circuit parameters of the Hamiltonian according to the method described in [28].

One can obtain an analytical form of the Hamiltonian by neglecting the higher order terms, $C_1 C_2$, C_1^2 , C_2^2 , and higher order stray capacitances, in the inversion of the capacitance matrix. Doing so, the inverse of the capacitance matrix becomes,

$$[C^{-1}] = L_g \omega_r^2 \begin{pmatrix} 1 & \beta_1 & 0 & \dots & \dots & 0 \\ \beta_1 & 1 & \beta_2 & \ddots & \ddots & \vdots \\ 0 & \beta_2 & 1 & \beta_1 & \ddots & \vdots \\ \vdots & \ddots & \ddots & \ddots & \ddots & \vdots \\ \vdots & \ddots & \ddots & \ddots & \ddots & \beta_1 \\ 0 & \dots & \ddots & \ddots & \beta_1 & 1 \end{pmatrix}, \quad (\text{A8})$$

with $\omega_r = 1/\sqrt{L_g C_\Sigma}$ and $\beta_i = C_i/C_\Sigma$.

The Hamiltonian can be rewritten using the Legendre transform,

$$H_{CCA} = \frac{1}{2} \mathbf{Q}^T [C^{-1}] \mathbf{Q} + \frac{1}{2} \boldsymbol{\varphi}^T [L^{-1}] \boldsymbol{\varphi} \quad (\text{A9})$$

with $\mathbf{Q} = \partial \mathcal{L} / \partial \dot{\boldsymbol{\varphi}}$ the conjugate charge variable and $\mathbf{Q}^T = (Q_1, Q_2, \dots, Q_N)$. One gets the Hamiltonian,

$$\begin{aligned} H_{CCA} = & \frac{1}{2} \sum_{s=1}^N L_g \omega_r^2 Q_s^2 \\ & + \frac{1}{2} \sum_{s=1}^N \frac{1}{L_g} \varphi_s^2 \\ & + \frac{L_g \omega_r^2 \beta_1}{2} \sum_{s=1}^{N/2} (Q_{2s-1} Q_{2s} + Q_{2s} Q_{2s-1}) \\ & + \frac{L_g \omega_r^2 \beta_2}{2} \sum_{s=1}^{N/2-1} (Q_{2s} Q_{2s+1} + Q_{2s+1} Q_{2s}). \end{aligned} \quad (\text{A10})$$

This Hamiltonian is quantized by introducing the quantized charge, Q_s , and flux, φ_s , operators, acting on site s , satisfying the commutation relation,

$$[\varphi_s, Q_{s'}] = i \delta_{s,s'}. \quad (\text{A11})$$

They are defined as,

$$Q_s = \sqrt{\frac{1}{2Z_r}} (a_s - a_s^\dagger), \quad (\text{A12})$$

$$\varphi_n = \sqrt{\frac{Z_r}{2}} (a_s + a_s^\dagger), \quad (\text{A13})$$

where a_s^\dagger (a_s) is the annihilation (creation) operator on the n -th site.

Inserting Eq. (A12) and Eq. (A13) into Eq. (A10), we find the dimerized Hamiltonian,

$$\begin{aligned} H_{CCA} = & \omega_r \sum_{s=1}^N a_s^\dagger a_s \\ & + J_1 \underbrace{\sum_{s=1}^{N/2} (a_{2s-1}^\dagger a_{2s} + \text{H. c.})}_{\text{Intracell coupling}} \\ & + J_2 \underbrace{\sum_{n=1}^{N/2-1} (a_{2s}^\dagger a_{2s+1} + \text{H. c.})}_{\text{Intercell coupling}}. \end{aligned} \quad (\text{A14})$$

In our setup, we observe a non-negligible contribution from higher-order neighbor coupling terms. Following Ref. [28], we identify two main origins for these terms. First, as discussed in the introduction of the capacitance matrix, when the ratio $C_{1(2)}/C_\Sigma \ll 0.1$, higher-order couplings naturally emerge upon inverting the capacitance matrix. Second, direct stray capacitances can mediate coupling between non-adjacent (next-nearest and beyond) resonators. These higher-order neighbor couplings, up to order $q = 4$, can be written as

$$K' = \sum_{q=2}^4 \sum_{s=1}^{N-q} J^{(q)} (a_s^\dagger a_{s+q} + \text{h.c.}), \quad (\text{A15})$$

where $J^{(q)}/2\pi$ denotes the coupling strength to the q -th neighbor. In particular, the couplings to the second, third, fourth, and fifth neighbors are denoted J' , J'' , J''' , and J'''' , respectively. The extraction of the Hamiltonian parameters is reported in [Supplementary Note B](#) and their values are reported in [Ext. Data Tab. 1](#).

2. Transmon + Metamaterial

In this subsection, we add the split-junction transmon qubit [77] to the system. As we did in subsection A 1, we can derive the Lagrangian of the full circuit to then obtain the full Hamiltonian of the system. The Lagrangian of the full circuit takes the form [27],

$$\mathcal{L}_{Tot} = \frac{1}{2} (\dot{\varphi}^T [C_{Tot}] \dot{\varphi}) - V. \quad (\text{A16})$$

The total capacitance matrix is defined as,

$$[C_{Tot}] = \begin{pmatrix} [C] & -[C_c] \\ -[C_c]^T & C_T \end{pmatrix}, \quad (\text{A17})$$

$[C_c]$ is of dimension $(1, 44)$ and represent the coupling capacitances between the transmon qubit and the metamaterial. C_T is the total capacitance of the transmon qubit and is defined as $C_T = C_{T,g} + \sum_s C_{c,s}$, with $C_{T,g}$ the transmon capacitance to ground and $C_{c,s}$ the coupling capacitance to site s . The potential energy V is defined as,

$$V = \frac{1}{2L_g} \sum_{s=1}^N \varphi_s^2 - E_J(\varphi). \quad (\text{A18})$$

$E_J(\varphi) = E_J \cos(\Phi/\Phi_0)$ is the Josephson Energy, Φ is the flux threaded through the SQUID of transmon and $\Phi_0 = h/2e$ is the flux quantum. Applying the Legendre transformation $H = 1/2 \mathbf{Q}^T [C]^{-1} \mathbf{Q} + V$ [27], and applying quantization as done in the previous section one gets the Hamiltonian,

$$\begin{aligned} H = & \omega_r \sum_{s=1}^N a_s^\dagger a_s + J_1 \sum_{s=1}^{N/2} (a_{2s-1}^\dagger a_{2s} + \text{H. c.}) \\ & + J_2 \sum_{s=1}^{N/2-1} (a_{2s}^\dagger a_{2s+1} + \text{H. c.}) \\ & + \sum_{q=2}^4 \sum_{s=1}^{N-q} J_{s,s+q} (a_s^\dagger a_{s+q} + \text{H. c.}) \\ & + \omega_q b^\dagger b - \frac{E_C}{2} b^\dagger b^\dagger b b + \sum_{s=1}^N g_s (a_s^\dagger b + \text{H. c.}), \end{aligned} \quad (\text{A19})$$

where $\omega_q \approx \sqrt{8E_C E_J(\Phi)} - E_C$ and $g_s/2\pi$ is the qubit site coupling rate.

Supplementary Information B: Metamaterial characterization

1. Extraction of the Hamiltonian parameters

The circuit parameters of the CCA are extracted by measuring the CCA in transmission via single-tone spectroscopy at high photon number, with the qubit detuned to its lowest frequency (see [Fig. 12a](#)). From this measurement, two distinct bands are observed, each containing 21 modes. The two modes located in the middle bandgap are identified as the SSH modes. These modes exhibit low amplitudes in transmission due to the minimal overlap of their photonic wavefunctions, which is a consequence of the CCA's effective size. Additionally, these modes are non-degenerate due to the presence of disorder that breaks chiral symmetry [28].

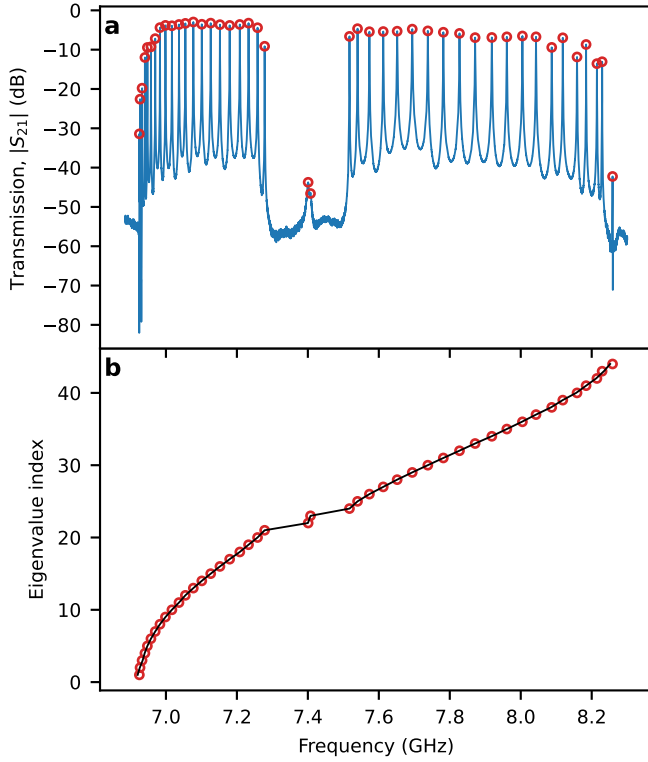


Figure 12. **CCA characterization: Hamiltonian.** (a) Single-tone spectroscopy measurement of the CCA at high photon number with the qubit detuned. The extracted eigenmodes are represented with the red circles. (b) Eigenmodes of the CCA as a function of the eigenvalue index (red circle). The black line represent the fit of the eigenmodes of the CCA.

A peak-finding algorithm detects the 44 eigenmodes of the CCA, which are shown in Fig. 12b. The detected mode frequencies are fitted to the eigenvalues of the Hamiltonian in Eq. (A7), with the fit indicated by a black line in Fig. 12b. The extracted parameters from this fit are listed in Ext. Data Tab. 1.

A strong asymmetry between the lower and upper bands of the CCA spectrum is observed. This asymmetry is caused by higher-than-first-neighbor couplings between CCA sites. These couplings arise from stray capacitance between higher-neighbor sites and from the high coupling ratio $C_{1(2)}/C_\Sigma$, which introduces additional coupling terms during the inversion of the capacitance matrix (Eq. (A5)).

2. Extraction of the metamaterial dissipation

This subsection focuses on extracting the dissipations of the bare CCA, following the extraction of circuit parameters in the previous subsection.

To extract the bare dissipation rates of the eigenmodes, we first detune the qubit to its lowest frequency. Each resonance is then measured via single-tone spectroscopy as a function of the VNA input power, performing re-

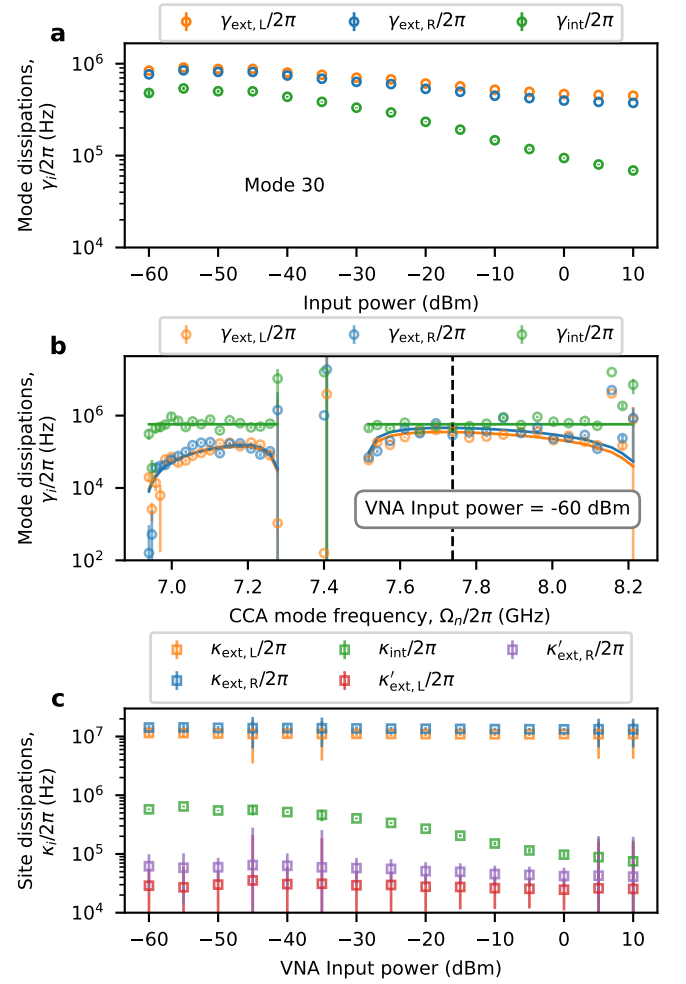


Figure 13. **CCA characterization: Dissipations.** (a) Mode dissipations, γ , vs VNA input power for mode 30 of the CCA. The reported dissipation are the external dissipation to the left port (orange), right port (blue) and internal dissipations (green). (b) Fit of the mode dissipations, γ , with the complex part of the eigenvalues of the non-Hermitian Hamiltonian Eq. (B3). The fitted mode in panel a is highlighted by the black dashed line. (c) Extracted site dissipations, κ , vs VNA input power from the fit in panel b.

flection measurements from both sides of the CCA. The reflection scattering coefficients on the left and right port for mode m are defined as,

$$S_{LL}^{(m)} = A_L e^{-i\alpha_L} \left(1 - \frac{\gamma_{\text{ext},L} e^{i\phi_L}}{i(\omega_p - \tilde{\omega}_m) + \frac{\gamma_{\text{ext},L} + \gamma_{\text{ext},R} + \gamma_{\text{int}}}{2}} \right), \quad (\text{B1})$$

and,

$$S_{RR}^{(m)} = A_R e^{-i\alpha_R} \left(1 - \frac{\gamma_{\text{ext},R} e^{i\phi_R}}{i(\omega_p - \tilde{\omega}_m) + \frac{\gamma_{\text{ext},L} + \gamma_{\text{ext},R} + \gamma_{\text{int}}}{2}} \right), \quad (\text{B2})$$

respectively, where the dissipation rates to the left ($\gamma_{\text{ext},L}$) and right ($\gamma_{\text{ext},R}$) ports are not assumed to be

symmetric. The parameter $\gamma_{\text{int}}/2\pi$ represents the internal dissipation rate of the cavity. The parameters $A_{L(R)}$, $\alpha_{L(R)}$, and $\phi_{L(R)}$ represent the baseline amplitude, phase shift, and impedance mismatch, respectively, of the scattering trace measured from the left (right) port. Phase delays are corrected during post-processing. The mode's resonant frequency is given by $\tilde{\omega}_m/2\pi$ and the probe frequency by $\omega/2\pi$. Each mode is fitted in the complex plane using Eq. (B1) and Eq. (B2). Typical fitting results for mode 30 are shown in Fig. 13a.

The procedure above is repeated for all eigenmodes, with results shown in Fig. 13b for a VNA input power of -60 dBm. These dissipations can be modeled by transforming the Hamiltonian in Eq. (A7) into a non-Hermitian Hamiltonian that accounts for dissipation effects:

$$H_{\text{CCA};k,l}^{\text{Non-Herm}} = H_{\text{CCA};k,l} - i\mathbf{I} \frac{\kappa_{\text{int}}}{2} - \frac{i}{2} \begin{cases} \kappa_{\text{ext},L} & \text{if } k = l = 0, \\ \kappa_{\text{ext},R} & \text{if } k = l = 44, \\ \kappa'_{\text{ext},L} & \text{if } k = l = 1, \\ \kappa'_{\text{ext},R} & \text{if } k = l = 43, \\ 2\sqrt{\kappa_{\text{ext},L}\kappa'_{\text{ext},L}} & \text{if } (k, l) = (0, 1) \\ & \text{or } (1, 0), \\ 2\sqrt{\kappa_{\text{ext},R}\kappa'_{\text{ext},R}} & \text{if } (k, l) = (44, 43) \\ & \text{or } (43, 44). \end{cases} \quad (\text{B3})$$

where the dissipation parameters are defined as:

- $\kappa_{\text{int}}/2\pi$: Internal cavity dissipation rate (assumed equal for all cavities)
- $\kappa_{\text{ext},L}/2\pi$ and $\kappa_{\text{ext},R}/2\pi$: External coupling rates of the leftmost and rightmost cavities to their respective measurement ports
- $\kappa'_{\text{ext},L}/2\pi$ and $\kappa'_{\text{ext},R}/2\pi$: External coupling rates of the second-to-leftmost and second-to-rightmost cavities to their respective measurement ports

The imaginary part of the eigenvalues of Eq. (B3) determines the dissipation profile of the eigenmodes through the relation:

$$\text{Im}(\text{Eig}(H_{\text{CCA}}^{\text{Non-Herm}})) = 2\vec{\gamma}_{\text{Tot}}, \quad (\text{B4})$$

where $\vec{\gamma}_{\text{Tot}} = \vec{\gamma}_{\text{int}} + \vec{\gamma}_{\text{ext},L} + \vec{\gamma}_{\text{ext},R}$ represents the total dissipation rate vector of length $N = 44$ for all eigenmodes.

By selectively setting dissipation values to zero in the non-Hermitian Hamiltonian (Eq. (B3)), we can isolate and extract the different dissipation contributions of the

CCA. Specifically:

$$\text{Im}(\text{Eig}(H_{\text{CCA}}^{\text{Non-Herm}})) = 2 \begin{cases} \vec{\gamma}_{\text{int}} & \text{if } \kappa_{\text{ext},R} = \kappa_{\text{ext},L} = \kappa'_{\text{ext},R} = \kappa'_{\text{ext},L} = 0, \\ \vec{\gamma}_{\text{ext},R} & \text{if } \kappa_{\text{ext},L} = \kappa'_{\text{ext},L} = \kappa_{\text{int}} = 0, \\ \vec{\gamma}_{\text{ext},L} & \text{if } \kappa_{\text{ext},R} = \kappa'_{\text{ext},R} = \kappa_{\text{int}} = 0. \end{cases} \quad (\text{B5})$$

The internal and external dissipations extracted using Eq. (B1) and Eq. (B2) are fitted to Eq. (B5), with results shown in Fig. 13b for a VNA input power of -60 dBm. As shown in the figure, we observe the expected behavior: external dissipation is larger in the center of the band compared to the edges, and there is a strong asymmetry in external dissipation between the lower and upper bands. This asymmetry arises from next-nearest-neighbor interactions and the $\kappa'_{\text{ext},L(R)}$ terms.

The extraction procedure is repeated for multiple input powers, with results shown in Fig. 13c. The complete set of extracted dissipation parameters at low power (-60dB VNA input power) is reported in Ext. Data Tab. 1. With these results, combined with the previously extracted CCA circuit parameters, we now have complete characterization of both the real and imaginary parts of the non-Hermitian Hamiltonian (Eq. (B4)) in the single-excitation subspace.

3. Influence of disorder on the dissipations

Disorder affects mode localization, whether originating from resonant frequency disorder or coupling disorder, which in turn affects the external dissipation rates $\gamma_{\text{ext},L(R)}/2\pi$. This effect is particularly evident in the measurements presented in section V and section VI. To quantitatively study this phenomenon, we perform simulations of the expected dissipations for different CCA modes using Eq. (B5) over 50,000 realizations of resonant frequency disorder (Fig. 14). These simulations highlight the way disorder alters the dissipation profile.

A typical disorder realization is shown in Fig. 14, where green, blue, and orange circles correspond to γ_{int} , $\gamma_{\text{ext},L}$, and $\gamma_{\text{ext},R}$, respectively. Internal dissipation rates are unaffected by frequency disorder since we assume constant losses across all sites, an idealization that differs from experimental conditions. Notably, disorder impacts the lower band more significantly than the upper band, due to the lower dispersion, and thus lower kinetic energy, in this band.

Supplementary Information C: Qubit characterization

In this section the characterization of the qubit is presented.

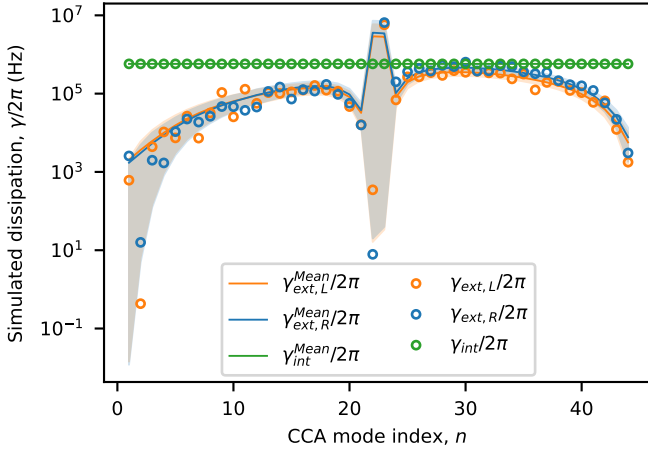


Figure 14. **Simulation of the CCA mode dissipation, γ , with disorder.** Dissipations simulated with the eigenvalues of the non-Hermitian Hamiltonian Eq. (B5) with a standard deviation on the resonant frequency of 22 MHz, repeated 5×10^4 times. The orange (blue) line is the mean external dissipation rates from the left $\gamma_{\text{ext},L}^{\text{Mean}}/2\pi$ (right $\gamma_{\text{ext},R}^{\text{Mean}}/2\pi$) as a function of the CCA mode index. The green line is the mean internal dissipation rate $\gamma_{\text{int}}^{\text{Mean}}/2\pi$ as a function of the CCA mode index. The orange, blue and green shaded areas encompass the 18.57-th and the 84.13-th percentile of the dissipation distribution associated to $\gamma_{\text{ext},L}/2\pi$, $\gamma_{\text{ext},R}/2\pi$ and $\gamma_{\text{int}}/2\pi$, respectively. The orange, blue and green circles corresponds to a single disorder realization associated to $\gamma_{\text{ext},L}/2\pi$, $\gamma_{\text{ext},R}/2\pi$ and $\gamma_{\text{int}}/2\pi$, respectively.

1. Two-tone spectroscopy measurements

The transmon qubit is characterized using pulsed two-tone spectroscopy at frequencies in the upper, middle, and lower bandgaps. The measurement protocol consists of applying a fast flux pulse to the qubit via the flux line, followed by a 200 ns π -pulse through the charge line. After resetting the flux bias to its initial value, we perform readout.

The transmon qubit's sweet spot is located in the upper bandgap [see Fig. 15a]. We find a good agreement between the theoretical model predictions (red dashed lines) and the experimental measurements shown in Fig. 15. A strong frequency shift between the bare qubit and the dressed qubit remains evident in the middle bandgap and the lower bandgap. This is attributed to the strong coupling to the upper band edge modes.

The transmon qubit's sweet spot is located in the upper bandgap [see Fig. 15a]. We find good agreement between the predictions of the theoretical model (red dashed lines) and the experimental measurements shown in Fig. 15. A pronounced frequency shift between the bare and dressed qubit remains visible in both the middle and lower bandgaps, which we attribute to the strong coupling to the upper band-edge modes.

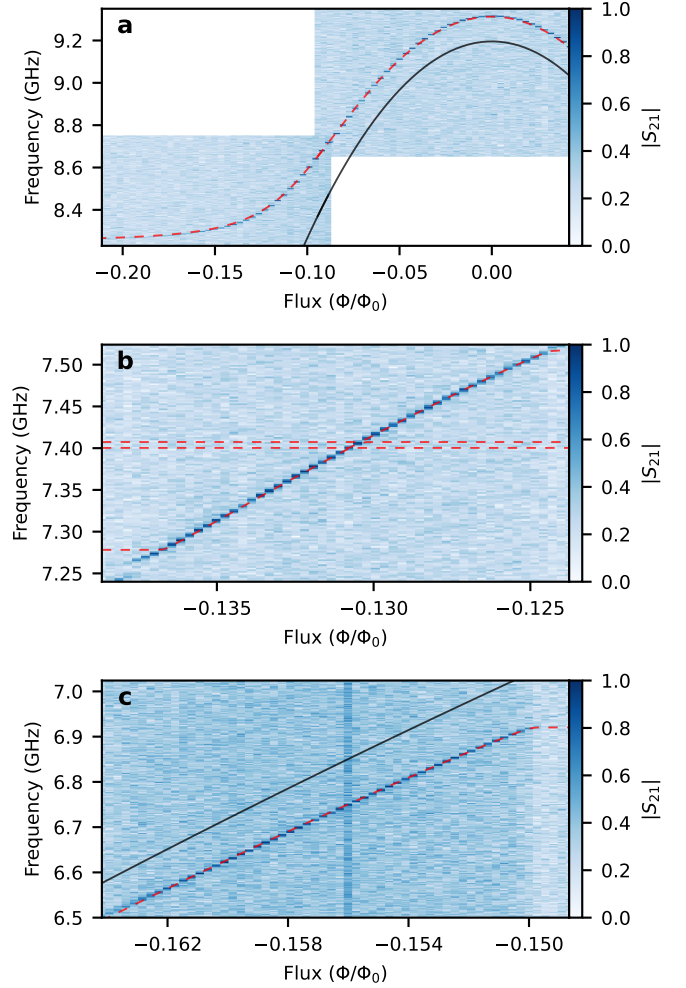


Figure 15. **Two-tone spectroscopy measurement.** (a) Two-tone spectroscopy measurement of the transmon qubit above the upper band as a function of the reduced flux, Φ/Φ_0 , threading the SQUID loop. With the qubit initialized at $\omega_q/2\pi = 9.05$ GHz and $\omega_q/2\pi = 8.46$ GHz. The red-dashed line is the theoretical prediction. The black line is the bare qubit frequency ($\omega_q/2\pi$) (b) Same as in panel a in the middle bandgap. With the qubit initialized at $\omega_q/2\pi = 7.52$ GHz. (c) Same as in panel a and b below the lower band. With the qubit initialized at $\omega_q/2\pi = 6.80$ GHz.

2. Losses

In this subsection, we evaluate the Purcell losses experienced by the qubit to identify the factors limiting its lifetime. The first source of loss we consider is the drive line. The Purcell decay rate due to the drive line is given by:

$$\gamma_{\text{Purcell-Drive}} = \omega_q^2 Z_0 \frac{C_c^2}{C_\Sigma}, \quad (\text{C1})$$

where $C_c = 0.5$ fF is the coupling capacitance between the drive line and the qubit, estimated from finite element simulations, $C_\Sigma = 60.9$ fF is the total capacitance of the

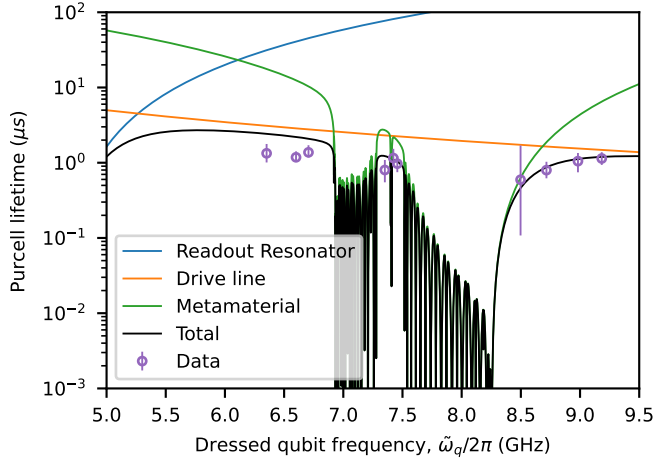


Figure 16. **Purcell lifetime.** Limit of the qubit lifetime due to the environment as a function of the dressed qubit frequency, $\tilde{\omega}_q/2\pi$. The blue line is the contribution from the readout resonator. The orange line is the contribution from the drive line. The green line is the contribution from the CCA. The black line is the sum of the contributions. The data are represented with the purple circle. The errorbar corresponds to the minimum and maximum fitted qubit lifetime.

transmon qubit, and Z_0 is the characteristic impedance of the drive line. Given the high ratio $C_c/C_\Sigma = 0.008$, this Purcell decay mechanism limits the qubit lifetime to 5 μs at 5 GHz, decreasing to less than 2 μs at 9.5 GHz [orange line in Fig. 16].

A second source of Purcell decay is due to the readout resonator,

$$\gamma_{\text{Purcell-Res}} = (\gamma_{\text{RO,ext}} + \gamma_{\text{RO,int}}) \left(\frac{g}{\Delta} \right)^2. \quad (\text{C2})$$

$\gamma_{\text{RO,ext}}/2\pi = 1.64 \text{ MHz}$ is the external coupling of the readout resonator to its feedline, $\gamma_{\text{RO,int}}/2\pi = 330 \text{ kHz}$, is the intrinsic dissipation rate of the readout resonator, $g/2\pi = 89 \text{ MHz}$ is the coupling rate of the qubit to the readout resonator, and $\Delta = \omega_q - \omega_{\text{RO}}$, is the detuning between the qubit and the readout resonator of resonant frequency $\omega_{\text{RO}}/2\pi = 4.6 \text{ GHz}$. This source of losses is limiting the qubit lifetime to values greater than 10 μs in the measurement range [blue line in Fig. 16].

The third source of losses is the Purcell decay due to the CCA,

$$\gamma_{\text{Purcell-CCA}} = \sum_{n=1}^{44} (\gamma_{n,\text{int}} + \gamma_{n,\text{ext}}) \left(\frac{G_n}{\Delta_n} \right)^2 \quad (\text{C3})$$

$\gamma_{n,\text{ext}}/2\pi$ is the external dissipation rate mode n , $\gamma_{n,\text{int}}/2\pi$ is the internal dissipation rate of mode n . $G_n/2\pi$ is the coupling rate from the qubit to mode n and $\Delta_n = (\Omega_n - \omega_q)$ is the detuning between mode n and the qubit. This source of losses is limiting the qubit lifetime to 10 μs below the lower band, around 2-3 μs in the middle bandgap and between 1 and 10 μs in the upper bandgap [green line in Fig. 16].

The combined Purcell effect is represented by the black line in Fig. 16. We compare experimental qubit lifetime measurements at different frequencies [purple circles in Fig. 16] against the predicted Purcell decay rates. Each qubit decay rate measurement is repeated 100 to 2000 times per frequency point over a duration of several hours to ensure statistical reliability. In the upper bandgap, we observe excellent agreement between experimental lifetimes and Purcell decay predictions. Here, the lifetime is limited by the CCA when the qubit is near the band edge and by the drive line when the qubit is far detuned from the band. In the middle bandgap, the experimental data show reasonable agreement with theory, where the qubit lifetime is limited by both the drive line and the CCA. In the lower bandgap, the qubit lifetime is slightly below the predictions based solely on Purcell decay, suggesting the presence of additional loss mechanisms in this frequency range.

3. Calibration π -pulse

For the measurements presented in section IV and section VI, the qubit π -pulse was calibrated according to the sequence shown in Fig. 17. Below we briefly describe each parameter extracted at each steps of the calibration sequence. The pulse sequences are shown on top of each panels of Fig. 17.

1. **Two-tone spectroscopy measurement:** The 01 transition of the qubit is first estimated [red dashed line in Fig. 17a] by performing two-tone spectroscopy.
2. **Time-Rabi:** The π -pulse time is then estimated [red dashed line in Fig. 17b] by doing time-Rabi measurement with a square pulse shape.
3. **Ramsey vs detuning:** The precise qubit frequency is extracted [red dashed line in Fig. 17c] by performing a Ramsey measurement as a function of excitation pulse detuning with a square pulse shape.
4. **Power Rabi:** Then the time of the pulse is fixed to 40 ns and a Power Rabi measurement is done to estimate the optimal π -pulse amplitude [red dashed line in Fig. 17d] with a gaussian pulse shape.
5. **Gauss error amplification:** To refine the π -pulse amplitude estimate, we perform Gaussian error amplification by applying a train of $2N + 1$ π -pulses as a function of pulse amplitude. The optimal amplitude is determined by fitting the resulting pattern [red dashed line in Fig. 17e].
6. **DRAG error amplification:** We use DRAG to prevent leakage to higher excited state [78]. The DRAG amplitude is calibrated by performing a similar type of measurement as done above, but

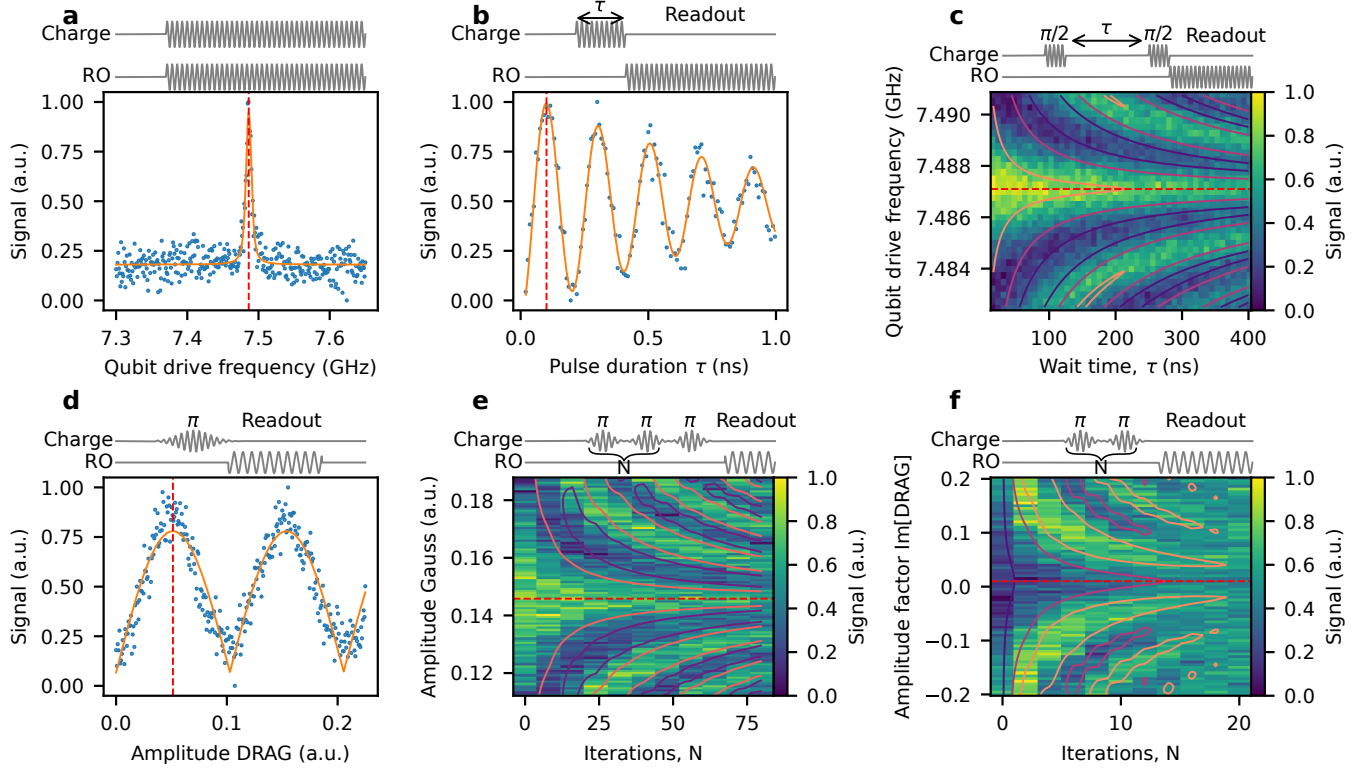


Figure 17. π -pulse calibration sequence. In all panels the pulse sequence is indicated above and the measurement shown below. **(a)** Two-tone spectroscopy measurement. The data points are indicated with blue dots, the fit is indicated with the orange line. The red dashed line represents the extracted qubit frequency. **(b)** Time-Rabi measurement with the qubit driven at the frequency extracted in the previous measurement. The data points are indicated with blue dots, the fit is indicated with the orange line. The red dashed line represents the pulse time required to perform a π -pulse. **(c)** Ramsey measurement vs qubit frequency drive. The $\pi/2$ pulse is calibrated from the previous measurement. The data is represented in the colormap and the fit is shown with the contour plot. The red dashed line shows the extracted qubit frequency. **(d)** Power Rabi measurement. The measurement is performed at the frequency of the qubit extracted from the previous measurement. The data points are indicated with blue dots, the fit is indicated with the orange line. The red dashed line shows the amplitude required to perform a π -pulse. **(e)** Gauss error amplification measurement. The data is represented in the colormap and the fit is shown with the contour plot. The red dashed line shows the optimal amplitude for the π -pulse. **(f)** DRAG error amplification measurement. The data is represented in the colormap and the fit is shown with the contour plot. The red dashed line shows the optimal amplitude factor on the DRAG asymmetry parameter.

sweeping the imaginary component of DRAG pulse. The extracted parameter is shown with the red dashed line in Fig. 17f.

Supplementary Information D: Qubit + metamaterial characterization

1. More data figure 2

In Fig. 18, we report zoom ins of the single-tone spectroscopy measurement presented in Fig. 2.

2. More atomic ratios

In Fig. 19, we present supplementary atomic ratio measurements performed via single-tone spectroscopy in the lower band [panel Fig. 19a] and upper band [panel Fig. 19b], and via two-tone spectroscopy in the bandgaps [panel Fig. 19c]. These measurements are done using the method introduced in the main text.

Supplementary Information E: Open dynamics of the qubit

1. Qubit initialized in the middle bandgap

In the time domain measurements shown in section IV, the qubit is initialized in the middle bandgap. Its fre-

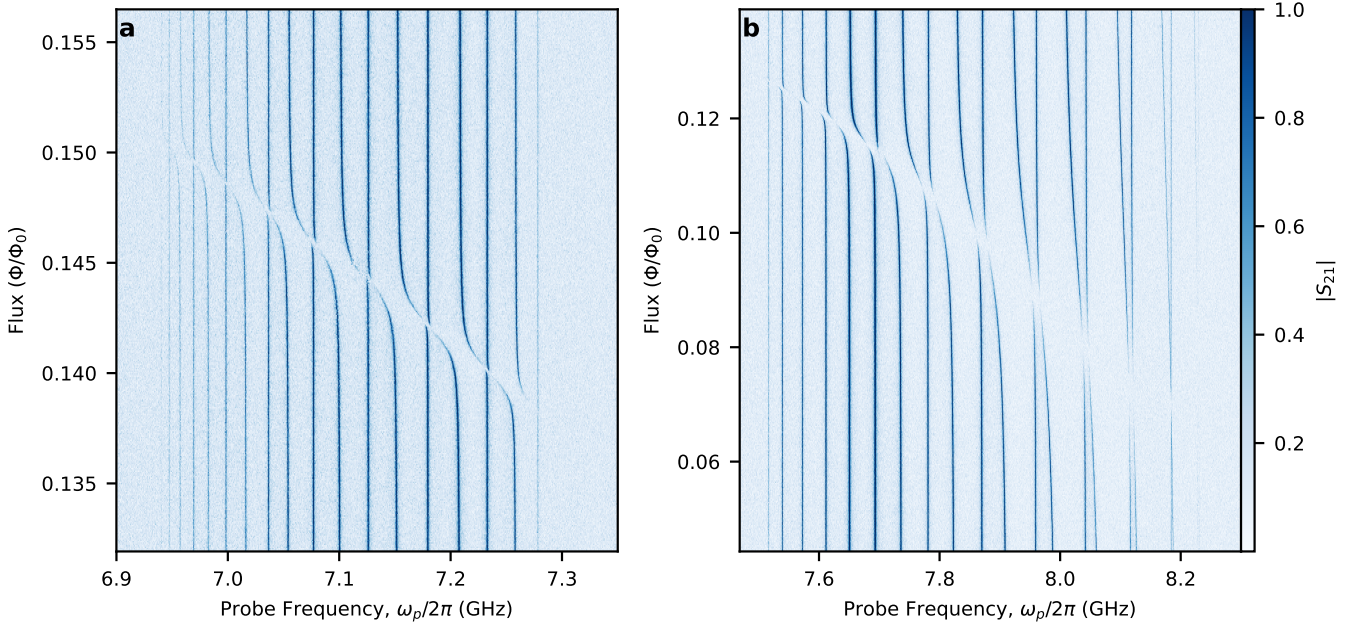


Figure 18. **Zoom-in on the spectroscopy measurements in figure 2.** Single-tone spectroscopy measurements vs reduced flux Φ/Φ_0 , in the lower band (a) and the upper band (b). The color bar is shared between the two panels.

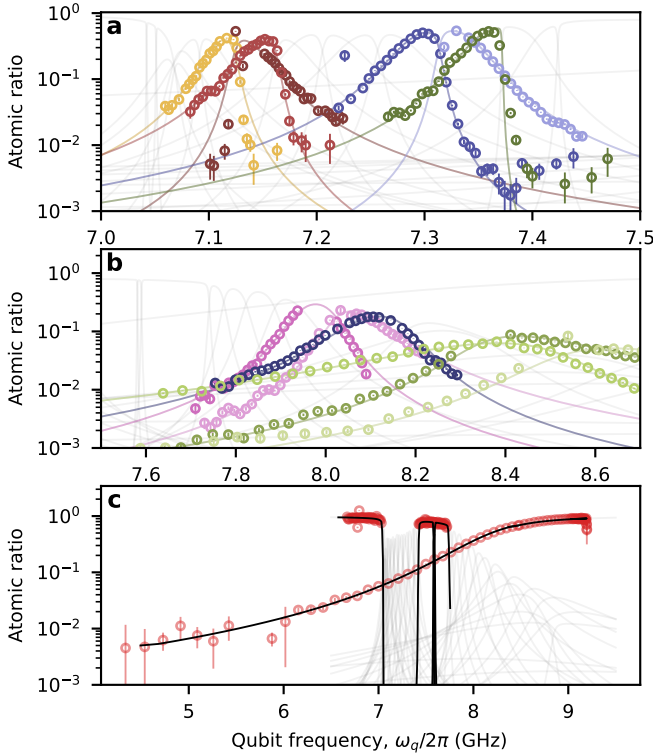


Figure 19. **More atomic ratio.** (a) Atomic ratio in the lower band of modes 9, 10, 11, 17, 18 and 19. Modes 13 and 14 are in the main text. (b) Atomic ratio in the upper band of modes 29, 30, 31, 34, 35 and 36. Modes 31 and 32 are also reported in the main text. (c) Atomic ratio measured with two-tone spectroscopy. Modes 1, 21, 22, 23 and 45.

quency is then rapidly tuned to a target value, allowing it to interact with the CCA for a defined duration, before returning to the initial frequency for state measurement. Four distinct frequency regions are identified in [Figure 3](#):

- the lower bandgap ($\omega_q/2\pi \lesssim 7.015$ GHz),
- the lower band ($7.015 \text{ GHz} \lesssim \omega_q/2\pi \lesssim 7.43$ GHz),
- the middle bandgap ($7.43 \text{ GHz} \lesssim \omega_q/2\pi \lesssim 7.725$ GHz), and
- the upper band ($\omega_q/2\pi \gtrsim 7.725$ GHz).

However, we do not resolve the upper bandgap due to the strong coupling between the qubit and the last CCA mode.

In [Fig. 20](#), we compare the measured dynamics of the qubit to the simulated dynamics of the qubit using `QuantumToolbox.jl` [see [Methods](#)]. First, we simulate the experimental pulse sequence, where the ramp time is limited to 2.4 ns, the simulation is reported in [Fig. 20c–d](#). We find excellent agreements between theory and experiment, where the upper bandgap is also not resolvable in the simulation. Notable differences happens in terms of losses, where in the bandgaps we find enhance losses most likely due to Two-Level-System fluctuators, however we cannot certainly assess this conclusion.

In [Fig. 20](#), we compare the measured dynamics of the qubit to simulations performed using `QuantumToolbox.jl` [see [Methods](#)]. Our simulations model the experimental pulse sequence where the ramp time of the flux offset is fixed to 2.4 ns, and the results are presented in [Fig. 20c–d](#). We find excellent agreement between theory and experiment, including the inability

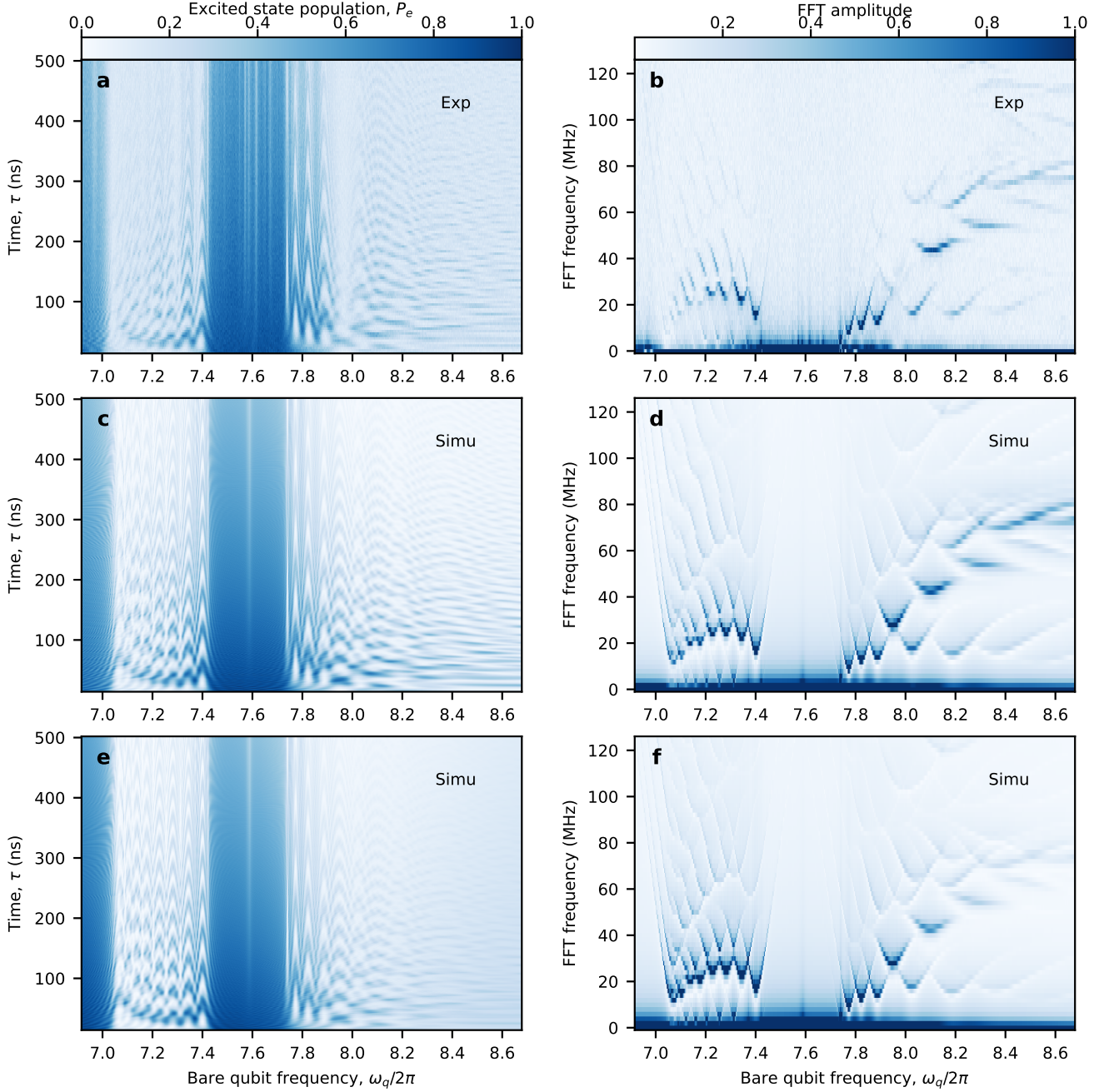


Figure 20. **Comparing the dynamics of the emitter in the bath with theory.** (a) Measurement of the excited state population of the qubit as a function of the time τ and the bare qubit frequency $\omega_q/2\pi$ with a ramp time of 2.4 ns. The measurement is done according to the pulse sequence indicated in Fig. 3. (b) Fourier transform of the data in panel a. The colormap is saturated to better highlight the features. (c) Simulation of the time evolution of the qubit as a function of the time τ and the bare qubit frequency $\omega_q/2\pi$ with a ramp time of 2.4 ns. (d) Fourier transform of the simulated data in panel c. The colormap is saturated to better highlight the features. (e) Simulation of the time evolution of the qubit as a function of the time τ and the bare qubit frequency $\omega_q/2\pi$ with a ramp time of 0.1 ns. (f) Fourier transform of the simulated data in panel e. The colormap is saturated to better highlight the features.

to resolve the upper bandgap. We observe notable differences in the bandgaps, where the measurement shows enhanced losses that we attribute to two-level system (TLS) fluctuators, although we cannot definitively confirm this

explanation.

In Fig. 20e–f, we simulate the qubit dynamics with a ramp time of 0.1 ns. In this case, we can resolve the upper bandgap, unlike with the ramp time of 2.4 ns. However,

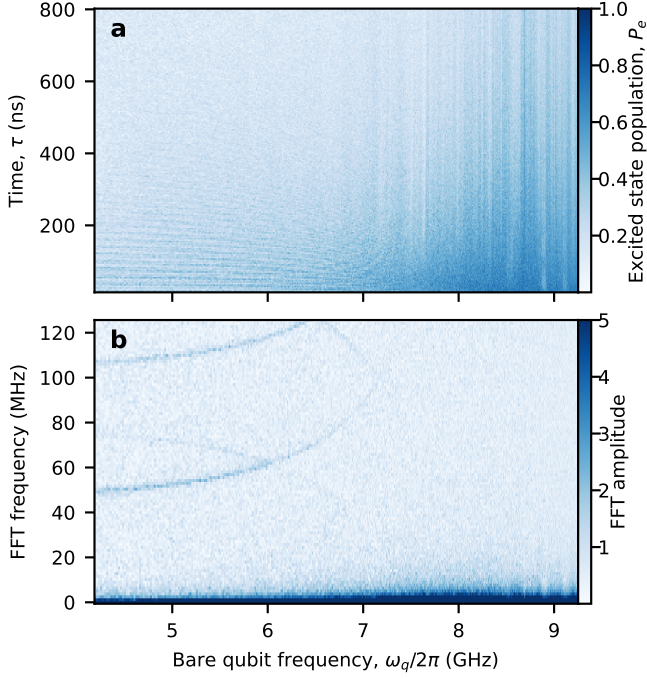


Figure 21. **Qubit dynamics with the qubit initialized in the upper bandgap.** (a) Measurement of the excited state population of the qubit as a function of the time τ and the bare qubit frequency $\omega_q/2\pi$. The qubit is initialized in the upper bandgap. (b) Fourier transform of the experimental data in panel a. The colormap is saturated to highlight its features.

we observe fewer mode interactions than in Fig. 20c–d in the upper bandgap, which we attribute to population transfer to atom photon bound state above the upper band.

2. Qubit initialized in the upper bandgap

In this subsection, we initialize the qubit in the upper bandgap at $\omega_q/2\pi = 8.69$ GHz and repeat the same measurement protocol as in the previous subsection. The time domain measurements are shown in Fig. 21a and the corresponding Fast Fourier transform is presented in Fig. 21b. We observe a standard exponential decay for frequencies $\omega_q/2\pi \gtrsim 7.3$ GHz. We observe fewer Rabi oscillations than in Fig. 3c, which we attribute to strong coupling between the qubit and the upper band that prevents leakage into CCA modes. This strong coupling can be exploited to implement fast gates on APBS without dynamical hybridization with the band.

Supplementary Information F: Calibration SWAP

This section outlines the typical routine for calibrating the SWAP gate.

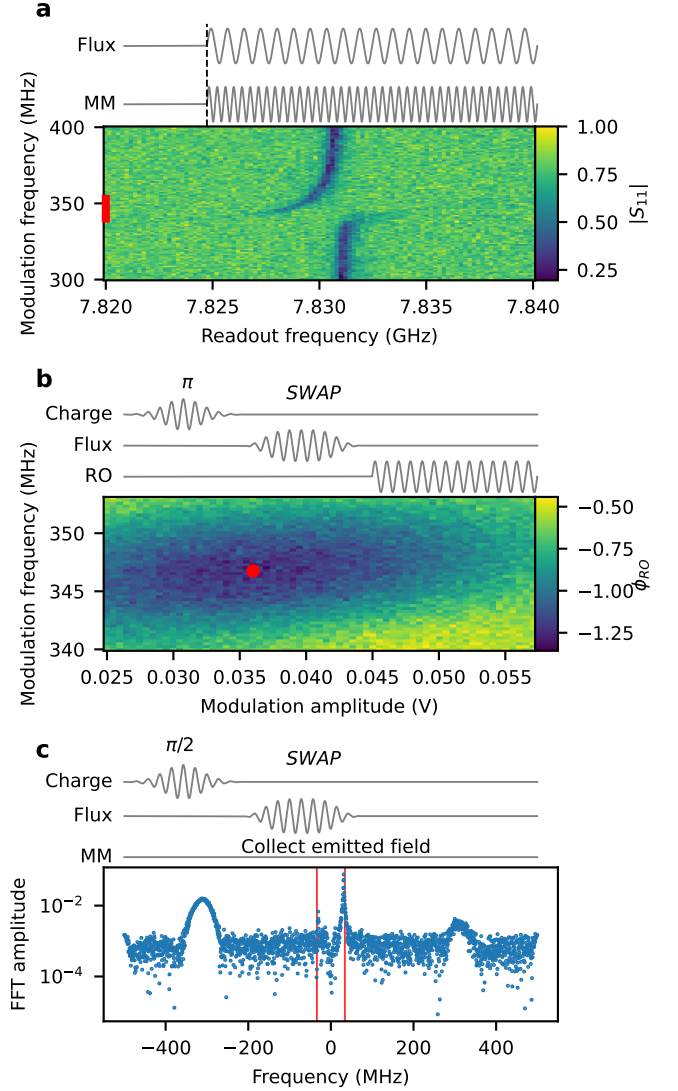


Figure 22. **Calibration SWAP** (a) Metamaterial spectroscopy vs qubit modulation frequency. The vertical red line highlight the frequency range chosen for the next measurement. (b) Evolution of the qubit population as a function of the modulation frequency and amplitude for a fixed modulation length of 120ns. The red point highlight the optimal modulation frequency and amplitude chosen for the emission measurement. (c) Emitted field after calibrating the SWAP pulse. The red dashed lines are the frequency at which we expect the field to be emitted.

The initial step involves obtaining an estimate of the modulation frequency and amplitude required to perform the SWAP. This is achieved by applying a flux modulation tone to the qubit and measuring the CCA mode of interest at low power, as shown in Fig. 22a.

The subsequent step focuses on precisely estimating the SWAP amplitude, duration, and frequency. The SWAP duration is fixed at 160ns to limit the amplitude of the SWAP gate, in order to avoid coupling to

other CCA modes. Typically, such measurements are performed similarly to those in Fig. 17e. However, due to the high dissipation rate of the eigenmodes, this method proves impractical in our case. Instead, the calibration step involves exciting the qubit, applying the frequency modulation as a function of amplitude and modulation frequency for a fixed duration, and then measuring the qubit population to minimize its value. The results of these measurements are presented in Fig. 22b. The global minima of this 2D map are determined using a total variation denoising algorithm, which identifies the optimal modulation amplitude and frequency for the fixed SWAP duration set during calibration.

The final step assesses whether neighboring eigenmodes are populated during the SWAP. To this end, an emission experiment is conducted. The qubit is first excited to a superposition state via a $\pi/2$ -pulse, and its population is then transferred to the eigenmode of interest using the calibrated SWAP pulse. The emitted field from the CCA is collected throughout the entire pulse sequence and subsequent decay, and is downconverted using a local oscillator at 7.8 GHz. A fast Fourier transform is applied to the complex signal to identify the modes contributing to the emitted field, as illustrated in Fig. 22c. The frequency range of this diagram spans from -500 MHz to +500 MHz. At approximately ± 30 MHz, the expected emission frequency is observed. At around ± 300 MHz, a wide peak is detected, which is attributed to cross-talk from the charge line due to the $\pi/2$ -pulse [further details in [Supplementary Note H](#)].

Supplementary Information G: Calibration of Attenuation and Gain for the emission measurement

For the measurements presented in section VI, a precise knowledge of the gain was needed. In this section, we describe the calibration sequence to extract the gain, focusing on modes 31 and 32 studied in section VI. In order to extract the gain, we first need to calibrate for the attenuation, for this we use a typical AC-stark shift measurement. We assume a dispersive Hamiltonian of the type,

$$H_{\chi, \text{Mode}}^{(m)} = \omega_q \frac{\sigma_z}{2} + \tilde{\omega}_m (a_m^\dagger a_m + \chi_m \sigma_z), \quad (\text{G1})$$

with σ_z , the Pauli Z operator, $\tilde{\omega}_m/2\pi$ the frequency of mode m and χ_m the dispersive shift associated to mode m . Due to the complexity of the system, we do not analytically estimate χ_m using the qubit coupling to the mode and detuning. Indeed, we expect the dispersive shift to be also proportional to the atomic ratio of the eigenmode. It will only be valid for a specific flux value, hence, for all the measurements described below we are going to work at a fixed flux value with the dressed qubit frequency $\tilde{\omega}_q/2\pi = 7.38$ GHz, corresponding to the bare qubit frequency $\omega_q/2\pi = 7.55$ GHz.

1. Dispersive shift measurement

The first step consists of extracting the dispersive shift for both eigenmodes. To do so, we measure the mode of interest with the qubit in its ground and excited state [Fig. 23a–b]. From this measurement, we expect to observe the modes to shift in frequency by 2χ . For mode 31, we observe a large dispersive shift, $\chi_{31}/2\pi = -498 \pm 12$ kHz, due to the large qubit coupling to this eigenmode. However, for mode 32, the dispersive shift is weak, $\chi_{32}/2\pi = -91 \pm 29$ kHz, due to the weak coupling qubit to this eigenmode, this is due to the specific coupling configuration of the qubit to the CCA. We attribute this low dispersive shift and high relative error to be the main cause of misestimation of attenuation for eigenmode 32.

2. AC-Stark shift measurement

The second step consists of measuring the AC-stark shift of the qubit, to estimate the attenuation for mode m , from the left and right side of the CCA. To do so we rewrite the Hamiltonian in Eq. (G1) as,

$$H_{\chi, \text{Qubit}}^{(m)} = \frac{\omega_q}{2} (\sigma_z + 2\chi_m a_m^\dagger a_m) + \tilde{\omega}_m a_m^\dagger a_m. \quad (\text{G2})$$

Hence, according to the equation above, the dressed qubit is expected to shift as a function of the number of photons in mode m , with,

$$\tilde{\omega}_{q, n_m} = \tilde{\omega}_{q, 0} + 2\chi_m n_m, \quad (\text{G3})$$

$\omega_{q, 0}$ is the qubit frequency at low photon number in the mode and χ_m is the dispersive shift of eigenmode m . n_m is the number of photons in mode m , it will depend from which port it is measured from. The number of photons in eigenmode m is:

$$\begin{aligned} n_m &= a_m^\dagger a_m \\ &= \frac{\gamma_{\text{ext}, L}}{\frac{1}{4} (\gamma_{\text{int}} (a_m^\dagger a_m) + \gamma_{\text{ext}, L} + \gamma_{\text{ext}, R})^2} a_{L, m, \text{in}}^\dagger a_{L, m, \text{in}}, \end{aligned} \quad (\text{G4})$$

when measured from the left port, and,

$$\begin{aligned} n_m &= a_m^\dagger a_m \\ &= \frac{\gamma_{\text{ext}, R}}{\frac{1}{4} (\gamma_{\text{int}} (a_m^\dagger a_m) + \gamma_{\text{ext}, L} + \gamma_{\text{ext}, R})^2} a_{R, m, \text{in}}^\dagger a_{R, m, \text{in}}, \end{aligned} \quad (\text{G5})$$

when measured from the right port. And finally,

$$a_{S, m, \text{in}}^\dagger a_{S, m, \text{in}} = \frac{P_{S, m, \text{in}}}{\hbar \tilde{\omega}_m} = \frac{\bar{P}_{S, m, \text{in}} 10^{-A_{S, i}/10}}{\hbar \tilde{\omega}_m}, \quad (\text{G6})$$

with $P_{S, m, \text{in}}$ the input power at the device level for mode m , with S taking the value L (Left) or R (Right), depending on which port we are measuring from. Similarly,

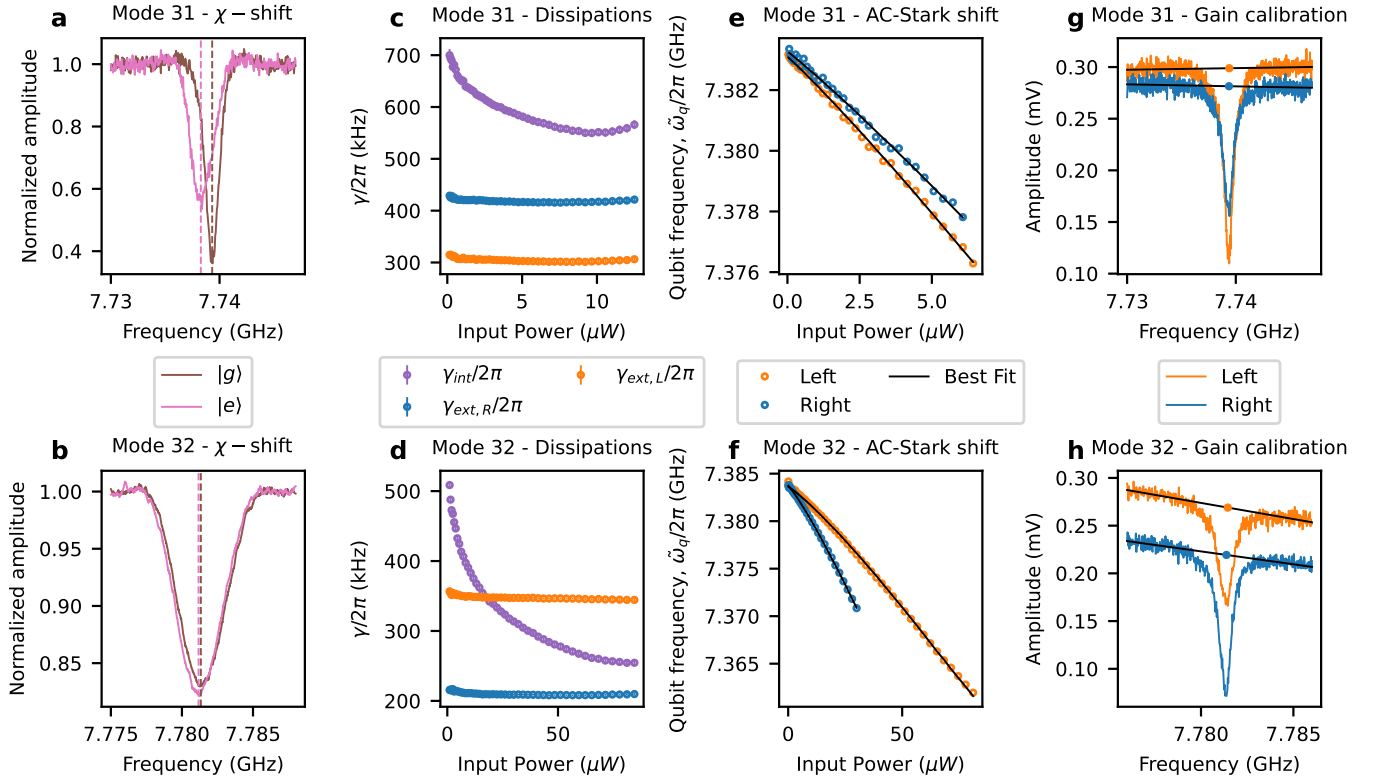


Figure 23. **Attenuation and gain calibration.** (a) [b] Measurement of the dispersive shift χ , of mode 31 (32). The brown color is mode 31 [32] with the qubit in the ground state. The pink color is mode 31 [32] with the qubit in the excited state. The dashed line highlights the resonant frequency of the mode of interest with the qubit in ground (brown) or excited state (pink). (c) [d] Measurement of dissipations for mode 31 [32]. The internal dissipations, $\gamma_{\text{int}}/2\pi$, are reported in purple, the external dissipations to the left, $\gamma_{\text{ext,L}}/2\pi$, are reported in orange, and to the right, $\gamma_{\text{ext,R}}/2\pi$, are reported in blue. (e) [f] Measurement of the AC-Stark shift for mode 31 [32]. The blue circles are the data acquired from the right and the orange circles the data acquired from the left. The continuous black line is the AC-Stark shift fit according to Eq. (G3). (g) [h] Calibration of the gain for mode 31 [32]. Single-tone spectroscopy measurement of the modes to extract the baseline. The data are in orange are acquired from the left and in blue are acquired from the right. The dots are the points chosen to calibrate the gain.

$\bar{P}_{S,m\text{in}}$ is the input power at the output of the digitizer and $A_{S,m}$ is the attenuation of the line from the S port for mode m . $A_{S,m}$ takes into account any amplification and attenuation of the input measurement chain.

Modes 31 and 32, are not overcoupled in the single photon regime, i.e. $\gamma_{\text{int}} \gtrsim \gamma_{\text{ext,L(R)}}$. Hence, before measuring the AC-Stark shift, we need to measure the dissipation rates of the CCA modes as a function of the input power. To be as precise as possible, we use the same input power in the dissipation measurement as the ones for the AC-Stark shift measurements. This measurement is presented in Fig. 23c–d. Mode 31 is more coupled to the right than to the left port [see Fig. 23c]. On the other hand, mode 32 is more coupled to the left than to the right port [see Fig. 23d]. We attribute this asymmetry to two factors: first to disorder which can affect the localization of the eigenmodes, and second to the qubit already affecting the mode shape of the eigenmodes. For both cases we are close to the undercoupled limit and we observe a strong dependence of the internal dissipation rate as a function of the input power.

Finally, we proceed to the AC-Stark shift measurement. For this measurement, the mode of interest is pumped and probed at its resonant frequency, $\tilde{\omega}_m/2\pi$, and the frequency of the qubit is monitored using standard two-tone spectroscopy measurements. The measurements are reported in Fig. 23e–f. In Fig. 23e–f, we report the frequency of the dressed qubit, $\tilde{\omega}_q/2\pi$ extracted from the AC-Stark shift measurement for mode 31 [panel e] and mode 32 [panel f]. We finally fit the qubit frequency shift using Eq. (G3), with the attenuation and initial dressed qubit frequency as the only fitting parameters. The extracted attenuations for the two modes on both sides of the CCA are reported in III. The error on the gain is estimated from the convergence of the fit of the AC-Stark shift as a function of the number points in the fit and the χ -shift error. The nonlinear trend of the AC-stark shifts is due to the varying γ_{int} .

Line	Attenuation (dB)	Gain (dB)
Left - Mode 31	104.59_{+1}^{-1}	86.15_{+1}^{-1}
Right - Mode 31	103.80_{+1}^{-1}	84.83_{+1}^{-1}
Left - Mode 32	$103.95_{-1.67}^{+1.5}$	$84.58_{-1.67}^{+1.5}$
Right - Mode 32	$103.83_{-1.67}^{+1.5}$	$82.69_{-1.67}^{+1.5}$

Table III. Attenuation and gain extracted for the modes at which the emission measurement is done.

3. Extraction of the gain

The last step consists of extracting the gain for each modes from the two sides of the CCA. According to input/output theory, we expect the single-tone spectroscopy response of modes 31 and 32 to follow Eq. (B1) and Eq. (B2), from the left and right side, respectively. Specifically, the absolute value of the scattering coefficient is equal to 1 out of resonance, i.e. $\hat{a}_{\text{out}} = \hat{a}_{\text{in}}$. Thus, we can write, at the baseline,

$$\bar{P}_{S,m \text{ out}}^{\text{dB}} = \bar{P}_{S,m \text{ in}}^{\text{dB}} - A_{S,m} + G_{S,m}, \quad (\text{G7})$$

where $\bar{P}_{S,m \text{ out}}^{\text{dB}} = P_{S,m \text{ out}}^{\text{dB}} + G_{S,m}$ is the output power at the input of the analog to digital converter and $G_{S,m}$ is the gain in dB. We then perform single-tone spectroscopy measurements of modes 31 and 32 in reflection [see Fig. 23g–h], fit the baseline of the norm of the signal [black lines in panels Fig. 23g–h] and extract the amplitude of the expected baseline at the resonant frequency of the modes, at which the attenuation is calibrated and at which the field is emitted. We then find the gain for the two modes from both sides of the CCA by applying Eq. (G7), the values of the gain are reported Tab. III.

Supplementary Information H: Emission measurements

1. Data cleanup

The initial emission data acquired from the CCA are very noisy and do not seem to converge to 0 as a function of time [see Fig. 24a]. We attribute this main source of noise to spurious tones arising from the measurement setup. These can actually be seen in the Fourier transform of the time trace where sharp peaks at $[\pm 125, \pm 250, \pm 375, \pm 500]$ MHz are visible [see Fig. 24b]. These spurious peaks are also present when unplugging the digitizer from the cryostat. To minimize the effect of those spurious tones we place the local oscillator such that the expected emitted field is in the range $[10, 100]$ MHz of the digitizer to limit the influence of those spurious tones. Then we digitally apply sharp notch filters at the frequencies of these spurious tones [red line in Fig. 24b].

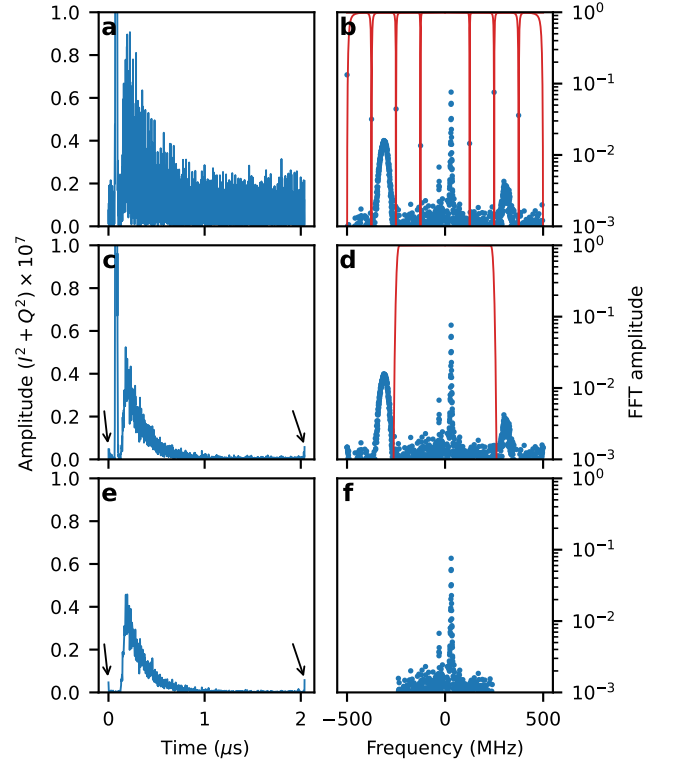


Figure 24. **Emission data cleanup.** (a) Initial time domain trace of the emitted field, where the DC offset has been removed. (b) Fourier transform of the time domain trace presented in panel a [blue dots]. The red lines are the notch filter applied to remove the spurious tones due to the measurement setup at $[\pm 125, \pm 250, \pm 375, \pm 500]$ MHz. (c) Time domain trace after application of the notch filters in panel b. The two black arrows highlight lobes appearing due to the filtering of the data. (d) Fourier transform of the time domain trace presented in panel c [blue dots]. The red line is the FIR filter with a Hamming window applied to the data to remove the π -pulse crosstalk. (e) Time domain trace after application of the FIR filter in panel d. (f) Fourier transform of the time domain trace presented in panel f.

After applying the notch filters, the signal is cleaner [see Fig. 24c] and converge to 0 as a function of time. However, we can notice the appearance of two lobes near $t = 0 \mu\text{s}$ and $t = 2 \mu\text{s}$, these appear due to the application of the numerical filters. We can still observe at 80 ns the presence of a sharp high amplitude tone [also present in Fig. 24a]. It is due to cross-talk between the charge line and the CCA ports. This signal is stronger when measuring the emission from the right than from the left side of the CCA, due to the proximity of the charge line pad to the right pad of the of the CCA input port. We can also notice that this tone does not decay, and is ≈ 40 ns wide corresponding to the length of the π -pulse. We filter out this tone by applying a low pass Finite Impulse Response filter with a cut-off at 250 MHz with Hamming window [red line in Fig. 24d]. The resulting time trace is shown in Fig. 24e and its Fourier transform shown in

Fig. 24f.

The last step consists of converting the signal to field intensity and photon number. The field intensity is converted using,

$$|\langle a_{\text{out}} \rangle|^2 = \frac{I^2 + Q^2}{G} \frac{1}{Z_0 \hbar \omega}, \quad (\text{H1})$$

where G is the gain, a_{out} is the outgoing emitted photon field from the left or right side of the CCA, I and Q are the in-phase and quadrature phase of the signal, $Z_0 = 50 \Omega$ is the waveguide impedance and $\omega/2\pi$ is the frequency of the emitted signal. Finally, we find the emitted photon number at time t using,

$$N_{\text{ph}} = \int_0^t \frac{I^2 + Q^2}{G} \frac{1}{Z_0 \hbar \omega} d\tau. \quad (\text{H2})$$

2. Spectrograms

In Fig. 25a–d, we present spectrograms of the directional emission data from Fig. 5, computed using 200 ns windows with a 1 ns time step. This analysis allows us to trace the temporal evolution of the various frequency tones involved in the emitted data.

The π -pulse is visible in all four spectrograms near 320 MHz, appearing most prominently on the right side due to the proximity of the charge line to the right CCA port. During the SWAP operation, we observe population transfer from the qubit to the mode of interest at the frequencies highlighted by red lines in Fig. 25a–d. Line cuts at these frequencies are shown in Fig. 25e–f.

During the DC ramp, we observe the emitted field frequency shifting to the value indicated by the purple line, corresponding to the expected frequency for directional emission. The cancellation of emission to one side is excellent for mode 31 but poor for mode 32 [see Fig. 25e–f], consistent with the measurements shown in Fig. 5.

We also observe spurious tones arising during the DC ramp, as indicated by the black lines in the spectrograms. These tones only appear during and after the DC ramp and not during the SWAP operation (Fig. 25e–f), suggesting they originate from non-adiabatic transitions to other eigenmodes. While these spurious tones could be avoided using the measurement protocol shown in Ext Data Fig. 6, our current experimental setup did not permit implementation of this protocol.

Supplementary Information I: Fabrication

1. Wafer cleaning

The device is fabricated on a high resistivity ($\geq 10 \text{ k}\Omega \text{ cm}$) 4-inch intrinsic silicon wafer with a thickness of $525 \mu\text{m}$. The wafer is first cleaned in a Piranha solution (sulfuric acid/hydrogen peroxide mixture) to remove organic contaminants, followed by a hydrofluoric acid (HF) bath to remove oxide.

2. Ground plane evaporation

Immediately after cleaning, we deposit a 150 nm aluminum ground plane using electron-beam evaporation (Leybold Optics LAB 600H) at a rate of 0.2 nm s^{-1} .

3. Markers patterning

Alignment markers are patterned using double-layer photolithography (LOR-5A and AZ1512-HS resists) with a laser-writer (Heidelberg Instruments MLA-150). The pattern is developed in AZ 726 MIF developer for 70 s, followed by deposition of 10 nm Ti and 50 nm Pt using electron-beam evaporation. The lift-off process is then performed to complete marker fabrication.

4. Ground plane etching

The wafer is coated with ECI 3007 photoresist, exposed with the laser-writer, and automatically developed. The aluminum ground plane is etched using Alutetch for 2.25 min at 26°C , followed by two water rinses.

5. NbN sputtering and lift-off

The NbN deposition areas are patterned using electron-beam lithography (Raith EBPG5000+) on a bilayer resist stack (MMA EL9/PMMA 495K A8). After development (60 s in 3:1 MiBK:IPA followed by 60 s in IPA), NbN is sputtered using a Kenosistec RF sputtering system following established protocols Ref. [79]. The standard lift-off procedure completes the patterning.

6. Inductor patterning and etching

The metamaterial inductors are patterned on CSAR C04 electron-beam resist using electron-beam lithography. After development (60 s in n-Amyl acetate followed by 60 s in MiBK/IPA), the inductors are dry-etched in an Oxford Plasmalab 80+ using a CF_4/Ar gas mixture with a stepped recipe Ref. [79].

7. Inductor patching

A double layer of electron-beam resist (MMA EL9/PMMA 495K A8) is applied and patterned using electron-beam lithography. After development, the areas to be patched are milled and aluminum is evaporated in a Plassys MEB550SL3 system. The standard lift-off procedure completes the process.

8. Josephson junction patterning and evaporation

The Josephson junctions are designed for Manhattan-style evaporation. After coating with a double layer of MMA EL9/PMMA 495K A8 resist, the junction pattern is exposed using electron-beam lithography. The sample undergoes a 15 s low-power oxygen plasma descum before aluminum evaporation in an angled evaporator (Plassys MEB550SL3). The standard lift-off procedure is then applied.

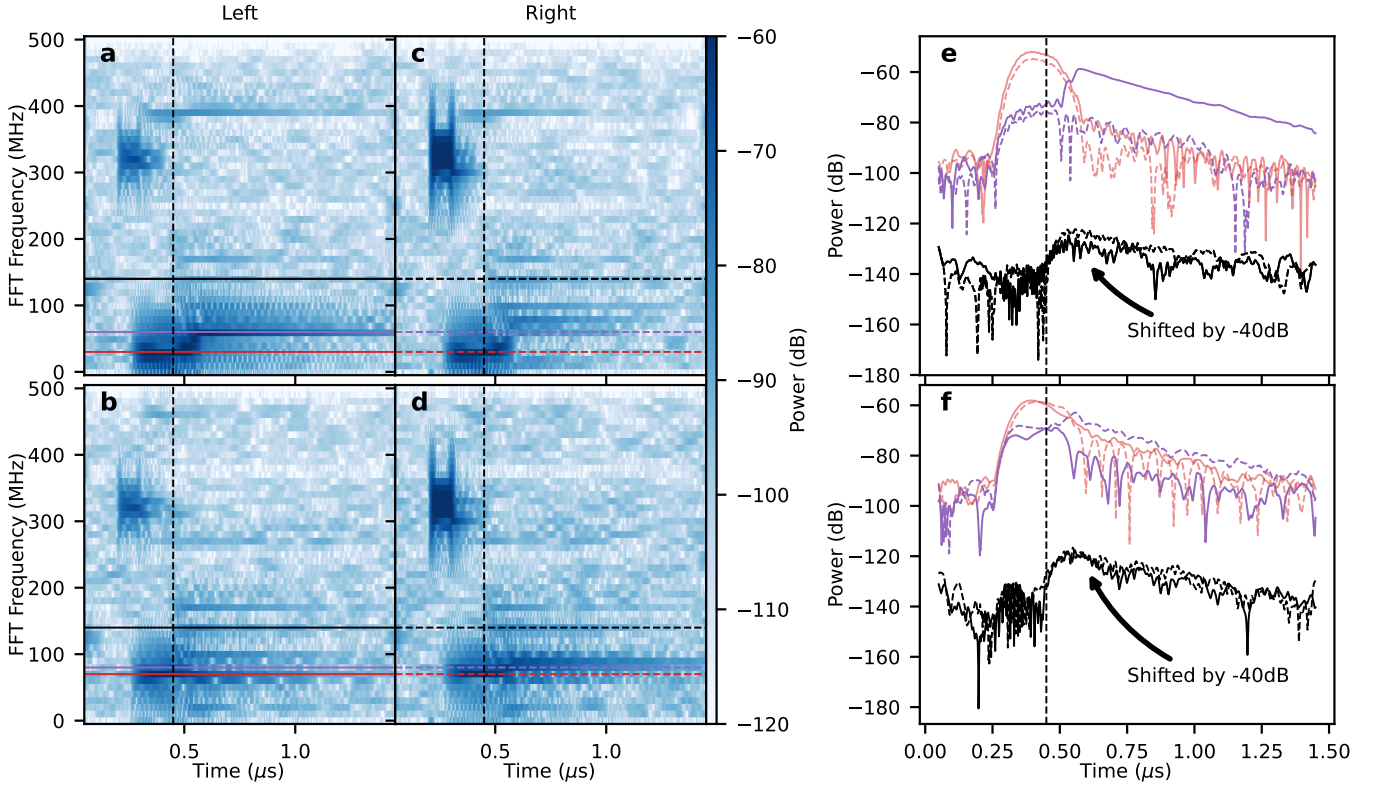


Figure 25. **Spectrograms of the emission measurements.** (a) [b] Spectrogram of the emission measurement acquired from the left for mode 31 [32]. (c) [d] Spectrogram of the emission measurement acquired from the right for mode 31 [32]. The horizontal red and purple lines correspond to the initial frequency of emission and the final frequency of emission after the ramp, respectively. The horizontal black lines highlight spurious tones arising during the ramp. The vertical dashed line highlight the point from which the spurious tones start arising. (e) [f] Line cuts of the spectrogram of the emission measurement acquired from the left (continuous lines) and right (dashed lines) for mode 31 [32]. The black lines are shifted down by -40dB for clarity.

9. Josephson junctions patch

Following the same process as inductor patching, this step repairs any defects in the junction fabrication. The double-layer resist is exposed and developed as before, and aluminum is evaporated and lifted off to complete the junctions.

10. Packaging

Completed devices are diced using a DISCO DAD321 dicer, mounted onto copper holders using MMA EL9, and wire-bonded to PCBs using a semi-automatic bonder (Bondtec).

The standard lift-off procedure consists of sequential solvent baths with sonication: 12 hours in 1165 remover at 70 °C, followed by fresh 1165 remover, methanol, and isopropanol, each with 5 minutes of mild sonication.

Supplementary Information J: Measurement setup

A schematic of the measurement setup is depicted in Fig. 26. The device is thermally anchored to the mixing chamber plate of a commercial dry dilution cryostat

(Bluefors-LD) at a temperature of 10 mK enclosed with an Al and Cu shield, and placed inside a μ -metal shield. The device has 5 input lines: Readout input [A], Drive [B], CCA left [D], CCA right [F] and flux [G]. The input lines are attenuated with cryogenic attenuators at different stages of the cryostat, as reported in 26. The device has 3 output lines: Readout output [H], CCA left [C] and CCA right [E]. All the output lines consist of two double circulator-isolator brackets (LNF-CIIS48A and LNF-ISIS48A), input lines D and F are connected to the circulator of lines C and E, respectively, to be able to measure the device in reflection. A 50 Ω copper termination is placed on the circulator of the readout output. The signal is then amplified with a 4-8 GHz HEMT (LNF-LNC4.8C) thermalized on the 4K stage of the cryostat, it is then re-amplified at room temperature with a 4-8 GHz low noise amplifier (Agile AMT-A0284). All lines are filtered at the mixing chamber stage first with an Eccosorb filter (QMC-CRYOIRF-003MF-S [filter (d) in Fig. 26] and QMC-CRYOIRF-001MF-S [filter (e) in Fig. 26]) and with cryogenic low pass filters (RLC-F-30-8000 [filter (a) in Fig. 26], RLC-F-30-12.4 [filter (b) in Fig. 26], RLC-F-10-3000 [filter (c) in Fig. 26]). The coil bias is controlled with a current source Yokogawa

GS200.

The spectroscopy measurements used in Fig. 2, Fig. 3 and Fig. 13 are performed using a 4 ports R&S ZNB20 vector network analyzer (VNA) [Fig. 27a] with 20 dB input attenuators. The rest of the measurements are performed using an OPX+ coupled to an Octave from Quantum Machine, implementing standard heterodyne

measurement techniques. The readout input line [A] is attenuated with a 30 dB attenuator and filtered with a low-pass filter (ZLSS-4R8G-S+ [filter (a) in Fig. 27b]). The CCA input line is attenuated with a 20 dB attenuator and filtered with a low-pass filter (VLF-8400+ [filter (b) in Fig. 27b]). The Drive line is attenuated with a 20 dB attenuator and filtered with a low-pass filter (FLP0960 [filter (c) in Fig. 27b]).

-
- [1] A. Wallraff, D. I. Schuster, A. Blais, L. Frunzio, R.-S. Huang, J. Majer, S. Kumar, S. M. Girvin, and R. J. Schoelkopf, Strong coupling of a single photon to a superconducting qubit using circuit quantum electrodynamics, *Nature* **431**, 162 (2004).
 - [2] S. Haroche and J.-M. Raimond, *Exploring the quantum: atoms, cavities, and photons* (Oxford university press, 2006).
 - [3] S. Krinner, N. Lacroix, A. Remm, A. Di Paolo, E. Genois, C. Leroux, C. Hellings, S. Lazar, F. Swiadek, J. Herrmann, *et al.*, Realizing repeated quantum error correction in a distance-three surface code, *Nature* **605**, 669 (2022).
 - [4] D. E. Chang, A. S. Sørensen, E. A. Demler, and M. D. Lukin, A single-photon transistor using nanoscale surface plasmons, *Nature physics* **3**, 807 (2007).
 - [5] I. Söllner, S. Mahmoodian, S. L. Hansen, L. Midolo, A. Javadi, G. Kiršanskė, T. Pognolato, H. El-Ella, E. H. Lee, J. D. Song, *et al.*, Deterministic photon-emitter coupling in chiral photonic circuits, *Nature nanotechnology* **10**, 775 (2015).
 - [6] D. Chang, J. Douglas, A. González-Tudela, C.-L. Hung, and H. Kimble, Colloquium: Quantum matter built from nanoscopic lattices of atoms and photons, *Reviews of Modern Physics* **90**, 031002 (2018).
 - [7] A. S. Sheremet, M. I. Petrov, I. V. Iorsh, A. V. Poshakinskiy, and A. N. Poddubny, Waveguide quantum electrodynamics: Collective radiance and photon-photon correlations, *Reviews of Modern Physics* **95**, 015002 (2023).
 - [8] B. Kannan, A. Almanakly, Y. Sung, A. Di Paolo, D. A. Rower, J. Braumüller, A. Melville, B. M. Niedzielski, A. Karamlou, K. Serniak, A. Vepsäläinen, M. E. Schwartz, J. L. Yoder, R. Winik, J. I.-J. Wang, T. P. Orlando, S. Gustavsson, J. A. Grover, and W. D. Oliver, On-demand directional microwave photon emission using waveguide quantum electrodynamics, *Nature Physics* **19**, 394 (2023).
 - [9] F. Ciccarello, P. Lodahl, and D. Schneble, Waveguide quantum electrodynamics, *Optics and Photonics News* **35**, 34 (2024).
 - [10] P. Lodahl, S. Mahmoodian, S. Stobbe, A. Rauschenbeutel, P. Schneeweiss, J. Volz, H. Pichler, and P. Zoller, Chiral quantum optics, *Nature* **541**, 473 (2017).
 - [11] N. M. Sundaresan, Y. Liu, D. Sadri, L. J. Szöcs, D. L. Underwood, M. Malekakhlagh, H. E. Türeci, and A. A. Houck, Beyond Strong Coupling in a Multimode Cavity, *Physical Review X* **5**, 021035 (2015).
 - [12] D. Meiser and P. Meystre, Superstrong coupling regime of cavity quantum electrodynamics, *Physical Review A* **74**, 065801 (2006).
 - [13] D. O. Krimer, M. Liertzer, S. Rotter, and H. E. Türeci, Route from spontaneous decay to complex multimode dynamics in cavity qed, *Physical Review A* **89**, 033820 (2014).
 - [14] K. Sinha, S. A. Khan, E. Cüce, and H. E. Türeci, Radiative properties of an artificial atom coupled to a josephson-junction array, *Physical Review A* **106**, 033714 (2022).
 - [15] A. Johnson, M. Blaha, A. E. Ulanov, A. Rauschenbeutel, P. Schneeweiss, and J. Volz, Observation of collective superstrong coupling of cold atoms to a 30-m long optical resonator, *Physical review letters* **123**, 243602 (2019).
 - [16] R. Kuzmin, N. Mehta, N. Grabon, R. Mencia, and V. E. Manucharyan, Superstrong coupling in circuit quantum electrodynamics, *npj Quantum Information* **5**, 1 (2019).
 - [17] S. Léger, J. Puertas-Martínez, K. Bharadwaj, R. Dasonneville, J. Delaforce, F. Foroughi, V. Milchakov, L. Planat, O. Buisson, C. Naud, *et al.*, Observation of quantum many-body effects due to zero point fluctuations in superconducting circuits, *Nature Communications* **10**, 5259 (2019).
 - [18] N. Mehta, R. Kuzmin, C. Ciuti, and V. E. Manucharyan, Down-conversion of a single photon as a probe of many-body localization, *Nature* **613**, 650 (2023).
 - [19] D. Fraudet, I. Snyman, D. M. Basko, S. Léger, T. Sépulcre, A. Ranadive, G. Le Gal, A. Torras-Coloma, W. Guichard, S. Florens, *et al.*, Direct detection of down-converted photons spontaneously produced at a single josephson junction, *Physical Review Letters* **134**, 013804 (2025).
 - [20] D. Lechner, R. Pennetta, M. Blaha, P. Schneeweiss, A. Rauschenbeutel, and J. Volz, Light-matter interaction at the transition between cavity and waveguide qed, *Physical Review Letters* **131**, 103603 (2023).
 - [21] C. Castillo-Moreno, K. R. Amin, I. Strandberg, M. Kervinen, A. Osman, and S. Gasparinetti, Dynamical excitation control and multimode emission of an atom-photon bound state, *Physical Review Letters* **134**, 133601 (2025).
 - [22] Y. Liu and A. A. Houck, Quantum electrodynamics near a photonic bandgap, *Nature Phys* **13**, 48 (2017).
 - [23] N. M. Sundaresan, R. Lundgren, G. Zhu, A. V. Gorshkov, and A. A. Houck, Interacting Qubit-Photon Bound States with Superconducting Circuits, *Phys. Rev. X* **9**, 011021 (2019).
 - [24] M. Mirhosseini, E. Kim, V. S. Ferreira, M. Kalaei, A. Sipahigil, A. J. Keller, and O. Painter, Superconducting metamaterials for waveguide quantum electrodynamics, *Nature communications* **9**, 3706 (2018).
 - [25] S. Indrajeet, H. Wang, M. Hutchings, B. Taketani, F. K. Wilhelm, M. LaHaye, and B. Plourde, Coupling a superconducting qubit to a left-handed metamaterial res-

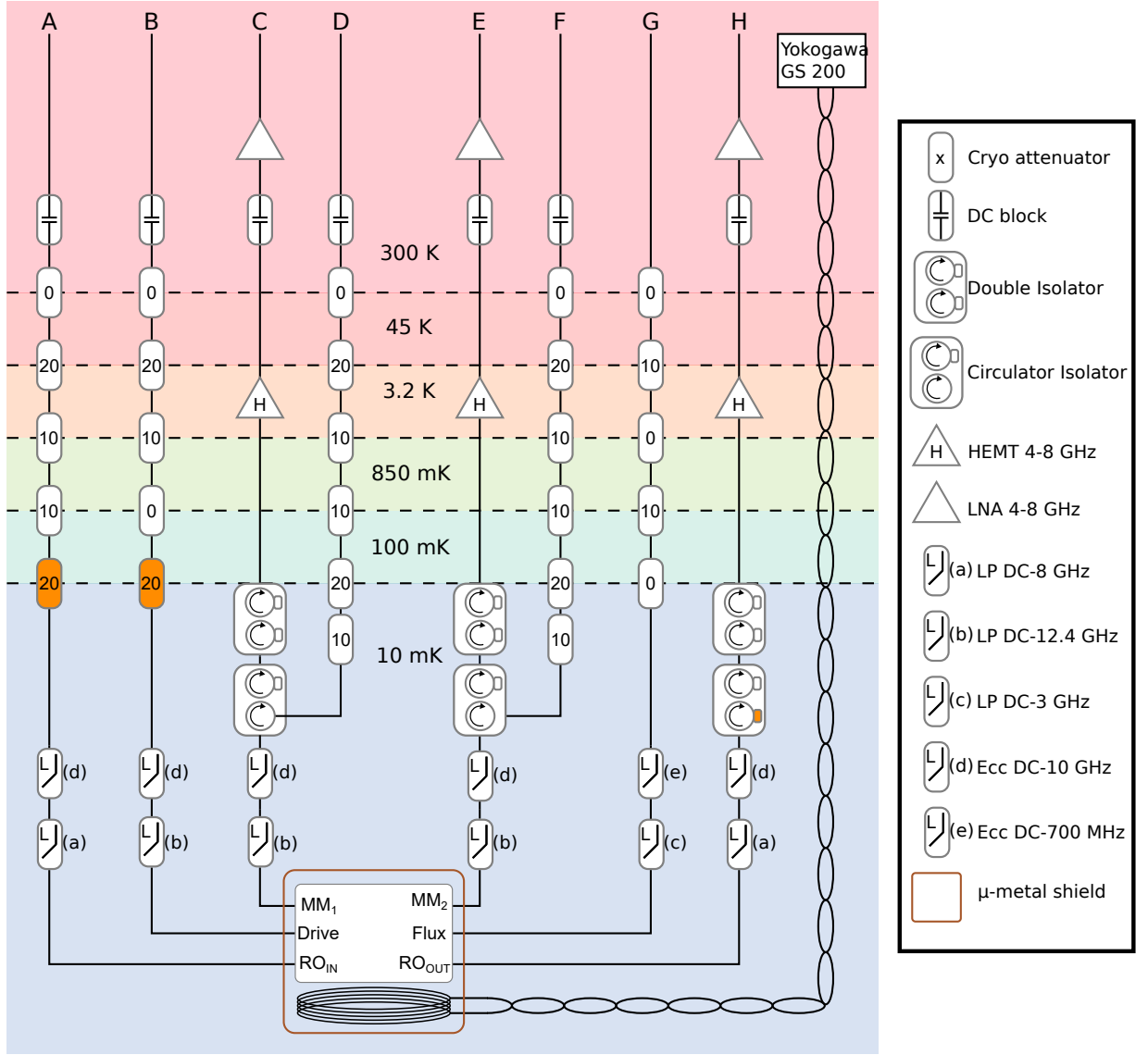


Figure 26. **Schematic of the cryogenic setup.**

- onator, *Physical Review Applied* **14**, 064033 (2020).
- [26] E. Kim, X. Zhang, V. S. Ferreira, J. Banker, J. K. Iverson, A. Sipahigil, M. Bello, A. González-Tudela, M. Mirhosseini, and O. Painter, Quantum Electrodynamics in a Topological Waveguide, *Phys. Rev. X* **11**, 011015 (2021).
- [27] M. Scigliuzzo, G. Calajò, F. Ciccarello, D. Perez Lozano, A. Bengtsson, P. Scarlino, A. Wallraff, D. Chang, P. Delsing, and S. Gasparinetti, Controlling Atom-Photon Bound States in an Array of Josephson-Junction Resonators, *Physical Review X* **12**, 031036 (2022).
- [28] V. Jouanny, S. Frasca, V. J. Weibel, L. Peyruchat, M. Scigliuzzo, F. Oppliger, F. De Palma, D. Sbroglio, G. Beaulieu, O. Zilberberg, *et al.*, High kinetic inductance cavity arrays for compact band engineering and topology-based disorder meters, *Nature Communications* **16**, 3396 (2025).
- [29] V. S. Ferreira, J. Banker, A. Sipahigil, M. H. Matheny, A. J. Keller, E. Kim, M. Mirhosseini, and O. Painter, Collapse and revival of an artificial atom coupled to a structured photonic reservoir, *Phys. Rev. X* **11**, 041043 (2021).
- [30] A. J. Kollár, M. Fitzpatrick, and A. A. Houck, Hyperbolic lattices in circuit quantum electrodynamics, *Nature* **571**, 45 (2019).
- [31] R. Naik, N. Leung, S. Chakram, P. Groszkowski, Y. Lu, N. Earnest, D. McKay, J. Koch, and D. I. Schuster, Random access quantum information processors using multi-mode circuit quantum electrodynamics, *Nature communications* **8**, 1 (2017).
- [32] J. C. Owens, M. G. Panetta, B. Saxberg, G. Roberts, S. Chakram, R. Ma, A. Vrajitoarea, J. Simon, and D. I. Schuster, Chiral cavity quantum electrodynamics, *Nat. Phys.* **18**, 1048 (2022).
- [33] T. Shi, Y.-H. Wu, A. González-Tudela, and J. I. Cirac, Bound states in boson impurity models, *Physical Review*

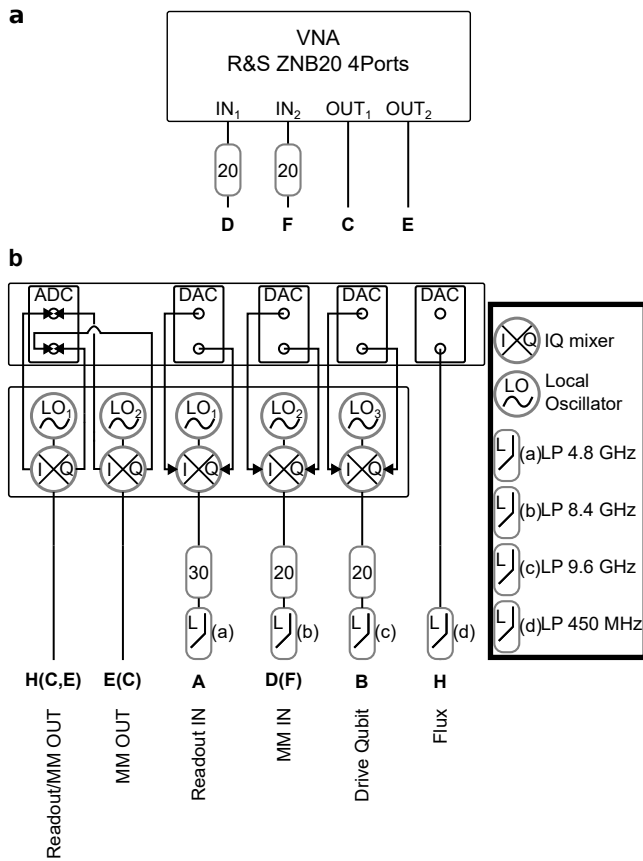


Figure 27. **Room temperature setup.** (a) Schematic of the VNA setup. (b) Schematic of the time-domain setup.

- X **6**, 021027 (2016).
- [34] G. Calajó, F. Ciccarello, D. Chang, and P. Rabl, Atom-field dressed states in slow-light waveguide QED, *Phys. Rev. A* **93**, 033833 (2016).
 - [35] X. Zhang, E. Kim, D. K. Mark, S. Choi, and O. Painter, A superconducting quantum simulator based on a photonic-bandgap metamaterial, *Science* **379**, 278 (2023).
 - [36] G. Kim, A. Butler, V. S. Ferreira, X. Zhang, A. Hadley, E. Kim, and O. Painter, Fast unconditional reset and leakage reduction of a tunable superconducting qubit via an engineered dissipative bath, *Physical Review Applied* **24**, 014013 (2025).
 - [37] A. V. Gorshkov, D. Cohen, A. Haim, A. Rotem, O. Golan, G. Kim, A. Butler, C. T. Hann, O. Painter, F. G. Brandão, *et al.*, Cavity-mediated cross-cross-resonance gate, *arXiv preprint arXiv:2506.03239* (2025).
 - [38] T. Thorbeck, A. McDonald, O. Lanes, J. Blair, G. Keefe, A. A. Stabile, B. Royer, L. C. Govia, and A. Blais, High-fidelity gates in a transmon using bath engineering for passive leakage reset, *arXiv preprint arXiv:2411.04101* (2024).
 - [39] M. Bello, G. Platero, J. I. Cirac, and A. González-Tudela, Unconventional quantum optics in topological waveguide QED, *Sci. Adv.* **5**, eaaw0297 (2019).
 - [40] P. Pakkiam, N. P. Kumar, C.-C. Chiu, D. Sommers, M. Pletyukhov, and A. Fedorov, Experimental realization of qubit-state-controlled directional edge states in waveguide qed, *arXiv preprint arXiv:2411.05271* (2024).
 - [41] X. Wang, H.-B. Zhu, T. Liu, and F. Nori, Realizing quantum optics in structured environments with giant atoms, *Physical Review Research* **6**, 013279 (2024).
 - [42] M. V. Gustafsson, T. Aref, A. F. Kockum, M. K. Ekström, G. Johansson, and P. Delsing, Propagating phonons coupled to an artificial atom, *Science* **346**, 207 (2014).
 - [43] A. Frisk Kockum, Quantum Optics with Giant Atoms—the First Five Years, in *International Symposium on Mathematics, Quantum Theory, and Cryptography*, Mathematics for Industry, edited by T. Takagi, M. Wakayama, K. Tanaka, N. Kunihito, K. Kimoto, and Y. Ikematsu (Springer, Singapore, 2021) pp. 125–146.
 - [44] A. Frisk Kockum, P. Delsing, and G. Johansson, Designing frequency-dependent relaxation rates and Lamb shifts for a giant artificial atom, *Physical Review A* **90**, 013837 (2014).
 - [45] B. Kannan, M. J. Ruckriegel, D. L. Campbell, A. Frisk Kockum, J. Braumüller, D. K. Kim, M. Kjaergaard, P. Krantz, A. Melville, B. M. Niedzielski, A. Vepsäläinen, R. Winik, J. L. Yoder, F. Nori, T. P. Orlando, S. Gustavsson, and W. D. Oliver, Waveguide quantum electrodynamics with superconducting artificial giant atoms, *Nature* **583**, 775 (2020).
 - [46] A. M. Vadiraj, A. Ask, T. G. McConkey, I. Nsanzineza, C. W. S. Chang, A. F. Kockum, and C. M. Wilson, Engineering the level structure of a giant artificial atom in waveguide quantum electrodynamics, *Physical Review A* **103**, 023710 (2021).
 - [47] C. Joshi, F. Yang, and M. Mirhosseini, Resonance Fluorescence of a Chiral Artificial Atom, *Physical Review X* **13**, 021039 (2023).
 - [48] A. Soro, C. S. Muñoz, and A. F. Kockum, Interaction between giant atoms in a one-dimensional structured environment, *Phys. Rev. A* **107**, 013710 (2023).
 - [49] L. Leonforte, X. Sun, D. Valenti, B. Spagnolo, F. Illuminati, A. Carollo, and F. Ciccarello, *Quantum optics with giant atoms in a structured photonic bath* (2024).
 - [50] Z.-M. Gao, J.-Q. Li, Z.-W. Li, W.-X. Liu, and X. Wang, Circuit QED with giant atoms coupling to left-handed superlattice metamaterials, *Physical Review A* **109**, 013716 (2024).
 - [51] X. Wang, T. Liu, A. F. Kockum, H.-R. Li, and F. Nori, Tunable chiral bound states with giant atoms, *Physical Review Letters* **126**, 043602 (2021).
 - [52] X. Zhang, C. Liu, Z. Gong, and Z. Wang, Quantum interference and controllable magic cavity qed via a giant atom in a coupled resonator waveguide, *Physical Review A* **108**, 013704 (2023).
 - [53] W.-P. Su, J. Schrieffer, and A. Heeger, Soliton excitations in polyacetylene, *Physical Review B* **22**, 2099 (1980).
 - [54] J. K. Asbóth, L. Oroszlány, and A. Pályi, *A Short Course on Topological Insulators*, Lecture Notes in Physics, Vol. 919 (Springer International Publishing, Cham, 2016).
 - [55] J. Koch, T. M. Yu, J. Gambetta, A. A. Houck, D. I. Schuster, J. Majer, A. Blais, M. H. Devoret, S. M. Girvin, and R. J. Schoelkopf, Charge-insensitive qubit design derived from the Cooper pair box, *Physical Review A* **76**, 042319 (2007).
 - [56] M. Scigliuzzo, L. Peyruchat, R. M. Marabini, C. Becker, V. Jouanny, P. Delsing, and P. Scarlino, Quantum acous-

- tics with tunable nonlinearity in the superstrong coupling regime, [arXiv preprint arXiv:2505.24865](#) (2025).
- [57] Z. K. Mineev, Z. Leghtas, S. O. Mundhada, L. Christakis, I. M. Pop, and M. H. Devoret, Energy-participation quantization of josephson circuits, [npj Quantum Information](#) **7**, 131 (2021).
 - [58] R. P. Feynman, Forces in Molecules, [Physical Review](#) **56**, 340 (1939).
 - [59] C. Müller, J. H. Cole, and J. Lisenfeld, Towards understanding two-level-systems in amorphous solids: insights from quantum circuits, [Reports on Progress in Physics](#) **82**, 124501 (2019).
 - [60] D. Suárez-Forero, M. Jalali Mehrabad, C. Vega, A. González-Tudela, and M. Hafezi, Chiral quantum optics: recent developments and future directions, [Prx Quantum](#) **6**, 020101 (2025).
 - [61] J. Petersen, J. Volz, and A. Rauschenbeutel, Chiral nanophotonic waveguide interface based on spin-orbit interaction of light, [Science](#) **346**, 67 (2014).
 - [62] A. Almanakly, B. Yankelevich, M. Hays, B. Kannan, R. Assouly, A. Greene, M. Gingras, B. M. Niedzielski, H. Stickler, M. E. Schwartz, *et al.*, Deterministic remote entanglement using a chiral quantum interconnect, [Nature Physics](#), 1 (2025).
 - [63] A. González-Tudela and J. I. Cirac, Exotic quantum dynamics and purely long-range coherent interactions in Dirac conelike baths, [Phys. Rev. A](#) **97**, 043831 (2018).
 - [64] E. Raaholt Ingelsten, A. F. Kockum, and A. Soro, Avoiding decoherence with giant atoms in a two-dimensional structured environment, [Physical Review Research](#) **6**, 043222 (2024).
 - [65] E. Di Benedetto, X. Sun, M. A. Pinto, L. Leonforte, C.-Y. Chang, V. Jouanny, L. Peyruchat, P. Scarlino, and F. Ciccarello, Emergent cavity-qed dynamics along the edge of a photonic lattice, [arXiv preprint arXiv:2507.13444](#) (2025).
 - [66] P. Longo, P. Schmitteckert, and K. Busch, Few-photon transport in low-dimensional systems: interaction-induced radiation trapping, [Physical review letters](#) **104**, 023602 (2010).
 - [67] V. E. Manucharyan, J. Koch, L. I. Glazman, and M. H. Devoret, Fluxonium: Single cooper-pair circuit free of charge offsets, [Science](#) **326**, 113 (2009).
 - [68] P. Scarlino, J. H. Ungerer, D. J. van Woerkom, M. Mancini, P. Stano, C. Müller, A. J. Landig, J. V. Koski, C. Reichl, W. Wegscheider, *et al.*, In situ tuning of the electric-dipole strength of a double-dot charge qubit: Charge-noise protection and ultrastrong coupling, [Physical Review X](#) **12**, 031004 (2022).
 - [69] Y. Ashida, T. Yokota, A. İmamoğlu, and E. Demler, Non-perturbative waveguide quantum electrodynamics, [Physical Review Research](#) **4**, 023194 (2022).
 - [70] C. Sánchez Muñoz, F. Nori, and S. De Liberato, Resolution of superluminal signalling in non-perturbative cavity quantum electrodynamics, [Nature communications](#) **9**, 1924 (2018).
 - [71] J. R. Schrieffer and P. A. Wolff, Relation between the Anderson and Kondo Hamiltonians, [Physical Review](#) **149**, 491 (1966).
 - [72] S. Bravyi, D. P. DiVincenzo, and D. Loss, Schrieffer–Wolff transformation for quantum many-body systems, [Annals of Physics](#) **326**, 2793 (2011).
 - [73] S. Longhi, Bound states in the continuum in a single-level fano-anderson model, [The European Physical Journal B](#) **57**, 45 (2007).
 - [74] E. N. Economou, Green’s Functions for Tight Binding Hamiltonians, in [Green’s Functions in Quantum Physics](#), Springer Series in Solid-State Sciences, edited by E. N. Economou (Springer, Berlin, Heidelberg, 1979) pp. 71–91.
 - [75] L. Leonforte, D. Valenti, B. Spagnolo, A. Carollo, and F. Ciccarello, Dressed emitters as impurities, [Nanophotonics](#) **10**, 4251 (2021).
 - [76] A. Mercurio, Y.-T. Huang, L.-X. Cai, Y.-N. Chen, V. Savona, and F. Nori, [Quantumtoolbox.jl: An efficient julia framework for simulating open quantum systems](#) (2025), [arXiv:2504.21440 \[quant-ph\]](#).
 - [77] A. Blais, A. L. Grimsmo, S. Girvin, and A. Wallraff, Circuit quantum electrodynamics, [Rev. Mod. Phys.](#) **93**, 025005 (2021).
 - [78] F. Motzoi, J. M. Gambetta, P. Rebentrost, and F. K. Wilhelm, Simple Pulses for Elimination of Leakage in Weakly Nonlinear Qubits, [Physical Review Letters](#) **103**, 110501 (2009).
 - [79] S. Frasca, I. N. Arabadzhev, S. B. de Puechredon, F. Oppliger, V. Jouanny, R. Musio, M. Scigliuzzo, F. Minganti, P. Scarlino, and E. Charbon, Nbn films with high kinetic inductance for high-quality compact superconducting resonators, [Physical Review Applied](#) **20**, 044021 (2023).